

CELSO JACO FACCIO JÚNIOR

**A  $C^1$  spline-based contact formulation:**  
textile applications

São Paulo  
2023

CELSONO JACO FACCIÓ JUNIOR

**A  $C^1$  spline-based contact formulation:**  
textile applications

**Revised Version**

Thesis submitted to the Polytechnic School  
at the University of São Paulo in partial  
fulfillment of the requirements for the  
degree of Doctor of Science.

Concentration area:

Structures

Advisor:

Prof. Dr. Alfredo Gay Neto

São Paulo  
2023

Autorizo a reprodução e divulgação total ou parcial deste trabalho, por qualquer meio convencional ou eletrônico, para fins de estudo e pesquisa, desde que citada a fonte.

Este exemplar foi revisado e corrigido em relação à versão original, sob responsabilidade única do autor e com a anuência de seu orientador.

São Paulo, \_\_\_\_\_ de \_\_\_\_\_ de \_\_\_\_\_

Assinatura do autor: \_\_\_\_\_

Assinatura do orientador: \_\_\_\_\_

#### Catálogo-na-publicação

Faccio Júnior, Celso Jaco

Uma Formulação de Contato  $C^1$  Baseada em Splines: Aplicações Têxteis /

C. J. Faccio Júnior -- versão corr. -- São Paulo, 2023.

123 p.

Tese (Doutorado) - Escola Politécnica da Universidade de São Paulo.  
Departamento de Engenharia de Estruturas e Geotécnica.

1.Spline 2.Contato normal não linear 3.Atrito 4.Contato pontual 5.Contato conforme I.Universidade de São Paulo. Escola Politécnica. Departamento de Engenharia de Estruturas e Geotécnica II.t.

FACCIO JÚNIOR, C. J. A  $C^1$  **spline-based contact formulation**: textile applications. 2023. Thesis (Doctorate in Civil Engineering) – Polytechnic School, University of São Paulo, São Paulo, 2023.

Date approved

Examination Board

Prof. Dr. Alfredo Gay Neto  
Institute University of São Paulo (EP-USP)  
Decision \_\_\_\_\_

Prof. Dr. Paulo de Mattos Pimenta  
Institute University of São Paulo (EP-USP)  
Decision \_\_\_\_\_

Prof. Dr. Eduardo Nobre Lages  
Institute Federal University of Alagoas (UFAL)  
Decision \_\_\_\_\_

Prof. Dr. Marco Lucio Bittencourt  
Institute University of Campinas (Unicamp)  
Decision \_\_\_\_\_

Prof. Dr. Alex Alves Bandeira  
Institute Federal University of Bahia (UFBA)  
Decision \_\_\_\_\_

To Soraya and Celso

# ACKNOWLEDGEMENTS

I would like to thank my advisor, Prof. Alfredo Gay Neto, for guiding me through this journey. His work as an advisor was fundamental in providing insights and believing this thesis.

I would like to thank my beloved wife, Isadora Castro, for supporting me all the time and listening to countless meetings.

I would like to thank my parents, Soraya Lima and Celso Faccio, for raising me with love and good education.

I would like to thank my sister, Patrícia Faccio, for the incentive to face this process.

I would like to thank Dom and Gigi for their unconditional love.

I would like to thank the financial support provided by the National Council for Scientific and Technological Development (CNPq) under the grants 168927/2018-7 (candidate) and 304321/2021-4 (advisor), and the São Paulo Research Foundation (FAPESP) under the grant 2020/13362-1.

All things considered, I believe that this thesis results from three main factors, not in any particular order: privileges, hard work, and luck. The privileges I benefited from, including those I'm aware of and those I'm not. The hard work of many in researching and developing. Finally, a bit of luck, which is somehow everywhere, but is hard to tell.

Last but not least, as any reasonable researcher, I reserve myself the right of being terribly wrong.

*“Geometry is not true, it is advantageous.”*

– Henri Poincaré

# RESUMO

FACCIO JÚNIOR, C. J. **Uma formulação de contato  $C^1$  baseada em splines: aplicações têxteis.** 2023. Tese (Doutorado em Engenharia Civil) – Escola Politécnica, Universidade de São Paulo, São Paulo, 2023.

O contato entre corpos é um fenômeno complexo que envolve interação mecânica, atrito, transferência de calor, entre outros fatores. Uma abordagem comum (e conveniente) para interação mecânica em um ambiente de elementos finitos é usar diretamente a geometria dos elementos para formular a interação por contato. A principal desvantagem dessa abordagem está na existência de arestas agudas formadas, por exemplo, pela junção de elementos finitos retilíneos ou não-suaves que podem levar a singularidades de contato. Para contornar este problema, particularmente no contexto de contatos viga-a-viga, o presente trabalho propõe uma formulação de elementos de contato baseada em curvas splines  $C^1$ . A formulação baseada em splines é desenvolvida para lidar com cenários de contato conforme (distribuído) e não-conforme (pontual). Uma estratégia de três critérios é introduzida para auxiliar no processo de tomada de decisão entre cenários de contato conforme e não-conforme. A formulação baseada em splines proposta pode ser anexada diretamente a qualquer formulação envolvendo elementos finitos de viga quadráticos, garantindo uma descrição suave para esses elementos. Uma lei específica de interação de contato normal não-linear e um modelo reológico para atrito já estabelecido, ambos com contribuições elásticas e viscosas, são adotados aumentando as possibilidades em aplicações práticas. Para demonstrar algumas possibilidades de aplicação, vários exemplos são explorados, incluindo comparações diretas com uma formulação de contato superfície-a-superfície e uma formulação alternativa de contato suave, além de exemplos desafiadores envolvendo contatos conformes e não-conformes e aplicações têxteis.

Palavras-chave: Spline. Contato normal não-linear. Atrito. Contato pontual. Contato conforme.



# ABSTRACT

FACCIO JÚNIOR, C. J. **A  $C^1$  spline-based contact formulation:** textile applications. 2023. Thesis (Doctorate in Civil Engineering) – Polytechnic School, University of São Paulo, São Paulo, 2023.

The contact between bodies is a complex phenomenon that involves mechanical interaction, frictional sliding, and heat transfer, among others. A common (and convenient) approach for mechanical interaction in a finite element framework is to directly use the geometry of the elements to formulate the contact. The main drawback lies in the sharp corners that occur when straight or non-smooth finite elements are connected leading eventually to contact singularities. To circumvent this issue, particularly in the context of beam-to-beam contact, the present work proposes contact formulation based on smooth  $C^1$  continuous spline contact elements. The spline-based formulation is designed to handle conformal (distributed) and non-conformal (pointwise) contact scenarios. A three-criterion strategy is introduced to aid in the decision-making process between conformal and non-conformal contact. The proposed spline-based formulation, which can be directly attached to any quadratic beam finite element formulation, guarantees a smooth description for the whole set of elements, where contact takes place. A specific nonlinear normal contact interaction law and an established rheological model for friction, both with elastic and viscous damping contributions, are adopted increasing robustness in practical applications. To demonstrate this robustness several examples are explored including direct comparisons with a similar surface-to-surface formulation and an alternative smooth contact scheme and challenging examples involving conformal and non-conformal contacts and textile applications.

Keywords: Spline. Nonlinear normal contact. Friction. Pointwise contact. Conformal contact.

# LIST OF FIGURES

1	Comparison between experimental and computational results of the biaxial mechanical behavior of a textile. Extracted from [1]. . . . .	22
2	Non-conformal contact with the spline-based contact formulations. Ex- tracted from [2]. . . . .	22
3	Conformal contact with the spline-based contact formulations. . . . .	23
4	Contact interaction between two bodies. . . . .	26
5	Basis functions calculated based on a knot vector $\Xi = \{0, 0, 0, 1/3, 2/3, 1, 1, 1\}$ for two quadratic beam elements. Dashed lines represent the knot spans (spline elements) [2]. . . . .	31
6	Spline and spline-based surface [2]. . . . .	32
7	Basis functions calculated for the spline elements based on the original knot vector $\Xi = \{0, 0, 0, 1/3, 2/3, 1, 1, 1\}$ . . . . .	33
8	Representation of three spline elements and three spline-based surface re- gions based on the original spline presented in Figure 5 [2]. . . . .	34
9	Representations of the rough contact search and the local contact search [2].	36
10	Spline element in black with a gray dashed line control mesh and orange control points. Red arrows indicating generalized displacements $\mathbf{u}_{AA}$ , $\mathbf{u}_{AB}$ , and $\mathbf{u}_{AC}$ , which rule the position of control points [2]. . . . .	37
11	Normal contact compliance law from [55] proposed for $\mathbf{f}_{ne}$ as red marks and approximated by a power trendline as a black solid line. Compliance law adopted in the numerical example of textile shear [2]. . . . .	40
12	Representation of the frictional contact of two splines $\Gamma_A^{i+1}$ and $\Gamma_B^{i+1}$ at configuration “ $i + 1$ ”. The red arrows indicate the sliding paths $\gamma_A^\Delta$ and $\gamma_B^\Delta$ , and the normal direction $\mathbf{n}^{i+1}$ [2]. . . . .	41
13	Rheological model for the frictional interaction including two sliding devices (1 and 2), an elastic contribution, and a dissipative contribution [2]. . . . .	43
14	LCP degenerations [3]. . . . .	46

15	Cases with ill-defined LCP solution [3]. . . . .	47
16	Spline elements $\Gamma_A$ and $\Gamma_B$ respectively in blue and green with their control meshes in gray for $h_A = 1$ and $h_B = 1$ [3]. . . . .	49
17	Hessian matrix eigenvalues evolution for a fixed $h_B = 1$ and several $h_A$ values for a curved conformal contact scenario [3]. . . . .	49
18	Hessian matrix eigenvalues evolution for a fixed $h_B = 0$ and several $h_A$ values for a straight conformal contact scenario. . . . .	51
19	LCP solution workflow [3]. . . . .	54
20	Representation of the displacement field of a generic point $\mathbf{x}$ according to the geometrically-exact beam theory adopted [1]. . . . .	56
21	Original developed software for integrating the Giraffe solver with the TexGen <sup>®</sup> software. . . . .	64
22	Textile geometric parameters [1]. . . . .	65
23	Yarns relative crimp [1]. . . . .	65
24	Textile modeling strategy [1]. . . . .	65
25	Representation of perpendicular beams model example with prescribed displacements [2]. . . . .	67
26	Reactions obtained at point B in the perpendicular beams contact example with normal contact [2]. . . . .	67
27	Perpendicular beams contact with red arrows and blue arrows representing respectively the “SP” model and the “SS” model. Simulation includes normal contact only [2]. . . . .	68
28	Detailed view of the normal contact forces representation [2]. . . . .	68
29	Reactions obtained for point B in the perpendicular beams contact example with normal and tangential contact [2]. . . . .	69
30	Perpendicular beams contact with red arrows and blue arrows representing respectively the “SP” contact model and the “SS” contact model. Simulation including normal and tangential contact [2]. . . . .	70
31	Representation of perpendicular beams model example with prescribed displacements including rotation [2]. . . . .	70

32	Reactions obtained for point B in the perpendicular beams contact example with normal and tangential contact including rotations [2]. . . . .	70
33	Perpendicular beams contact with red arrows and blue arrows representing respectively the “SP” contact model and the “SS” contact model. The simulation includes normal and tangential contact with rotations [2]. . . . .	71
34	Perpendicular beams contact with red arrows and blue arrows representing respectively the “SP” contact model and the “SS” contact model. The simulation includes normal and tangential contact with rotations. Top view at instant 1.96 s [2]. . . . .	71
35	Basis functions influence on the nodal reaction forces on five nodes [2]. . . . .	72
36	Prescribed displacements adopted in the objectivity test [2]. . . . .	73
37	Reaction forces and moments on point B in the objectivity test [2]. . . . .	73
38	Normal contact force at some configurations in the objectivity test [2]. . . . .	74
39	Convergence analysis for the perpendicular beams numerical example 5.1.1.1 for three different meshes with 30, 60, and 120 elements in each beam indicated respectively with suffixes “1”, “2”, and “3” [2]. . . . .	74
40	Representation of ring model example with prescribed displacements [2]. . . . .	75
41	Octagonal ring model finite element mesh in black color with nodes in orange color and contact surfaces in gray color [2]. . . . .	76
42	Reactions forces for point A and normal and friction forces obtained in the ring obstacle contact example [2]. . . . .	77
43	Normal and tangential contact forces at several instants of the ring obstacle example [2]. . . . .	78
44	Representation of wave-shaped model example with prescribed displacements [2]. . . . .	78
45	Wave-shaped obstacle finite element meshes in black color with nodes in orange color and contact surfaces in gray color [2]. . . . .	79
46	Reactions forces for point A and normal and friction forces obtained in the wave-shaped obstacle contact example [2]. . . . .	79

47	Normal and tangential contact forces at several instants of the wave-shaped obstacle example [2]. . . . .	80
48	Models overview [2]. . . . .	81
49	Horizontal beam left end reaction forces as illustrated in Table 8. Reaction forces indicated as MZB adapted from [24]. Extracted from [2]. . . . .	83
50	Twisting beams simulation setup for TB1 [3]. . . . .	84
51	Front view with rigid elements [3]. . . . .	84
52	Twisting beams example axial and moment reaction force at point E [3]. . . . .	85
53	Twisting beams example final configuration normal contact forces [3] and internal axial forces. . . . .	86
54	Parallel beams sliding simulation setup [3]. . . . .	87
55	Reaction forces and moment at point E [3]. . . . .	87
56	Sliding beams example normal forces [3]. . . . .	88
57	Parallel beams example. Contact elements in red and beam elements in gray [3]. . . . .	88
58	Parallel beams simulation setup [3]. . . . .	89
59	Parallel beams example final configuration [3]. . . . .	89
60	Parallel beams example results [3]. . . . .	89
61	Parallel beams simulation PB2 normal and frictional forces [3]. . . . .	90
62	Rotating beams example simulation setup [3]. . . . .	90
63	Rotating beam example results [3]. . . . .	91
64	Rotating beam example normal forces [3]. . . . .	92
65	Beam rotating on arc simulation setup [3]. . . . .	93
66	Beam rotating on arc results [3]. . . . .	93
67	Beam rotating on arc contact forces for RA2 [3]. . . . .	94
68	Representation of knot tightening model example with prescribed displacements [2]. . . . .	96

69	Reactions force components at point A obtained in the knot tightening contact example [2]. . . . .	97
70	First contact instant at 7 s in the knot tightening contact example [2]. . .	97
71	Normal contact forces at several instants in the knot tightening example [2].	98
72	Representation of textile shear model example with prescribed displacements [2]. . . . .	99
73	Model results obtained at the end of the textile shear example simulation [2].	99
74	Shear angle response with respect to the normalized shear force applied [2].	100
75	Biaxial tension model setup. . . . .	100
76	Biaxial tension models. Spline-based contact surface in red and structural beam model rendered in gray. . . . .	101
77	Biaxial tension results, “Experimental” in black from [7], “Surface” in blue from [1], and “Spline” in red from the spline-based contact formulation. . .	102
78	Normal contact forces obtained from the biaxial modeling of a glass fabric plain weave for $k = 1$ . . . . .	103

# LIST OF TABLES

1	Control points representing two quadratic finite elements simply joined. . .	32
2	Control meshes for $\Gamma_A$ and $\Gamma_B$ with new variables $h_A$ and $h_B$ [3]. . . . .	48
3	LCP solutions with their corresponding eigenvalues of $\mathbf{H}$ when $h_A = -0.5$ . . . . .	51
4	Initial position of nodes taken for basis function analysis. . . . .	72
5	Octagonal ring example simulation data. The variable $t$ is the total simulation time. . . . .	75
6	Wave-shaped obstacle example simulation data. . . . .	79
7	Displacement field adopted to reproduce perpendicular beams simulation. Rotations were applied around the beam center. . . . .	81
8	Simulation overview comparative figures at several time steps. . . . .	82
9	Rotating beam example displacements data. . . . .	90
10	Knot tighten example simulation data. . . . .	96
11	Textile shear example simulation data. . . . .	98
12	Objectivity test simulation displacements. . . . .	106

## LIST OF SYMBOLS

$\xi$	Spline convective coordinates
$N_{i,p}(\xi)$	Spline basis functions
$\mathbf{P}_i$	Spline control points
$\mathbf{C}(\xi)$	Spline physical meshes
$\Xi_i$	Knot vector
$\xi_i$	Lower value of knot vector span
$\xi_{i+1}$	Higher value of a knot vector span
$n_{fe}$	Number of quadratic finite elements
$n_{se}$	Number of spline elements
$\mathbf{c}$	Vector of convective coordinates
$c_A$	Convective coordinate from $\Gamma_A$
$c_B$	Convective coordinate from $\Gamma_B$
$\Gamma_A$	Contact element A
$\Gamma_B$	Contact element B
$\xi_A$	Spline convective coordinate from $\Gamma_A$
$\xi_B$	Spline convective coordinate from $\Gamma_B$
$\mathbf{d}$	Collection of degrees-of-freedom from $\Gamma_A$ and $\Gamma_B$
$\mathbf{d}_A$	Degrees-of-freedom from $\Gamma_A$
$\mathbf{d}_B$	Degrees-of-freedom from $\Gamma_B$
$\mathbf{u}_{AA}, \mathbf{u}_{AB},$ and $\mathbf{u}_{AC}$	Translational displacement vectors from $\Gamma_A$
$\mathbf{u}_{BA}, \mathbf{u}_{BB},$ and $\mathbf{u}_{BC}$	Translational displacement vectors from $\Gamma_B$
$g_e$	Gap effective
$\mathbf{g}$	Gap vector
$\mathbf{n}$	Gap vector normal direction
$r_A$	Cross-section radii from $\Gamma_A$
$r_B$	Cross-section radii from $\Gamma_B$
$f_1$	Objective function
$\mathbf{r}$	Residual function
$\mathbf{H}$	Hessian matrix
$\mathbf{f}_{ne}$	Normal elastic force
$\epsilon_{e1}$	Normal elastic contact parameter 1



$\epsilon_{e2}$	Normal elastic contact parameter 2
$\mathbf{f}_{nd}$	Damping normal force
$c_{nd}$	Damping constant
$\dot{\mathbf{g}}_n$	Normal relative velocity
$\mathbf{f}_n$	Normal contact force
$\mathbf{g}_t$	Tangential gap
$\gamma_A^\Delta$	Contact trajectory on $\Gamma_A$
$\gamma_B^\Delta$	Contact trajectory on $\Gamma_B$
$\gamma_{AB}^\Delta$	Contact trajectories difference from $\Gamma_A$ and $\Gamma_B$
$\mathbf{g}_t^\Delta$	Incremental tangential gap
$\mathbf{g}_t^{i+1}$	Total tangential gap
$\mathbf{g}_t^i$	Tangential gap accumulated
$\mathbf{Q}$	Rodrigues rotation tensor
$\mathbf{Q}^\Delta$	Rodrigues rotation tensor increment
$\theta^\Delta, \alpha, \mathbf{E}_\alpha,$ and $\mathbf{e}_\alpha$	Rodrigues rotation tensor parameters
$\mathbf{f}_{te}$	Tangential gap vector elastic contribution
$\epsilon_{te}$	Tangential penalty
$\mathbf{f}_{td}$	Tangential gap vector damping contribution
$c_{td}$	Viscous damping coefficient
$\dot{\mathbf{g}}_t$	Relative sliding velocity
$\mathbf{f}_{trial}$	Tangential trial force
$\mathbf{t}^{i+1}$	Frictional contact direction
$\mu_s$	Static frictional coefficient
$\mu_d$	Dynamic frictional coefficient
$\mathbf{g}_{t \text{ slide}}$	Tangential sliding gap
$\mathbf{g}_{t \text{ updated}}^{i+1}$	Updated tangential gap
$H_{AA}$	Hessian value when degeneration takes place in $\Gamma_B$
$H_{BB}$	Hessian value when degeneration takes place in $\Gamma_A$
$\lambda_1$ and $\lambda_2$	Hessian matrix eigenvalues
$h_A$ and $h_B$	Variable to change the overall spline's shape
$\text{tol}_\xi$	Tolerance associated with the knot span
$\text{tol}_c$	Tolerance associated with Hessian eigenvalues
$\mathbf{x}$	Kinematic description of a material point
$\zeta$	Beam axis convective coordinate
$\mathbf{a}$	Vector mapping all points of a beam cross-section
$\mathbf{e}_3$	Axis associated with a beam centerline

$e_1$ and $e_2$	Axis associated with a beam cross-section
$I$	Identity matrix of order three
$A$	Tensor associated with the Rodrigues rotation
$F$	Deformation gradient
$\nabla S$	Strain measure
$E$	Green-Lagrange strain tensor
$\eta$	Generalized beam axial strains
$\kappa$	Specific rotations
$\gamma$	Infinitesimal strain tensor with Voigt notation
$\tau$	Stress-strain expression using Hooke's law
$E$	Young's Modulus
$G$	Shear Modulus
$n$	Beam model equivalent forces
$m$	Beam model equivalent moments
$S_1$ and $S_2$	First moments of area
$I_1$ and $I_2$	Second moments of area
$I_{12}$	Product of inertia
$I_0$	Polar moment of inertia
$I_t$	Torsional inertia
$k$	Shear correction factor
$\sigma$	Vector of beam model forces and moments
$\varepsilon$	Vector of axial strains and specific rotations
$D$	Beam model constitutive matrix
$l$	Beam model length
$\bar{q}$	External generalized loads
$f$	Inertial forces and moments
$\delta W_i$	Internal forces contribution to the weak form
$\delta W_e$	External forces contribution to the weak form
$\delta T$	Inertial forces contribution to the weak form
$\delta W_n$	Normal contact contribution to the weak form
$\delta W_t$	Tangential contact contribution to the weak form
$y_n$	Number of yarns in each direction
$y_s$	In-plane yarns' spacing
$y_g$	Out-of-plane yarns' spacing or gap
$y_l$	Yarns' horizontal length
$y_c$	Yarns' crimp

# CONTENTS

<b>1</b>	<b>Context</b>	<b>21</b>
<b>2</b>	<b>Introduction</b>	<b>24</b>
2.1	Brief Description on the State-of-Art . . . . .	26
2.2	Objective . . . . .	28
2.3	Organization . . . . .	29
<b>3</b>	<b>Spline-Based Contact Formulation</b>	<b>30</b>
3.1	Spline-Based Surface . . . . .	30
3.2	Normal Contact Formulation . . . . .	35
3.2.1	Normal Interaction Law . . . . .	39
3.3	Tangential Contact Formulation . . . . .	40
3.3.1	Tangential Interaction Law . . . . .	43
3.4	Contact Problem Degeneration . . . . .	45
3.4.1	Contact Solution Characterization . . . . .	47
3.4.1.1	Curved Contact Problem . . . . .	49
3.4.1.2	Straight Contact Problem . . . . .	50
3.5	Numerical Strategy & Algorithm . . . . .	51
<b>4</b>	<b>Structural Theory</b>	<b>55</b>
4.1	Kinematics . . . . .	55
4.2	Constitutive Matrix . . . . .	56
4.3	Weak Form . . . . .	61
4.4	Giraffe Finite Element Solver . . . . .	62
4.4.1	Spline-Based Contact Implementation . . . . .	62

4.4.2	Textile Modeling . . . . .	63
<b>5</b>	<b>Numerical Examples</b>	<b>66</b>
5.1	Non-conformal Contact . . . . .	66
5.1.1	Perpendicular Beams . . . . .	66
5.1.1.1	Normal Contact . . . . .	66
5.1.1.2	Normal & Tangential Contact . . . . .	68
5.1.1.3	Normal & Tangential Contact with Rotations . . . . .	69
5.1.1.4	Basis Functions, Objectivity, and Convergence . . . . .	71
5.1.2	Octagonal Ring . . . . .	74
5.1.3	Wave-shaped Obstacle . . . . .	76
5.1.4	Alternative Smooth Contact Formulation . . . . .	80
5.2	Conformal Contact . . . . .	83
5.2.1	Twisting Beams . . . . .	83
5.2.2	Sliding Beams . . . . .	84
5.2.3	Parallel Beams . . . . .	85
5.2.4	Rotating Beam . . . . .	88
5.2.5	Beam Rotating on Arc . . . . .	92
<b>6</b>	<b>Textile Applications</b>	<b>95</b>
6.1	Knot Tighten . . . . .	95
6.2	Textile Shear . . . . .	97
6.3	Biaxial Tension . . . . .	100
<b>7</b>	<b>Conclusions</b>	<b>104</b>
7.1	Future Works . . . . .	105
	<b>Appendix A</b>	<b>106</b>

<b>Appendix B</b>	<b>107</b>
7.1 Weak Form Contribution . . . . .	107
7.2 Contact Tangent Operator . . . . .	109
7.3 Equations . . . . .	110
<b>References</b>	<b>112</b>

# 1 CONTEXT

This thesis condenses three papers produced by the candidate and co-authors [1, 2, 3] during the doctorate program. These papers are not chronologically presented in this thesis. The overall objective of the candidate project was to advance in the modeling of dry fabrics materials considering beam elements and contact formulations. All papers' results were developed within the Giraffe finite element solver [4]. The Giraffe is a finite element solver initially developed by the supervisor that is specially devoted to geometrically non-linear structural elements and contact formulations.

The first paper developed by the candidate and co-author, see [1], is focused on comparing results obtained from biaxial tension experiments and from the computational modeling of textiles, see Figure 1a. In [1] textile models are defined as a combination of a geometrically-exact beam theory and a well-established surface-to-surface contact formulation [5, 6]. This paper proved that this modeling strategy of textiles is capable of qualitatively reproducing biaxial tension experimental results. Moreover, this work showed the existence of multiple contact pairs where a single one would be expected, see Figure 1b. The existence of multiple contact pairs as seen in [1] is due to the contact surfaces' definition that is locally, and not entirely, smooth. In this sense, only  $C^0$  continuity is granted at the interface of contact surfaces simply joined. The existence of multiple contact forces served as motivation for the development of a  $C^1$  contact formulation based on a spline description.

The first work with the  $C^1$  spline-based contact formulation developed by the candidate and co-authors is presented in [2]. The formulation presented in this work includes a nonlinear normal contact constitutive law and a frictional law with their corresponding elastic and dissipative contributions. Despite the reasonable number of possibilities involving the  $C^1$  contact formulation and their constitutive laws, the formulation developed in [2] is limited to pointwise (non-conformal) contact scenarios, see Figure 2.

Moreover, conformal contact scenarios are particularly important in the dry fabrics field to model, for example, multiple fibers composing a yarn. This limitation and ap-

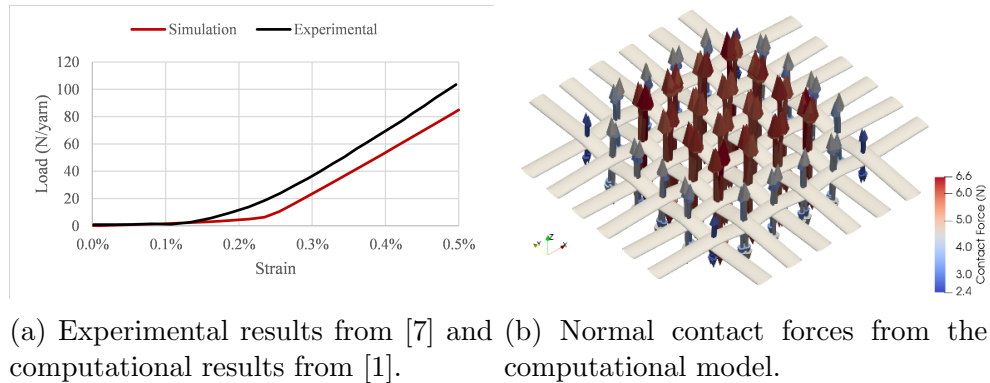


Figure 1: Comparison between experimental and computational results of the biaxial mechanical behavior of a textile. Extracted from [1].

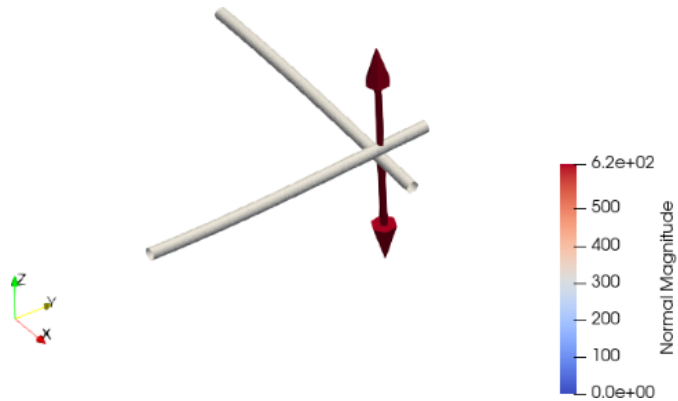


Figure 2: Non-conformal contact with the spline-based contact formulations. Extracted from [2].

plication motivated the candidate and co-authors to produce another paper including a three-criterion numerical strategy to handle conformal contact scenarios using the recent  $C^1$  spline-based contact formulation [3], see Figure 2. The paper with the  $C^1$  spline-based formulation to handle conformal contact scenarios is currently under review.

This thesis presents, according to the candidate's point of view, the main results and conclusions of the three papers produced. Moreover, it highlights the connection between these papers in proposing a contact model with a broad range of applications in the textile field.

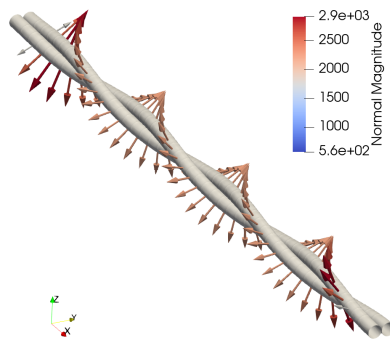


Figure 3: Conformal contact with the spline-based contact formulations.



## 2 INTRODUCTION

Mechanical contact between bodies is a relevant phenomenon in numerous practical applications, such as railways, cables, textile mechanics, and material forming, among others. However, its modeling is a non-trivial task from a physical-engineering perspective, since it can involve complex geometries, distinct constitutive equations, heat transfer, wear, and chemical reactions, among other effects. In engineering practical applications, it is particularly important to consider normal and tangential (friction) forces. There are several possibilities involving the contact modeling of solids considering them as rigid or flexible bodies. The Finite Element Method (FEM) is, however, particularly appealing when dealing with flexible bodies. In this context, it is convenient for contact formulations to take advantage of the underlying discretization leading to approaches such as node-to-node, node-to-surface, and surface-to-surface. For beam-to-beam contact, though, specific approaches need to be employed.

In node-to-node contact formulations [8, 9], the contact-candidate material points are defined *a priori*. The main drawback is the difficulty in predicting such points for large deformation scenarios if classical finite element discretizations are used, an exception is the virtual element method that allows node-to-node contact discretization even for large deformations, see [10]. In classical node-to-surface formulations [11, 12], a slave material point is projected during the deformation onto a master surface. Assuming a pointwise interaction, this approach defines the gap between the slave point and the master surface. It is able to handle large deformation scenarios. The main disadvantage is that the method has issues in passing the patch test, particularly when considering curved contact surfaces (see e.g.: [13, 14]). In surface-to-surface formulations [15, 16], the contact contribution to the weak form is directly calculated according to the contact interface area. This approach can be understood as an advancement when compared to the node-to-surface technique since the constraint is directly prescribed in the weak form considering its integral term with no *a priori* simplifications.

Unlike other mentioned contact approaches, the interaction involving beam elements

demands particular formulations [17, 18]. These may vary according to the beam cross-section, the approximation degree of the beam element (within a finite-element scheme), the degrees of freedom of the beam, the coordinate description of the beam, etc. Moreover, contact characterization depends deeply on the geometric description of the elements involved in every modeling technique. Even when considering locally smooth contact elements, a complete geometric description with a particular continuity level for the whole structure is highly desirable. Some immediate benefits of smooth discretizations are the absence of possible normal force jumps in the case of sliding between contact elements, a more precise geometric description for path-dependent tangential contact, and a potential reduction in the number of initially straight beam finite elements, frequently employed to describe in an approximated way a curved part.

Even considering smooth contact formulations, geometrical contact characterization is still a particular problem. Mathematically, one can present distinct descriptions for contacting elements involved. When addressing the problem of defining the contact patch on the interface only a few closed-form solutions are available. The seminal works of Hertz [19, 20] present some closed-form solutions for contact problems considering curvature radii of surfaces and adopting linear elastic materials.

In this context, a common approach for contact modeling is to combine a contact formulation with a solid/structural model. A compelling option for solid/structural model is, as mentioned, the FEM. The main advantage of FEM formulation is its great versatility with a myriad of applications. Moreover, FEM formulations introduce always a discretization of the problem domain (here including the contact surfaces), which can lead to difficulties in handling contact. These strategies, however, are deeply dependent on the discretization level of FEM meshes that are usually  $C^0$ . Moreover, sharp corners in  $C^0$  meshes lead to singularities in normal vector description, which can potentially lead to convergence difficulties. To circumvent this issue a possible procedure is to decouple the contact formulation from the solid/structural model by introducing a smooth geometric description such as splines, Bézier curves, or Hermite polynomials, see [21, 22, 23, 24, 2]. The objective of these smooth geometrical descriptions is to avoid possible continuity issues related to ill-defined geometries.

In a hypothetical scenario in which contact is characterized as pointwise, it is possible to formulate the contact interaction through a pair of material points (in distinct bodies or within a body, in case of self-contact). Material points can be viewed as locations where contact forces act, while geometrical entities, such as surfaces or curves, define domains where they are searched for. Figure 4a illustrates a just-touching pointwise contact

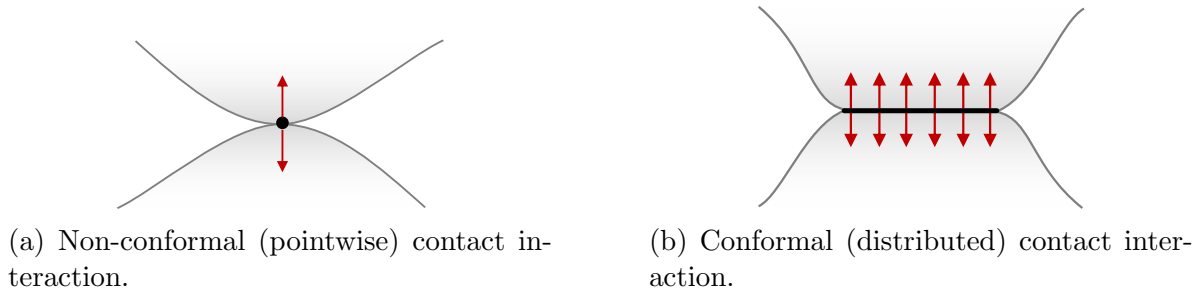


Figure 4: Contact interaction between two bodies.

interaction. The determination of material points is classically defined as the minimum distance between a pair of geometrical entities from bodies (closest point projection). The minimum distance problem between two bodies can be geometrically interpreted as finding a line segment that respects some orthogonality conditions associated with the body's description. Moreover, the minimum distance problem uniqueness, and by consequence the orthogonality conditions, relies on the convexity of the contact problem. In cases of non-convexity, the existence and/or uniqueness of the contact problem is not granted. Though these cases may seem like an exception, they are frequently observed in practical problems involving conformal contact. Figure 4b illustrates a conformal contact scenario with distributed contact forces. In such cases, an alternative approach is to weak the orthogonality conditions by fixing *a priori* one or more coordinates at geometrical entities. This procedure can be regarded as a degeneration of the original contact problem as seen in [25, 26, 27, 28]. A detailed discussion regarding degeneration of contact problems involving surfaces is presented in [29].

## 2.1 Brief Description on the State-of-Art

The idea of smooth contact elements is not new. Therefore many authors dedicated efforts toward that direction. In [30] a master-slave formulation for the contact of surfaces described with splines and Bézier curves including friction is presented and explored in simulations with large deformations. In [31] a variational formulation is developed for the frictional contact in 2D involving surfaces described with splines and cubic Hermite polynomials. In [21] a surface-to-surface formulation based on  $C^1$  cubic splines is presented for the normal and tangential contact in 2D applications. The mechanical constraints are imposed by Lagrange multipliers within a formulation using variational inequalities. Similar formulations can be found in earlier work, see, for two-dimensional for three-dimensional discretizations, respectively, in [32] and in [22]. In [33] a smooth segment described by three Hermite polynomials is introduced to model the beam centerline of two

3D adjacent finite elements. The author focuses on frictional contact ruled by a penalty method for beams with circular cross-section without rotational degrees-of-freedom. In [34] the concept of proximity zones to formulate the contact in a smooth way is introduced. Woven fabrics are investigated with this contact formulation which is based on the penalty method. In [35], the formulation is extended to more complex problems such as the knot tightening with multiple yarns. In [36] a curve-to-curve geometrically-exact contact formulation in a covariant form is consistently developed. It can be viewed either as the contact between sharp edges of full 3D bodies (edge-to-edge) or as the contact of beams' centerlines (beam-to-beam). For that, the contact elements are depicted in terms of a Frenet-Serret model for 3D curves. This formulation also includes normal and tangential interactions imposed by the penalty method.

In [23] a surface-to-surface contact formulation based on NURBS is combined in an Isogeometric Analysis (IGA) framework. This formulation is applied to frictionless contact. In [37] a mortar-based frictional contact formulation with NURBS is presented. The NURBS contact elements are directly inherited from IGA elements. A similar strategy is adopted in [38] for modeling dry woven fabrics. In [39] beam finite elements and contact elements are described by  $C^1$  Hermite polynomials in a variational manner. The formulation is applied for normal contact of slender circular beams considering a penalty potential contribution to the weak form. In [26] a geometrically-exact beam theory for elliptical cross-sections is combined with Bézier curves to describe a surface-to-surface contact formulation. In [40], a geometrically-exact beam theory in the context of IGA is presented that describes contact by splines as centerlines. For the contact modeling, a Differential Variational Inequality (DVI) including normal and tangential formulations is adopted.

Moreover, only a few works presented strategies to properly address conformal beam-to-beam contact scenarios. In [36, 41], several cases of contact problems existence and uniqueness are discussed in terms of curvature vectors ( $\kappa\mathbf{v}$ ) and tangent vectors ( $\boldsymbol{\tau}$ ). As a solution for contact problem convexity issues, the authors propose a generalized minimum distance search procedure including not only surfaces but also corners and edges. This procedure can be interpreted as a degeneration of the original surface-to-surface contact problem in the herein terminology, taken from works [25, 27].

In [42, 43], a beam contact formulation including normal and frictional interactions is introduced to handle very acute angles defined by beam centerlines. The author proposed a strategy that, from a single pointwise interaction, introduces two additional pairs of contact points enhancing the contact description. The proposed strategy, however, relies

on the existence of an initial single closest point projection to later add the pair of contact points. As a consequence, the proposed strategy seems to be non-suitable for representing conformal contact scenarios.

In [34, 35, 44, 45], a particular strategy is developed to handle normal and tangential contact scenarios. The idea involves several steps including closest point detection, as in classical master-slave contact formulations, proximity zones to limit convective coordinates span and, finally, intermediate geometries to project candidate points to contact. The contact formulation is successfully applied to textile simulations of dozens of yarns. To handle conformal contact, an alternative method based on the average of beams centerlines tangents is defined for the intermediate geometries.

In [46, 47, 39], cubic Hermite polynomials with  $C^1$  continuity are used to describe beam centerlines and normal contact interactions. In [46] a line-to-line formulation is developed to handle conformal contact of beams. The authors evaluate the existence and uniqueness of contact problems by the angle defined by the beam centerlines (contact angle), the closest point distance, and the curvature of the beam centerline. In [47] an all-angle beam contact (ABC) approach is presented to automatically switch between point-to-point and line-to-line contact formulations. The transition between these formulations is derived in a variationally consistent manner and a force-based model, but the presentation is limited to frictionless interaction. In [39] the ABC contact formulation is expanded incorporating a geometrically-exact Simo-Reissner beam theory.

## 2.2 Objective

The objective of this work is to propose a general spline-based smooth contact formulation for conformal and non-conformal beam-to-beam contact, with circular cross-sections. A particular numerical strategy based on three criteria is introduced to handle conformal contact scenarios. The spline nature guarantees a smooth description of the contact surfaces of structures as a whole, represented by a set of elements.

Other specific thesis objectives are:

- Develop a contact formulation that can be used together with general beam structural formulations, even with a non-smooth FEM mesh;
- Consider normal and tangential contact interactions with their elastic and dissipative contributions;

- Test the contact formulation in challenging problems involving conformal and non-conformal scenarios and their transitions;
- Apply the proposed contact formulation in numerical examples in textile applications.

## 2.3 Organization

This work is structured as follows. In Chapter 3 the spline-based  $C^1$ -continuous formulation for conformal and non-conformal contact is introduced with the normal and tangential interaction contributions. In Chapter 4 the geometrically-exact beam kinematics and constitutive matrix are briefly presented and the main references are mentioned. The Giraffe finite element solver is introduced and the spline-based contact formulation implementation is described. An originally developed software to aid in the textile modeling in the Giraffe solver is presented. In Chapter 5 numerous examples of conformal and non-conformal contacts are explored. These examples include several studies including static and dynamic simulations, normal and frictional contact, nonlinear interface law, etc. In Chapter 6 some examples in the context of dry fabrics modeling are explored. The objective of these examples is to provide a glimpse of applications in the textiles field. In Chapter 7 the conclusions regarding the  $C^1$  spline-based contact formulation developed are drawn and some future works are proposed.

### 3 SPLINE-BASED CONTACT FORMULATION

This chapter presents the spline-based contact formulation for conformal and non-conformal scenarios, including normal and tangential interactions [2, 3].

#### 3.1 Spline-Based Surface

A possible way to mathematically construct a spline is to recursively calculate specific basis functions from a specific vector known as knot vector. The knot vector is a non-decreasing vector of real numbers that sets, through knot spans, convective coordinate spans for the whole spline. The knot vector also controls the continuity level between spline elements. The continuity between two spline elements is equal to  $C^{p-m}$  where “ $p$ ” is the degree and “ $m$ ” is the multiplicity of the value in the knot vector. Since the objective is to work with quadratic splines with  $C^1$  continuity, all knot span values are taken with multiplicity  $m = 1$ , except at the first and last values which are defined with multiplicity  $m = 3$  to enforce interpolation. For the proposed formulation the knot vector is assumed as uniform, which means that knot vector values are equally spaced.

Considering a given knot vector, it is possible to define spline basis functions as

$$N_{i,0}(\xi) = \begin{cases} 1 & \text{if } \xi_i \leq \xi \leq \xi_{i+1} \\ 0 & \text{otherwise} \end{cases} \quad (3.1)$$

$$N_{i,p}(\xi) = \frac{\xi - \xi_i}{\xi_{i+p} - \xi_i} N_{i,p-1}(\xi) + \frac{\xi_{i+p+1} - \xi}{\xi_{i+p+1} - \xi_{i+1}} N_{i+1,p-1}(\xi).$$

where  $\xi$  is the convective coordinate with  $N_{i,p}(\xi)$  being recursively (using the Cox-de Boor formula [48]) calculated according to a desirable degree “ $p$ ”. The  $N_{i,p}(\xi)$  terms are considered only if the denominator is not zero to avoid indeterminations. Figure 5

illustrates step-by-step the procedure to produce five quadratic basis functions based on a knot vector equal to  $\Xi = \{0, 0, 0, 1/3, 2/3, 1, 1, 1\}$ . The dashed lines in Figure 5 indicate the three knot spans.

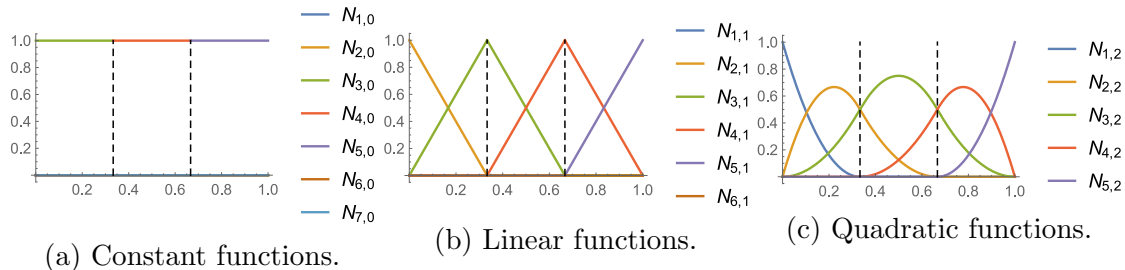


Figure 5: Basis functions calculated based on a knot vector  $\Xi = \{0, 0, 0, 1/3, 2/3, 1, 1, 1\}$  for two quadratic beam elements. Dashed lines represent the knot spans (spline elements) [2].

It is possible to note that for any given value of  $\xi$  in the constant, linear, or quadratic basis, the sum of the functions equals unity, see Figure 5. This characteristic implies that these functions can be used to split a given information (e.g. value or vector) with no losses. Moreover, Figure 5 also shows that the quadratic basis function preserves  $C^1$  continuity not only inside the knot spans but also between them. Once the basis functions are established, the spline is defined as

$$\mathbf{C}(\xi) = \sum_{i=1}^n N_{i,p}(\xi) \mathbf{P}_i. \quad (3.2)$$

where  $\mathbf{C}(\xi)$  represents the physical mesh,  $N_{i,p}(\xi)$  are the basis functions and  $\mathbf{P}_i$  are the control points defining a control mesh. The control mesh is an interpolatory mesh defined by control points while the physical mesh, which is often non-interpolatory, stands for the spline geometric description [49, 50].

Figure 6a illustrates a spline with a solid line (divided into two black lines and a red curve obtained for each knot span) representing the physical mesh and a dashed line with control points in orange representing the control mesh. Though any control mesh could be used to produce the spline, the defined control mesh was intentionally adopted to represent two straight quadratic finite elements. The particular choice of finite element nodes as control points highlights the link between the spline formulation and the structural formulation. Additionally, it shows how the spline smoothes the eventual sharp edges of classical straight finite elements discretization. The spline is, therefore, an approximation of the finite elements geometry. Moreover, this approximation can be reduced by refining

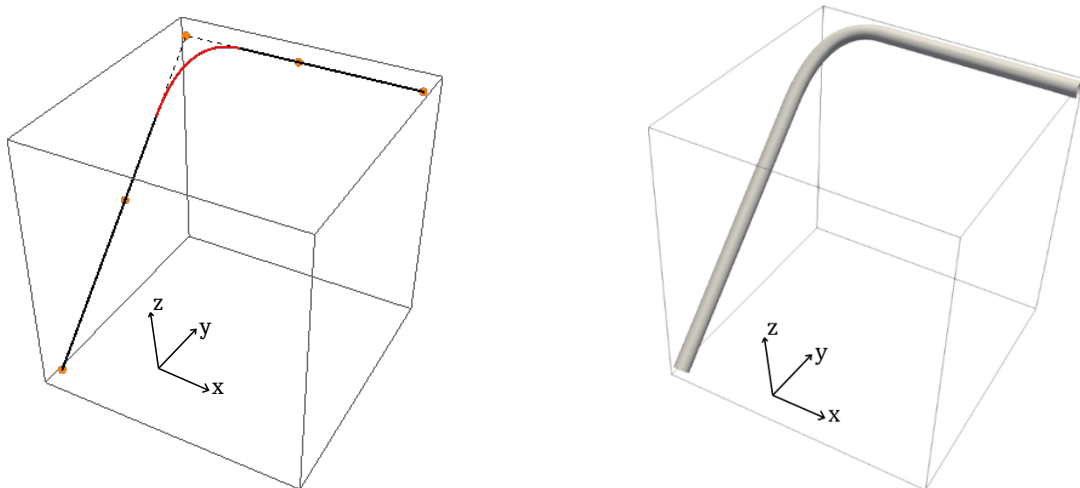


Table 1: Control points representing two quadratic finite elements simply joined.

$P_1 = (0, 0, 0)$
$P_2 = (0, 1, 1)$
$P_3 = (0, 2, 2)$
$P_4 = (1, 2, 2)$
$P_5 = (2, 2, 2)$

the finite elements mesh. The spline in Figure 6a combines the quadratic basis functions presented in Figure 5c and the control points presented in Table 1.

Considering the spline definition, it is feasible now to establish a spline-based surface by sweeping a circular profile along the whole spline curve in space. In this surface representation, the spline depicts a centerline while a circle radius characterizes the outer surface. Figure 6b illustrates a spline-based surface directly obtained from the spline presented in Figure 6a. A major advantage of spline-based surfaces is their natural smoothness, guaranteed by the spline definition. Moreover, it permits the definition of a desired continuity level in advance. In this work, a quadratic spline formulation with  $C^1$  continuity is adopted through all spline elements, except at the tips, where the spline is taken as interpolatory at control points. The choice for the quadratic spline formulation is the simplest one, keeping a minimum desirable smoothness.



(a) Spline control mesh represented by the dashed line with control points in orange. Spline physical mesh represented by the black lines and red curve. The red curve represents a single patch defined by a knot span.

(b) Spline-based surface obtained by sweeping a circular profile along the whole spline curve in space.

Figure 6: Spline and spline-based surface [2].

Though Figure 6b illustrates a spline-based surface that may be associated with a

single body, it is convenient for contact formulations to split that surface into smaller parts. These parts, which can be viewed as contact elements, hold all necessary geometrical information. For the proposed contact formulation a contact element consists of a spline element linked with a knot span and a radius. It is important to observe that the procedure of splitting the original spline into spline elements should preserve all original geometric properties.

Considering then quadratic basis functions and a generic knot span  $[\xi_i, \xi_{i+1}[$  with  $\xi_i \neq \xi_{i+1}$  the corresponding spline element knot vector is defined as

$$\Xi_i = \{\xi_{i-2}, \xi_{i-1}, \xi_i, \xi_{i+1}, \xi_{i+2}, \xi_{i+3}\} \quad (3.3)$$

where  $\Xi_i$  represents a subdomain of the original knot vector  $\xi$ . Figure 7 illustrates basis functions calculated for the spline elements based on the original knot vector  $\Xi = \{0, 0, 0, 1/3, 2/3, 1, 1, 1\}$  presented in Figure 5.

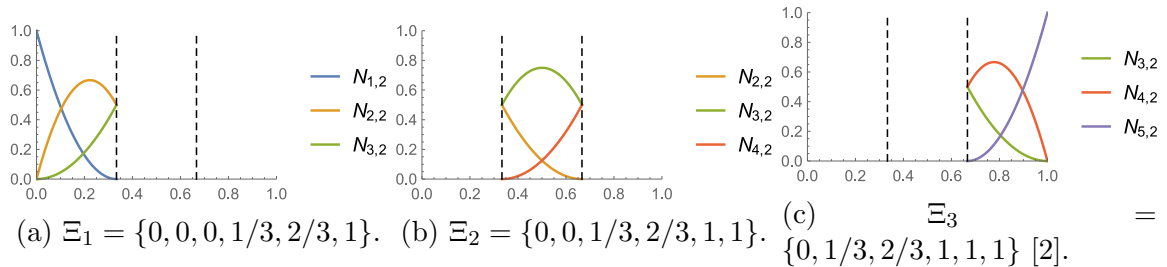


Figure 7: Basis functions calculated for the spline elements based on the original knot vector  $\Xi = \{0, 0, 0, 1/3, 2/3, 1, 1, 1\}$ .

As shown in Figure 7, each spline element comprises a set of three basis functions, in contrast to the five basis functions presented in Figure 5c. In fact, the basis functions presented in Figure 5c and Figure 7 are the same, except for the knot spans imposed according to the spline element in the analysis. Moreover, as each basis function is uniquely associated with a control point, see (3.2), it is possible to define control points that rule each spline element.

Therefore, a spline element is completely defined by a knot vector (based on the original knot vector) and a set of control points (according to the control mesh). Following the proposed formulation with quadratic spline elements, a set of three control points is necessary for each spline element.

Figure 8a to 8c illustrate the physical mesh of three spline elements based on the original spline of Figure 6a. Figure 8d to 8f present the corresponding spline-based surface

regions associated with the original spline-based surface presented in Figure 6b. Such regions are to be used herein to establish contact elements.

It is noteworthy that some points are shared between spline elements since they share basis functions (in different knot spans). This fact implies that contacts acting simultaneously in neighbor spline elements may affect a particular shared control point at the same time. Additionally, the number of spline elements is different to the number of finite elements. The number of spline elements is equal to the number of valid knot spans ( $\xi_i \neq \xi_{i+1}$ ) in the knot vector. For example, in the example here discussed for 2 quadratic finite elements 3 spline elements are necessary. Considering quadratic spline elements combined with quadratic finite elements simply joined ( $n_{fe}$ ), the number of contact elements is  $n_{se} = 2n_{fe} - 1$ .

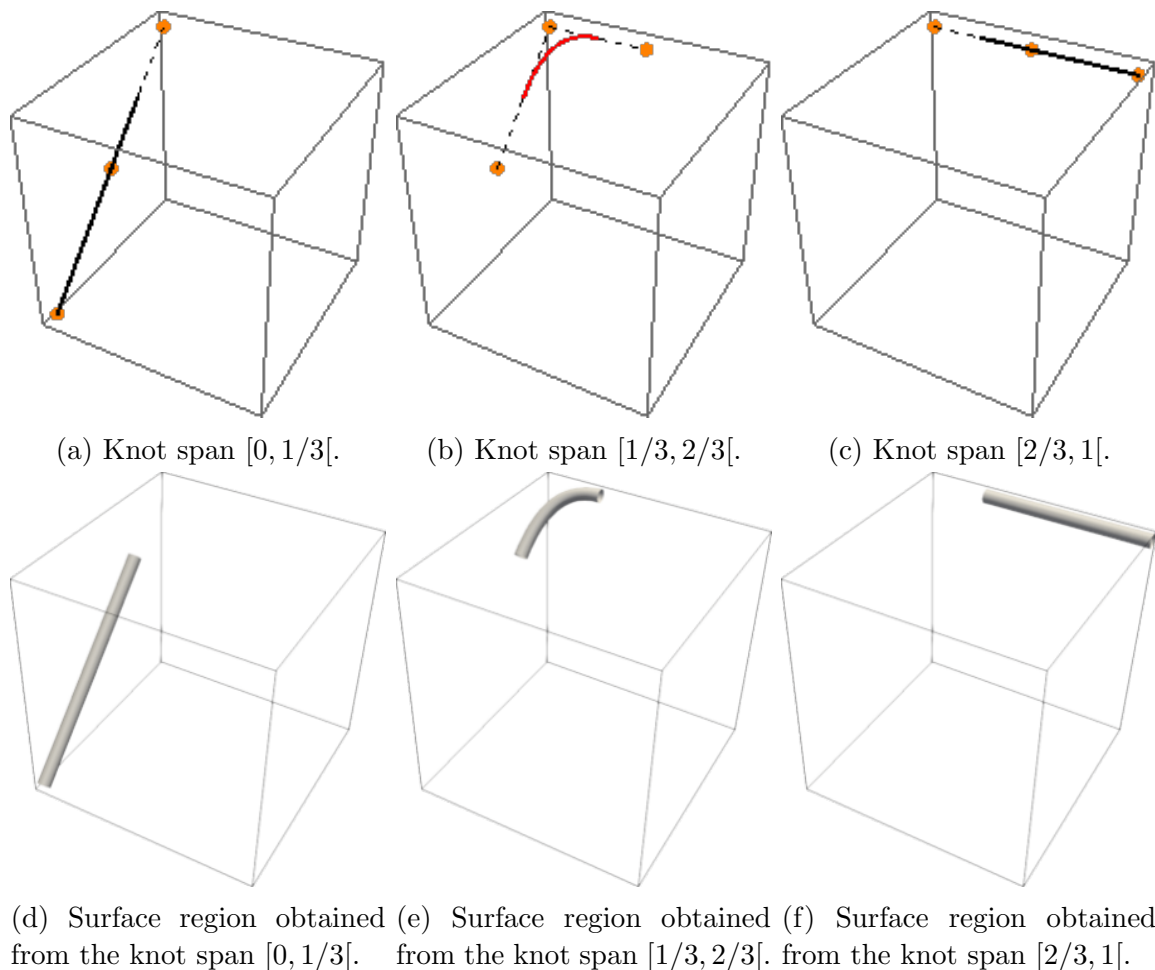


Figure 8: Representation of three spline elements and three spline-based surface regions based on the original spline presented in Figure 5 [2].

## 3.2 Normal Contact Formulation

Contact is characterized by the mechanical interaction between two bodies, taking place on portions of the surface of bodies (or within the same body, in the case of self-contact). In this work, each pair of contact elements uniquely defines a pointwise action-reaction.

The search for contact pairs is usually performed, roughly in two phases. The first phase consists of a global search. This phase aims to quickly identify pairs of contact elements prone to contact. This search uses a simple pinball check associated with points concerning contact elements [51]. In the pinball check a radius is defined for each contact element. These radii are then used to evaluate which contact pairs are prone to contact. Figure 9a highlights in red color a pair of spline elements from splines  $\Gamma_A$  and  $\Gamma_B$  which are prone to contact according to the pinball overlap.

Once all pairs of contact candidates are defined by the global search, a local search is performed. This local search seeks points at both contact elements where the contact interaction may take place. This nonlinear search can involve complex surfaces and is denoted as the Local Contact Problem (LCP). A detailed discussion of the LCP is presented in [29]. Moreover, depending on the configuration of the contact elements in space, there might be cases for which the LCP is ill-defined (such as conformal contact).

Considering however an LCP solution, corresponding to materials points, it is possible to formulate the contact interaction. In the case of penetration, an interface law is applied and its corresponding potential is calculated. Alternatively, one may adopt Lagrange multipliers to impose the non-penetration condition. The main drawback of using Lagrange multipliers is the lack of a physical interface law that may be quite convenient to represent contact interaction. The global and local contact searches are repeated at each simulation's time-step as the model evolves.

Figure 9b illustrates a LCP solution  $\bar{\mathbf{c}}^T = [\bar{c}_A, \bar{c}_B]^T$  for two spline elements  $\Gamma_A$  and  $\Gamma_B$ . The red vector  $\mathbf{g}$  indicates the minimum distance, or closest point projection, between  $\Gamma_A$  and  $\Gamma_B$ . From now on, a LCP solution is indicated by a set of convective coordinates  $\bar{\mathbf{c}}^T = [\bar{c}_A \ \bar{c}_B]^T = [\bar{\xi}_A \ \bar{\xi}_B]^T$ .

Contact elements are often described in terms of convective coordinates and generalized displacements. This kind of formalism is very useful for contact problems as shown for beams, shells, and general polyhedra [5, 6, 52]. Moreover, this formalism permits some mathematical manipulations (known as LCP degenerations) to handle specifically

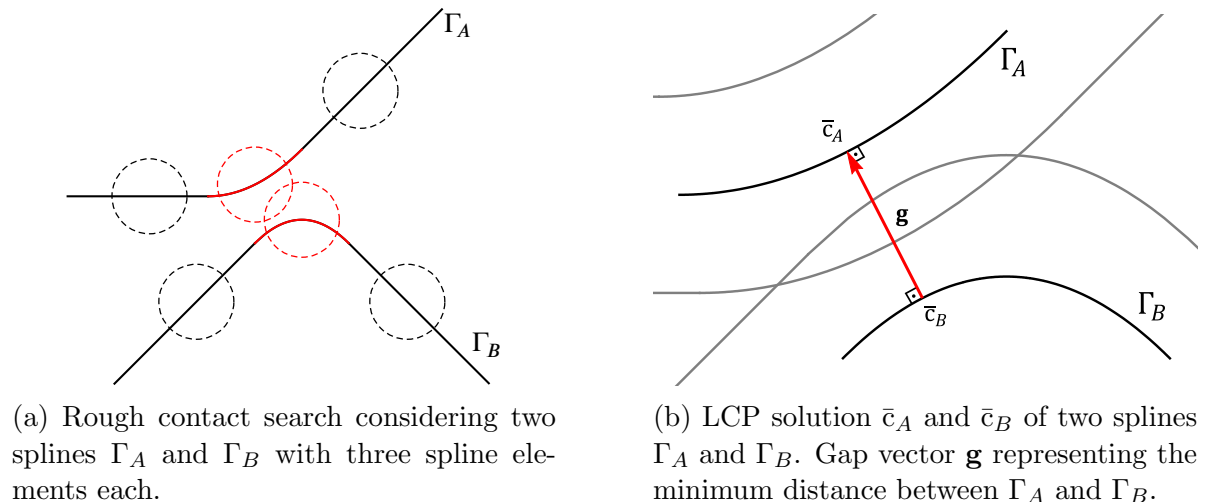


Figure 9: Representations of the rough contact search and the local contact search [2].

challenging conformal contact scenarios, see [27, 29]. In this work, the spline coordinates are defined as the convective coordinates. Furthermore, the generalized displacements are taken as translational displacements associated with the control points inherited from the finite element mesh. An immediate effect of this approach is a significant simplification of the LCP when compared to surfaces [29]. Within this approach, the LCP leads to a minimum distance problem involving two spline elements.

The convective coordinates range of validity of spline elements is naturally linked to their knot spans. As a result, it is convenient to describe the convective coordinates of the spline elements  $\Gamma_A$  and  $\Gamma_B$  respectively as  $c_A = \xi_A$  and  $c_B = \xi_B$ . It is still convenient to combine these values into a single vector of convective coordinates  $\mathbf{c}$  as

$$\mathbf{c} = \begin{bmatrix} c_A \\ c_B \end{bmatrix} = \begin{bmatrix} \xi_A \\ \xi_B \end{bmatrix} \quad (3.4)$$

The generalized displacements of any contact element should encompass, as much as possible, the degrees-of-freedom involved in the contact element deformation. For a spline element, defined by three control points, three displacement vectors are necessary. The generalized displacements of the spline elements  $\Gamma_A$  and  $\Gamma_B$  can be therefore expressed by  $\mathbf{d}_A = [\mathbf{u}_{AA}^T \ \mathbf{u}_{AB}^T \ \mathbf{u}_{AC}^T]$  and  $\mathbf{d}_B = [\mathbf{u}_{BA}^T \ \mathbf{u}_{BB}^T \ \mathbf{u}_{BC}^T]$ . In this context, rotational degrees-of-freedom are not included in the contact formulation description, though present in the finite element formulation. Such particularity leads to a broader and more versatile approach since only nodal positions and generalized displacements are necessary. Figure 10 illustrates the generalized displacements  $\mathbf{d}_A$  at the three control points from a spline el-

ement. Once again, it is convenient to concatenate the generalized displacements into a single vector  $\mathbf{d}$  as

$$\mathbf{d} = \begin{bmatrix} \mathbf{d}_A \\ \mathbf{d}_B \end{bmatrix} = [\mathbf{u}_{AA}^T \ \mathbf{u}_{AB}^T \ \mathbf{u}_{AC}^T \ \mathbf{u}_{BA}^T \ \mathbf{u}_{BB}^T \ \mathbf{u}_{BC}^T]^T \quad (3.5)$$

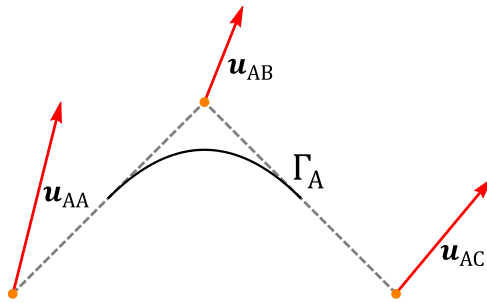


Figure 10: Spline element in black with a gray dashed line control mesh and orange control points. Red arrows indicating generalized displacements  $\mathbf{u}_{AA}$ ,  $\mathbf{u}_{AB}$ , and  $\mathbf{u}_{AC}$ , which rule the position of control points [2].

Finally, the spline elements  $\Gamma_A$  and  $\Gamma_B$ , prone to contact, are fully parametrized by their convective coordinate  $c_A$  and  $c_B$ , and their generalized displacement vectors  $\mathbf{d}_A$  and  $\mathbf{d}_B$ . The relation between the contact elements and the spline formulation is highlighted by the convective coordinate  $c_A$  and  $c_B$  taken respectively as  $\xi_A$  and  $\xi_B$  and by the generalized displacement vectors  $\mathbf{d}$  embedded in the points  $\mathbf{P}_i$  of the control mesh. Thus, the spline elements  $\Gamma_A$  and  $\Gamma_B$  are defined as

$$\begin{aligned} \Gamma_A(c_A, \mathbf{d}_A) &= \mathbf{C}_A(\xi_A) \text{ and} \\ \Gamma_B(c_B, \mathbf{d}_B) &= \mathbf{C}_B(\xi_B). \end{aligned} \quad (3.6)$$

With that, one can properly quantify and address contact interaction. An important value to characterize the contact interaction is the effective gap. A scalar effective gap  $g_e$  is defined as

$$g_e = \hat{g}_e(\mathbf{c}, \mathbf{d}) = \|\Gamma_A - \Gamma_B\| - (r_A + r_B), \quad (3.7)$$

where  $r_A$  and  $r_B$  are the beam cross-section radii associated with  $\Gamma_A$  and  $\Gamma_B$ , respectively. A negative sign of  $g_e$  characterizes the contact interaction. The quantity  $g_e$  is always evaluated at an LCP solution  $\bar{\mathbf{c}}$ , which corresponds to material points in spline elements

that present the minimum distance for a given configuration defined by  $\bar{\mathbf{d}}$  (see Figure 9b). Note that the scalar  $g_e$  is calculated with respect to the spline convective coordinates. This strategy is only valid for circular cross-sections that sweep the spline as the center [17]. Moreover, it is convenient now to formally introduce two important vectors associated with two spline elements  $\Gamma_A$  and  $\Gamma_B$ , the gap vector  $\mathbf{g}$  and its normal  $\mathbf{n}$ . The gap vector  $\mathbf{g}$  is given by

$$\mathbf{g} = \hat{\mathbf{g}}(\mathbf{c}, \mathbf{d}) = \Gamma_A - \Gamma_B, \quad (3.8)$$

and its normal  $\mathbf{n}$ , by definition, follows from

$$\mathbf{n} = \hat{\mathbf{n}}(\mathbf{c}, \mathbf{d}) = \frac{\Gamma_A - \Gamma_B}{\|\Gamma_A - \Gamma_B\|}. \quad (3.9)$$

The gap vector  $\mathbf{g}$  is particularly important since it mathematically expresses the contact elements' distance with all variables regarding the convective coordinates and degrees-of-freedom. Considering then a gap vector  $\mathbf{g}$ , it is convenient to define an objective function  $f_1$  associated with a quadratic expression of the distance between the spline elements. The objective function  $f_1$  is defined, considering the gap vector  $\mathbf{g}$  in (3.8), as

$$f_1 = \frac{1}{2} \mathbf{g} \cdot \mathbf{g}. \quad (3.10)$$

The LCP can be in consequence calculated as a stationary point of the objective function  $f_1$ , representing geometrically an orthogonality condition. In this context, the LCP can be expressed as

$$\mathbf{r} = \nabla f_1 = \begin{bmatrix} \Gamma_{A,\xi_A} \cdot \mathbf{g} \\ -\Gamma_{B,\xi_B} \cdot \mathbf{g} \end{bmatrix} = \begin{bmatrix} 0 \\ 0 \end{bmatrix} \quad (3.11)$$

where  $\mathbf{r}$  is a residual function, with  $\Gamma_{A,\xi_A}$  and  $\Gamma_{B,\xi_B}$  denoting partial derivatives with respect to their own convective coordinates. Once the condition presented in (3.11) is fulfilled, a LCP solution is obtained as a pair of convective coordinates corresponding to material points in each spline element within their valid knot spans (see Figure 9b).

A trust-region (TR) optimization framework [53, 54] is adopted to solve the nonlinear system expressed in (3.11).

Furthermore, it is still convenient to introduce a Hessian matrix  $\mathbf{H}$  concerning the objective function  $f_1$ . The Hessian matrix  $\mathbf{H}$  is calculated as

$$\mathbf{H} = \mathbf{r}_{,\mathbf{c}} = \nabla^2 f_1 = \begin{bmatrix} \mathbf{g} \cdot \Gamma_{A,\xi_A \xi_A} + \Gamma_{A,\xi_A} \cdot \Gamma_{A,\xi_A} & -\Gamma_{B,\xi_B} \cdot \Gamma_{A,\xi_A} \\ -\Gamma_{B,\xi_B} \cdot \Gamma_{A,\xi_A} & -\mathbf{g} \cdot \Gamma_{B,\xi_B \xi_B} + \Gamma_{B,\xi_B} \cdot \Gamma_{B,\xi_B} \end{bmatrix}. \quad (3.12)$$

The Hessian matrix presented in (3.12) is very useful in the characterization of a LCP solution  $\bar{\mathbf{c}}$  as further presented.

### 3.2.1 Normal Interaction Law

Once the penetration value is determined, one needs a method to impose the non-penetration mechanical constraint. The Lagrange multipliers method is a possibility, with the drawback of the introduction of extra unknowns, but with the capability of imposing the non-penetration condition exactly. The penalty method is another possible choice, allowing controlled penetrations. The penalty method can however be used to introduce local geometric effects by embedding these in an interface law, activated by a penetration evaluation given by the modulus of  $\mathbf{g}_e$ .

The definition of an interface (compliance) law is a central issue on this context. The compliance law of a pointwise fashioned contact should be able to capture the geometry (sharp, smooth, imperfections, etc.) and the material (elastic, viscoelastic, plastic, etc.) behavior of the bodies in contact. The classical work by Hertz presented the elastic normal contact problem involving some well-defined geometries parametrized by quadrics, able to represent locally the surfaces of spheres and cylinders [19]. In practical problems, the contact interaction between bodies is often characterized by a nonlinear interface law. In this work, a broad nonlinear normal elastic force  $\mathbf{f}_{ne}$  is adopted. The compliance law associated with  $\mathbf{f}_{ne}$  is defined as

$$\mathbf{f}_{ne} = \epsilon_{e1} |\mathbf{g}_e|^{\epsilon_{e2}} \left( \frac{\mathbf{g}_e}{|\mathbf{g}_e|} \right) \mathbf{n} \quad (3.13)$$

where  $\epsilon_{e1}$  and  $\epsilon_{e2}$  are parameters to be defined. The dotted line in Figure 11 illustrates a nonlinear compliance law for  $\epsilon_{e1} = 4E6 \text{ mN/m}^{2.613}$  and  $\epsilon_{e2} = 2.613$ .



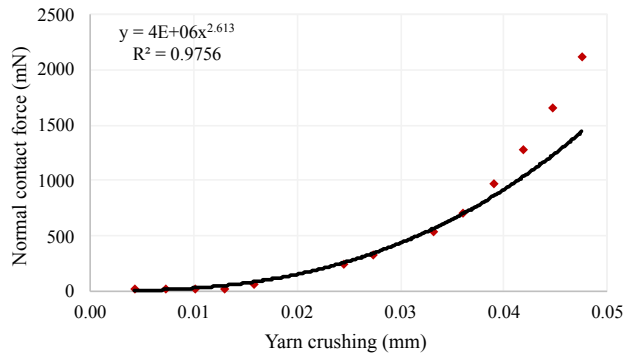


Figure 11: Normal contact compliance law from [55] proposed for  $\mathbf{f}_{ne}$  as red marks and approximated by a power trendline as a black solid line. Compliance law adopted in the numerical example of textile shear [2].

Though simple, equation (3.13) embraces several scenarios when combined with the pointwise contact interaction. It allows, for example, to impose compliance laws directly obtained from experiments, regardless of the overwhelming complexity of contact micromechanics. Another possibility for a normal interface law is a nonlinear law that behaves as a barrier, see [52].

Additionally, to account for dissipative effects, a linear damper is introduced in the normal interaction law. This normal damper is defined as

$$\mathbf{f}_{nd} = c_{nd}\dot{\mathbf{g}}_n \quad (3.14)$$

where  $c_{nd}$  is the damping constant and  $\dot{\mathbf{g}}_n$  is the normal relative velocity at the contact interface in normal direction as detailed in [27]. The normal force is then defined, considering elastic and dissipative contributions, as

$$\mathbf{f}_n = \mathbf{f}_{ne} + \mathbf{f}_{nd}. \quad (3.15)$$

### 3.3 Tangential Contact Formulation

The frictional force depends on the contact evolution during a certain time period. A possible way to quantify this force is to establish a tangential gap vector  $\mathbf{g}_t$ . The tangential gap can be viewed as a measure of the relative sliding of material points in contact.

To define the tangential gap, it is convenient first to define two auxiliary vectors as  $\gamma_A^\Delta$  and  $\gamma_B^\Delta$ . These vectors denote, in each spline element  $\Gamma_A$  and  $\Gamma_B$ , the contact trajectory of a material point between two consecutive configurations. From now on the superscript  $\Delta$  stands for a change from configurations “ $i$ ” to “ $i + 1$ ” within a time step, as illustrated in Figure 12. For sufficiently smooth surfaces and small timesteps, the contact trajectory vectors  $\gamma_A^\Delta$  and  $\gamma_B^\Delta$  can be defined as

$$\begin{aligned}\gamma_A^\Delta &= \Gamma_A(\mathbf{c}_A^{i+1}, \mathbf{d}_A^{i+1}) - \Gamma_A(\mathbf{c}_A^i, \mathbf{d}_A^i), \text{ and} \\ \gamma_B^\Delta &= \Gamma_B(\mathbf{c}_B^{i+1}, \mathbf{d}_B^{i+1}) - \Gamma_B(\mathbf{c}_B^i, \mathbf{d}_B^i).\end{aligned}\tag{3.16}$$

Despite the fixed generalized displacements  $\mathbf{d}$  at instant “ $i + 1$ ”, the convective coordinates  $\mathbf{c}$  of two consecutive timesteps are necessary. This characteristic enforces the history-dependency of the frictional forces. Figure 12 illustrates the contact trajectory vectors  $\gamma_A^\Delta$  and  $\gamma_B^\Delta$ .

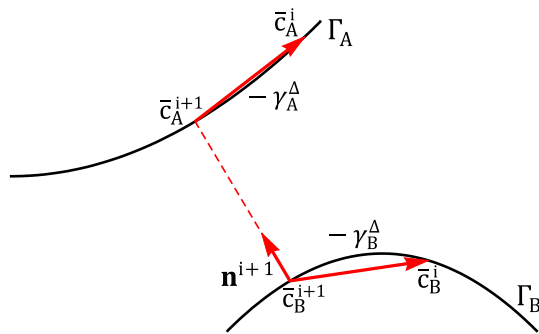


Figure 12: Representation of the frictional contact of two splines  $\Gamma_A^{i+1}$  and  $\Gamma_B^{i+1}$  at configuration “ $i + 1$ ”. The red arrows indicate the sliding paths  $\gamma_A^\Delta$  and  $\gamma_B^\Delta$ , and the normal direction  $\mathbf{n}^{i+1}$  [2].

It is possible now, considering two contact trajectory vectors  $\gamma_A^\Delta$  and  $\gamma_B^\Delta$ , to estimate a vector defined by the difference of both as  $\gamma_{AB}^\Delta = (-\gamma_A^\Delta + \gamma_B^\Delta)$ . This vector  $\gamma_{AB}^\Delta$  represents the difference between the trajectories of both contacting bodies’ material points, during a timestep. However, to evaluate the frictional behavior, only the tangential part of  $\gamma_{AB}^\Delta$  is necessary. It is possible to observe in Figure 12 that  $\gamma_A^\Delta$ ,  $\gamma_B^\Delta$ , and consequently  $\gamma_{AB}^\Delta$  are not based on the spline-based contact surface, but only in the spline-curve. This strategy represents a simplification, as long as frictional moments are neglected. The formulation, however, is still suitable for simulations involving slender beams (small radius). The tangential part of  $\gamma_{AB}^\Delta$ , which represents a measure for the incremental tangential gap  $\mathbf{g}_t^\Delta$ , is defined as

$$\mathbf{g}_t^\Delta = \gamma_{AB}^\Delta - (\gamma_{AB}^\Delta \cdot \mathbf{n}^{i+1})\mathbf{n}^{i+1} = (\mathbf{I} - \mathbf{n}^{i+1} \otimes \mathbf{n}^{i+1})\gamma_{AB}^\Delta \quad (3.17)$$

where  $\mathbf{n}^{i+1}$  is the contact normal vector at configuration “ $i+1$ ”. It is possible to compute the tangential gap  $\mathbf{g}_t^\Delta$  as

$$\mathbf{g}_t^\Delta = (\mathbf{I} - \mathbf{n}^{i+1} \otimes \mathbf{n}^{i+1}) ((\Gamma_A(c_A^i, \mathbf{d}_A^{i+1}) - \Gamma_B(c_B^i, \mathbf{d}_B^{i+1})) = (\mathbf{I} - \mathbf{n}^{i+1} \otimes \mathbf{n}^{i+1})\hat{\mathbf{g}}_n(\mathbf{c}^i, \mathbf{d}^{i+1}) \quad (3.18)$$

where  $\mathbf{c}^i$  is a vector containing the convective coordinates at configuration “ $i$ ” and  $\mathbf{d}^{i+1}$  is a vector containing the generalized displacements at configuration “ $i+1$ ”. Observe that (3.18) has no terms associated with  $\Gamma_A(c_A^{i+1}, \mathbf{d}_A^{i+1})$  and  $\Gamma_B(c_B^{i+1}, \mathbf{d}_B^{i+1})$ . These terms are actually zero since they are, by construction, parallel to  $\mathbf{n}^{i+1}$ . A more detailed discussion of (3.18) can be found in [6] and [27].

The tangential gap expressed in (3.18) represents the contribution of a single timestep to measure the relative sliding. However, to represent the whole contribution accumulated over time it is necessary to consider the contribution of all timesteps in a simulation. For that, it is convenient to define the total tangential gap  $\mathbf{g}_t^{i+1}$  as

$$\mathbf{g}_t^{i+1} = \mathbf{g}_t^\Delta + \mathbf{Q}^\Delta \mathbf{g}_t^i \quad (3.19)$$

where  $\mathbf{Q}^\Delta$  is a rotation tensor that guarantees that the previous accumulated tangential gap  $\mathbf{g}_t^i$  is always updated from direction  $\mathbf{n}^i$  to  $\mathbf{n}^{i+1}$ . As detailed in [27], it is possible to prove that  $\mathbf{n}^{i+1} = \mathbf{Q}^\Delta \mathbf{n}^i$  which implies that  $\mathbf{Q}^\Delta$  is just an operator mapping  $\mathbf{n}^i$  to  $\mathbf{n}^{i+1}$ . Among other possibilities, in this work, the Rodrigues rotation vector  $\mathbf{e}_\alpha$  is adopted to construct the rotation tensor  $\mathbf{Q}^\Delta$ . Therefore, the rotation tensor  $\mathbf{Q}^\Delta$  is expressed as

$$\mathbf{Q}^\Delta = \mathbf{I} + \frac{4}{4 + \alpha^2} \left( \mathbf{E}_\alpha + \frac{1}{2} \mathbf{E}_\alpha^2 \right) \quad (3.20)$$

where  $\alpha = 2 \tan(\theta^\Delta/2)$  with  $\theta^\Delta = \arcsin\|\mathbf{n}^i \times \mathbf{n}^{i+1}\|$ , and  $\mathbf{E}_\alpha = \text{skew}(\mathbf{e}_\alpha)$  with  $\mathbf{e}_\alpha = \alpha \mathbf{e}$  being  $\mathbf{e}$  the rotation direction.

### 3.3.1 Tangential Interaction Law

The frictional force is modeled by the Coulomb Law as presented in [56]. The proposed rheological model includes two sliding devices, an elastic part and a dissipative (viscous) part with static and dynamic friction coefficients that are considered to compute a trial friction force and test it against the Coulomb limit. Figure 13 illustrates the rheological model adopted including two sliding devices indicated with the numbers 1 and 2. This model is based on the formulations presented in [6] and [27].

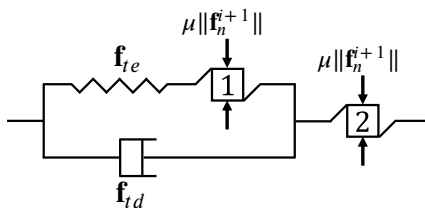


Figure 13: Rheological model for the frictional interaction including two sliding devices (1 and 2), an elastic contribution, and a dissipative contribution [2].

The elastic contribution to the frictional interaction  $\mathbf{f}_{te}$  is a linear function, defined with respect to the tangential gap presented in (3.19),

$$\mathbf{f}_{te} = \epsilon_{te} \mathbf{g}_t^{i+1} \quad (3.21)$$

where  $\epsilon_{te}$  is the so-called tangential penalty stiffness.

The viscous contribution to the friction force  $\mathbf{f}_{td}$  depends on the relative sliding velocity  $\dot{\mathbf{g}}_t$  at the interface, see [29],

$$\mathbf{f}_{td} = c_{td} \dot{\mathbf{g}}_t \quad (3.22)$$

where  $c_{td}$  is the tangential viscous damping coefficient.

With these two contributions, it is possible to define a frictional “trial” force  $\mathbf{f}_{trial}$  composed of an elastic part and a viscous part

$$\mathbf{f}_{trial} = \mathbf{f}_{te} + \mathbf{f}_{td}. \quad (3.23)$$

Note that, though both terms  $\mathbf{f}_{te}$  and  $\mathbf{f}_{td}$  occur in the instantaneous contact tangent

plane, they may not be parallel. Now it is convenient to introduce the frictional contact direction  $\mathbf{t}^{i+1}$  expressed as

$$\mathbf{t}^{i+1} = \frac{\mathbf{f}_{trial}}{\|\mathbf{f}_{trial}\|}. \quad (3.24)$$

It is still possible to check the “stick-slide” status of the Coulomb model (2) in Figure 13 by comparing the magnitude of the frictional trial force in (3.23) and the magnitude of the normal contact force in (3.15) multiplied by the friction coefficient  $\mu$ . Considering a friction coefficient  $\mu$ , taken as static or dynamic according to the previous time status (sliding/sticking), the status of the sliding device is called “stick” if  $\|\mathbf{f}_{trial}\| \leq \mu \|\mathbf{f}_n^{i+1}\|$  and “slide”, otherwise.

In a “stick” scenario, the current frictional force  $\mathbf{f}_t^{i+1}$  is equal to  $\mathbf{f}_{trial}$  as presented in (3.23). In this case, the frictional force  $\mathbf{f}_t^{i+1}$  is expressed as

$$\mathbf{f}_t^{i+1} = \mathbf{f}_{trial} = \mathbf{f}_{te} + \mathbf{f}_{td}. \quad (3.25)$$

However, for a “slide” scenario the frictional force  $\mathbf{f}_t^{i+1}$  is limited, according to the dynamic friction coefficient  $\mu_d$ . Therefore, the frictional force  $\mathbf{f}_t^{i+1}$  is taken as

$$\mathbf{f}_t^{i+1} = \mu_d \|\mathbf{f}_n^{i+1}\| \mathbf{t}^{i+1}. \quad (3.26)$$

It is still necessary to consider the contribution of the sliding device (1) in Figure 13. For that, a similar procedure to the one used for the Coulomb sliding is adopted. To check the “stick-slide” status of the rheological model a comparison is made between the magnitude of the frictional elastic contribution, see (3.21), and the magnitude of the normal contact force, see (3.15), multiplied by a friction coefficient  $\mu$ . Considering a friction coefficient  $\mu$ , taken as static or dynamic according to the previous status of Coulomb sliding, the status of the rheological sliding is “stick” if  $\|\mathbf{f}_{te}\| \leq \mu \|\mathbf{f}_n^{i+1}\|$  and “slide” otherwise.

In a rheological sliding “stick” scenario, no correction is necessary of the tangential gap definition presented in (3.19). However, in a rheological sliding “slide” scenario, a specific tangential sliding gap  $\mathbf{g}_{t \text{ slide}}$  is necessary, see [27]. This tangential sliding gap

$\mathbf{g}_t$  *slide* is defined as

$$\mathbf{g}_t \text{ slide} = \mathbf{g}_t^{i+1} - \frac{\mu_d \|\mathbf{f}_n^{i+1}\|}{\epsilon_{te}} \frac{\mathbf{f}_{te}}{\|\mathbf{f}_{te}\|}. \quad (3.27)$$

It is possible to include the tangential sliding gap contribution  $\mathbf{g}_t$  *slide* due to rheological sliding in an updated tangential gap  $\mathbf{g}_t^{i+1}$  *updated*. The updated tangential gap  $\mathbf{g}_t^{i+1}$  *updated* is then defined as

$$\mathbf{g}_t^{i+1} \text{ updated} = \mathbf{g}_t^{i+1} - \mathbf{g}_t \text{ slide} = \frac{\mu_d \|\mathbf{f}_n^{i+1}\|}{\epsilon_{te}} \frac{\mathbf{f}_{te}}{\|\mathbf{f}_{te}\|}. \quad (3.28)$$

Finally, the tangential force and the corresponding tangential gap can be summarized as

$$\begin{aligned} \mathbf{f}_t^{i+1} &= \begin{cases} \mathbf{f}_{te} + \mathbf{f}_{td} & \text{if "stick" in Coulomb sliding} \\ \mu_d \|\mathbf{f}_n^{i+1}\| \mathbf{t}^{i+1} & \text{if "slide" in Coulomb sliding} \end{cases} \\ \mathbf{g}_t^{i+1} &= \begin{cases} \mathbf{g}_t^\Delta + \mathbf{Q}^\Delta \mathbf{g}_t^i & \text{if "stick" in rheological sliding} \\ \frac{\mu_d \|\mathbf{f}_n^{i+1}\|}{\epsilon_{te}} \frac{\mathbf{f}_{te}}{\|\mathbf{f}_{te}\|} & \text{if "slide" in rheological sliding.} \end{cases} \end{aligned} \quad (3.29)$$

### 3.4 Contact Problem Degeneration

The LCP expresses a set of orthogonality conditions of a pair of geometrical entities considering their convective coordinates. When there is no distinction between the geometric entities involved, the LCP is named “master-master”. The LCP orthogonality conditions can be weakened, however, for any particular reason, by fixing *a priori* one or more convective coordinates. In this case, the orthogonality conditions are amended and the geometrical entities are unevenly treated. In this context, according to the selection of orthogonality conditions, the LCP can be modified, for instance, to a “curve-to-node” or a “node-to-node” contact problem. A degeneration is herein regarded as the process of weakening a master-master LCP by fixing one or more convective coordinates [25].

For the proposed spline-based contact formulation only two convective coordinates  $c_A$  and  $c_B$ , respectively associated with  $\Gamma_A$  and  $\Gamma_B$ , are involved in a master-master LCP.

As a result, a master-slave LCP degeneration corresponds to fixing one of the convective coordinates,  $c_A$  or  $c_B$ . Once a degeneration process is adopted, it is still necessary to choose a convective coordinate value. In this work, every time a degeneration takes place in  $\Gamma_A$  or  $\Gamma_B$  the corresponding convective coordinate is fixed for simplicity as the knot span mean value. The choice for this particular value seeks a fair contact forces distribution to the structural model according to the spline basis functions. Moreover, the superscript  $(\cdot)^*$  is adopted to indicate a fixed convective coordinate or a spline element where degeneration takes place. The process of fixing the convective coordinates can be expressed as

$$\begin{aligned}\bar{c}_A^* &= \frac{\xi_{A_i} + \xi_{A_{i+1}}}{2} \text{ with } \Gamma_A^*, \text{ and} \\ \bar{c}_B^* &= \frac{\xi_{B_i} + \xi_{B_{i+1}}}{2} \text{ with } \Gamma_B^*\end{aligned}\tag{3.30}$$

with  $[\xi_{A_i}, \xi_{A_{i+1}}[$  and  $[\xi_{B_i}, \xi_{B_{i+1}}[$  representing respectively the knot spans of  $\Gamma_A$  and  $\Gamma_B$ . Figure 14a and Figure 14b illustrate the master-slave LCP solutions when degeneration takes place respectively in  $\Gamma_A$  and  $\Gamma_B$ . The master-slave LCP solutions presented in Figure 14 were, in fact, obtained from the original master-master LCP solution presented in Figure 9b.

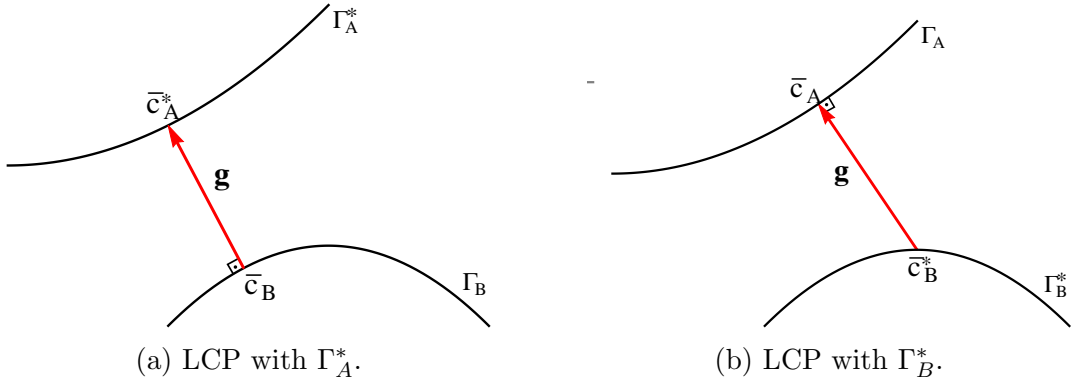


Figure 14: LCP degenerations [3].

One of the consequences of LCP degeneration is a reduction of the orthogonality relations. In this, a simple master-slave LCP is considered with a single orthogonality condition defined as

$$\begin{aligned}r_A &= \Gamma_{A,\xi_A} \cdot \mathbf{g} = 0 \text{ with } \Gamma_B^*, \text{ and} \\ r_B &= -\Gamma_{B,\xi_B} \cdot \mathbf{g} = 0 \text{ with } \Gamma_A^*.\end{aligned}\tag{3.31}$$

Moreover, the Hessian matrix  $\mathbf{H}$  is also simplified to a single value. When degeneration takes place in  $\Gamma_A$  or  $\Gamma_B$  the Hessian is no longer a matrix, but a scalar  $H$  given by

$$\begin{aligned} H_{AA} &= \mathbf{g} \cdot \Gamma_{A,\xi_A\xi_A} + \Gamma_{A,\xi_A} \cdot \Gamma_{A,\xi_A} \quad \text{with } \Gamma_B^*, \text{ and} \\ H_{BB} &= -\mathbf{g} \cdot \Gamma_{B,\xi_B\xi_B} + \Gamma_{B,\xi_B} \cdot \Gamma_{B,\xi_B} \quad \text{with } \Gamma_A^*. \end{aligned} \quad (3.32)$$

### 3.4.1 Contact Solution Characterization

A crucial aspect of the here proposed numerical strategy is the identification of non-convexity or non-strict-convexity of the LCP. For that, one may introduce the so-called LCP characterization, as a spectral analysis of the Hessian  $\mathbf{H}$  for a given LCP solution  $\bar{\mathbf{c}}$ . This will be seen as a reliable tool for the decision-making on the acceptance or rejection of an LCP solution  $\bar{\mathbf{c}}$ , such as, in case of rejection, how to proceed. The original LCP Hessian eigenvalues are denoted as  $\lambda_1$  and  $\lambda_2$ . For degenerated contact problems, however, a single eigenvalue  $\lambda_1$  is evaluated. The eigenvalue  $\lambda_1$  is, in fact, equal to the Hessian in this simplified case, as it is expressed by a single value  $H_{AA}$  or  $H_{BB}$ .

The here-discussed technique is not capable of identifying complex non-uniqueness scenarios, such as multiple pointwise solutions between wavy geometrical entities. Instead, it is devoted to identifying non-uniqueness cases stemming from conformal contact problems, to be useful in the particular beam-to-beam contact search, considering pairs of spline-based curves, as already here presented.

To illustrate the contact solution characterization, several contact scenarios are analyzed taking as basis two ill-defined geometric contact problems. In some cases, the LCP solution is not unique. These cases are presented here in 2D for convenience, but the formulation adopted and the conclusions drawn are directly extensible for 3D cases. The contact cases analyzed are presented in Figure 15a and Figure 15b respectively as a curved contact problem and a straight contact problem.



Figure 15: Cases with ill-defined LCP solution [3].



Consider now, for both contact cases, two spline elements  $\Gamma_A$  and  $\Gamma_B$  with equal basis functions defined as

$$\begin{aligned} N_{2,2}(\xi) &= \frac{1}{2}(2 - 3\xi)^2 \\ N_{3,2}(\xi) &= -\frac{3}{2} + 9\xi - 9\xi^2 \\ N_{4,2}(\xi) &= \frac{1}{2}(1 - 3\xi)^2 \end{aligned} \tag{3.33}$$

within a valid convective coordinate range of  $[1/3, 2/3[$ . These spline basis functions are illustrated in Figure 5b. Despite using the same basis functions,  $\Gamma_A$  and  $\Gamma_B$  represent different curves as defined by their control meshes in Table 2, similarly as presented in Figure 8. Moreover, in these studies only the  $y$  coordinates of the extreme nodes are perturbed. It is possible to observe in Table 2 that two new variables  $h_A$  and  $h_B$  were introduced, respectively, for  $\Gamma_A$  and  $\Gamma_B$ . This is done to easily modify the overall spline elements' shapes.

Control mesh for $\Gamma_A$	Control mesh for $\Gamma_B$
$\mathbf{P}_{A_2} = (0, 0.1 + h_A)$	$\mathbf{P}_{B_2} = (0, -0.1 - h_B)$
$\mathbf{P}_{A_3} = (1, 0.1)$	$\mathbf{P}_{B_3} = (1, -0.1)$
$\mathbf{P}_{A_4} = (2, 0.1 + h_A)$	$\mathbf{P}_{B_4} = (2, -0.1 - h_B)$

Table 2: Control meshes for  $\Gamma_A$  and  $\Gamma_B$  with new variables  $h_A$  and  $h_B$  [3].

Considering then the spline basis functions in (3.33) and the control meshes detailed in Table 2, it is possible to establish the spline elements  $\Gamma_A$  and  $\Gamma_B$  as

$$\begin{aligned} \Gamma_A(h_A) &= \sum_{i=2}^4 N_{i,2} P_{A_i} \\ \Gamma_B(h_B) &= \sum_{i=2}^4 N_{i,2} P_{B_i}. \end{aligned} \tag{3.34}$$

Figure 16 illustrates the spline elements  $\Gamma_A$  and  $\Gamma_B$  respectively in blue and green colors with their corresponding control meshes in gray adopting  $h_A = 1$  and  $h_B = 1$ . For the configuration presented in Figure 16, the LCP solution is trivial and equals  $\bar{\mathbf{c}}^T = [0.5, 0.5]^T$ . Moreover, Hessian eigenvalues analysis presented further are performed considering in principle a LCP solution equals  $\bar{\mathbf{c}}^T = [0.5, 0.5]^T$ . Non-trivial LCP solutions are discussed when necessary.

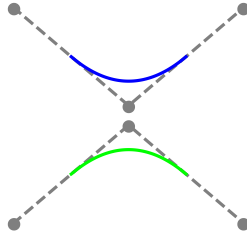


Figure 16: Spline elements  $\Gamma_A$  and  $\Gamma_B$  respectively in blue and green with their control meshes in gray for  $h_A = 1$  and  $h_B = 1$  [3].

### 3.4.1.1 Curved Contact Problem

The objective of this study is to illustrate the evaluation of the Hessian  $\mathbf{H}$  eigenvalues  $\lambda_1$  and  $\lambda_2$  behavior for a curved contact problem with possible non-unique LCP solutions. The study here developed is similar to the one presented in [29]. In [29], however, the authors are interested in a surface-to-surface contact problem involving thus four eigenvalues. The analysis here proposed starts from the trivial case illustrated in Figure 16, which has a unique solution, and proceeds step-by-step by modifying the overall shape of a single spline element. To perform this analysis a value of  $h_B = 1$  is fixed while several values of  $h_A$  are considered. Figure 17 depicts the eigenvalues evolution for several  $h_A$  values, depicting also for each case a simple visualization of the geometrical shapes involved in the LCP considered.

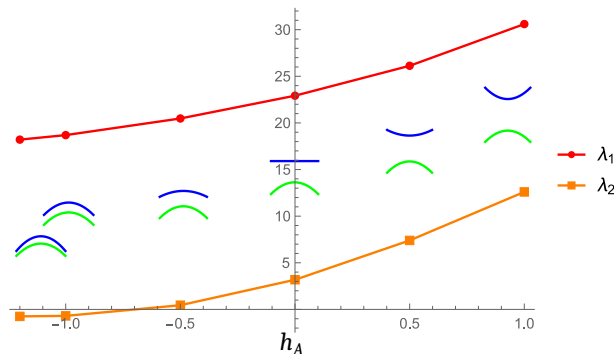


Figure 17: Hessian matrix eigenvalues evolution for a fixed  $h_B = 1$  and several  $h_A$  values for a curved conformal contact scenario [3].

It is possible to observe that both eigenvalues  $\lambda_1$  and  $\lambda_2$  decrease as  $\Gamma_A$  approaches a scenario with non-unique LCP solution. The cases with  $h_A = 1$ ,  $h_A = 0.5$ ,  $h_A = 0$ , and  $h_A = -0.5$  present both positive Hessian eigenvalues that are associated with straightforward LCP solutions. Moreover, it is noteworthy that the lower eigenvalue  $\lambda_2$  is negative when  $h_A = -1$  and  $h_A = -1.2$ .

When  $h_A = -1$  both curves present exactly the same shape, as the control points are simply shifted. These curves, however, do not represent a curved conformal contact

scenario. See [36] for a discussion regarding contact problems involving conformal curves. The conformal contact involving splines is, however, quite uncommon as producing offset curved splines is a non-trivial task [57, 58]. For this particular configuration, the LCP is characterized as a saddle with three LCP solutions, similarly as observed in [29]. The first LCP solution considered is  $\bar{\mathbf{c}}^T = [0.5, 0.5]^T$ . This solution does not represent the closest point projection, instead, it is a saddle point. The two other symmetric solutions (not illustrated) are intersections that occur in the extensions of the spline elements which are away from the knot spans range of interest. Therefore only  $\bar{\mathbf{c}}^T = [0.5, 0.5]^T$  is considered a valid LCP solution for the analysis.

When  $h_A = -1.2$  the LCP also presents three solutions  $\bar{\mathbf{c}}_1 = [0.788675, 0.788675]$ ,  $\bar{\mathbf{c}}_2 = [0.5, 0.5]$ , and  $\bar{\mathbf{c}}_3 = [0.211325, 0.211325]$ . However, as observed in the previous analysis, only  $\bar{\mathbf{c}}_2$  is considered a valid feasible solution, since  $\bar{\mathbf{c}}_1$  and  $\bar{\mathbf{c}}_3$  are not in the valid knot span of  $[1/3, 2/3[$ . In fact, a configuration with spline intersections is not of practical interest, as it would denote an extreme penetration scenario, as the spline curves represent beam centerlines, and the contact mechanical action occurs on the beam surfaces, considering proper cross-sections dimensions as defined in the gap expression (3.8). An intersection LCP solution near valid knot spans can be interpreted as a scenario of a possible proper contact interaction handled by neighbor spline elements due to the  $C^1$  continuity (see [29]).

#### 3.4.1.2 Straight Contact Problem

In this section, the aim is to evaluate the Hessian  $\mathbf{H}$  eigenvalues  $\lambda_1$  and  $\lambda_2$  evolution for a straight conformal contact scenario. To perform this study a value  $h_B = 0$ , that is equivalent to a straight line, is fixed while several  $h_A$  values are tested. A value of  $h_A = 1$  is initially adopted. The Hessian eigenvalues  $\lambda_1$  and  $\lambda_2$  evolution according to the  $h_A$  values are presented in Figure 18.

The results in Figure18 show that the eigenvalues decrease as  $\Gamma_A$  approaches scenarios with non-unique LCP solutions. This figure shows that both Hessian eigenvalues are positive  $h_B = 1$  and  $h_B = 0.5$ . These cases correspond to trivial unique LCP solutions. Moreover, it is possible to note in Figure 18 that the lower eigenvalue  $\lambda_2$  is zero when  $h_A = 0$  and negative when  $h_A = -0.5$ .

When  $h_A = 0$  a perfect straight conformal contact scenario is defined. In this scenario, there are infinite LCP solutions. Despite that, for any valid LCP solution, the Hessian eigenvalues are constant with a zero  $\lambda_2$ .

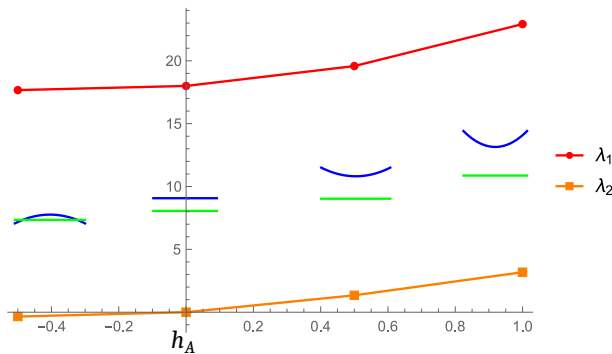


Figure 18: Hessian matrix eigenvalues evolution for a fixed  $h_B = 0$  and several  $h_A$  values for a straight conformal contact scenario.

When  $h_A = -0.5$  the LCP presents three valid (within the knot-span) solutions (each one with corresponding pairs of Hessian eigenvalues). The LCP solutions and eigenvalues of  $\mathbf{H}$  when  $h_A = -0.5$  are presented in Table 3. Though valid concerning spline elements knot spans, the LCP solutions  $\bar{\mathbf{c}}_1$  and  $\bar{\mathbf{c}}_3$  correspond to a very unlikely contact scenario of very large penetration, as such LCP solutions  $\bar{\mathbf{c}}_1$  and  $\bar{\mathbf{c}}_3$  correspond to intersections of the spline elements. This particular scenario results in a null gap vector, see (3.8). In practical problems, these spline intersections would represent an unfeasible contact scenario with extreme penetrations, as long as our gap measurement considers radial offsets together with the distance between beam centerlines. Finally, the last LCP solution  $\bar{\mathbf{c}}_2$  is indeed a saddle point with negative  $\lambda_2$ .

$\bar{\mathbf{c}}_1 = [0.629099, 0.629099]$	$\lambda_1 = 18.7003$
	$\lambda_2 = 0.649723$
$\bar{\mathbf{c}}_2 = [0.5, 0.5]$	$\lambda_1 = 17.6688$
	$\lambda_2 = -0.343826$
$\bar{\mathbf{c}}_3 = [0.370901, 0.370901]$	$\lambda_1 = 18.7003$
	$\lambda_2 = 0.649723$

Table 3: LCP solutions with their corresponding eigenvalues of  $\mathbf{H}$  when  $h_A = -0.5$ .

### 3.5 Numerical Strategy & Algorithm

The previous section shows that, in practice, one is interested in finding the LCP solution corresponding to a minimum distance problem, and neither an intersection (which is also mathematically characterized as a minimum) nor a saddle solution. Therefore, the scenario of interest is characterized by positive eigenvalues of the Hessian of the LCP, for the found solution.

To avoid problematic cases of spline intersections, that represent extreme penetrations,

the gap vector direction is monitored in contact interactions. This monitoring consists of calculating the dot product of the gap direction in two subsequent configurations. If the result is positive, the contact interaction is accepted. Otherwise, the contact is rejected and the simulation is cut back in time. Moreover, for a given found LCP solution, a non-positive eigenvalue  $\lambda_2$  is obtained we propose the degeneration of the LCP, in order to modify and recover a solution of interest. A small tolerance  $\text{tol}_c$  should be introduced to handle near straight conformal contact scenarios with approximately zero Hessian eigenvalue  $\lambda_2$ .

The proposed numerical strategy consists of evaluating, simultaneously, three numerical criteria of an LCP solution  $\bar{\mathbf{c}}$  to decide if it should be accepted, rejected, or undergoes a degeneration process. The three numerical criteria evaluated are:

1. The availability (convergence) of an LCP solution;
2. The location of a determined LCP solution, with respect to the valid range of the convective coordinates;
3. The contact problem characterization.

The objective of the first numerical criterion is to handle contact problems for which a LCP solution diverges. In the proposed formulation the LCP is always expressed as a minimum distance problem of  $C^1$  smooth curves representing beam centerlines. Moreover, a robust trust-region (TR) optimization framework [53, 54] is adopted to calculate LCP solutions. However, when for some numerical reason the LCP solution diverges, a degeneration procedure is considered. The LCP solution divergence may be caused, for example, when a Hessian eigenvalue is zero, as in the scenario of perfect conformal contact.

The second criterion consists of a simple verification concerning the valid convective range of spline elements prone to contact. When searching for an LCP solution  $\bar{\mathbf{c}}$ , the convective coordinates are not restricted to valid knot spans. Therefore, an LCP solution  $\bar{\mathbf{c}}$  result may result in one or more non-feasible convective coordinates. In this case, the solution is rejected and degeneration is again considered. The second criterion can be expressed as

$$\begin{aligned} \xi_{A_i}(1 - \text{tol}_\xi) &\leq \bar{c}_A < \xi_{A_{i+1}}(1 + \text{tol}_\xi), \text{ and} \\ \xi_{B_i}(1 - \text{tol}_\xi) &\leq \bar{c}_B < \xi_{B_{i+1}}(1 + \text{tol}_\xi). \end{aligned} \tag{3.35}$$

where a small toleration parameter  $\text{tol}_\xi$  is introduced. The objective of the tolerance  $\text{tol}_\xi$  is to handle particular conformal contact scenarios involving large deformations between spline elements.

The third criterion is based on the contact solution  $\bar{\mathbf{c}}$  characterization concerning the LCP solution (see Section 3.4.1). The objective of this criterion is to identify cases in which the solution  $\bar{\mathbf{c}}$  is, in fact, a minimum. A similar procedure is presented in [29] to characterize the contact of surfaces, in that context to modify the strategy while solving a contact problem.

The previous subsections explored numerical criteria to identify and characterize cases for which a LCP degeneration should be considered. However, it is still necessary to establish an algorithm to properly define the contact problem workflow. Figure 19 illustrates the LCP solution numerical workflow.

The numerical workflow starts with a LCP between two spline elements that are prone to contact. After that, all three criteria are evaluated for the decision-making process with respect to a LCP solution  $\bar{\mathbf{c}}$ . If all requirements are simultaneously met then the LCP solution  $\bar{\mathbf{c}}$  is accepted and the workflow ends.

Otherwise, if at least one criterion fails, the LCP undergoes a degeneration process with  $\Gamma_A^*$ . There is no particular criterion to define which spline element is  $\Gamma_A$  or  $\Gamma_B$ , this choice is arbitrary. Alternatively, one may adopt a criterion that evaluates both  $\Gamma_A^*$  and  $\Gamma_B^*$  and adopts the one with a lower gap value. Moreover, when degeneration occurs, the LCP is reduced to a single convective coordinate that, in this case, with  $\Gamma_A^*$ , is  $\bar{c}_B$ . The LCP solution  $\bar{c}_B$  is then verified with three criteria. These criteria are equivalent to the ones initially adopted for  $\bar{\mathbf{c}}$ . If all criteria for  $\bar{c}_B$  are met, the LCP solution is accepted and the process ends.

If at least one criterion is not met, another degeneration process takes place, now considering  $\Gamma_B^*$ . The LCP is therefore reduced to a single variable  $\bar{c}_A$ . Again all three criteria are verified. If all criteria are met the LCP solution is accepted and the process ends. Otherwise, the LCP solution is rejected and the process ends.

When degenerating the LCP, it is always assumed that in one of the curves, the solution is known and given as in (3.30), as a simple choice that seems valid for sufficiently refined meshes. The refinement will introduce the representation of a distributed contact action as a set of pointwise contact actions, according to the degeneration introduced. The choice of fixing convective coordinates in the middle of spline elements also seeks a better distribution of pointwise contact interactions.

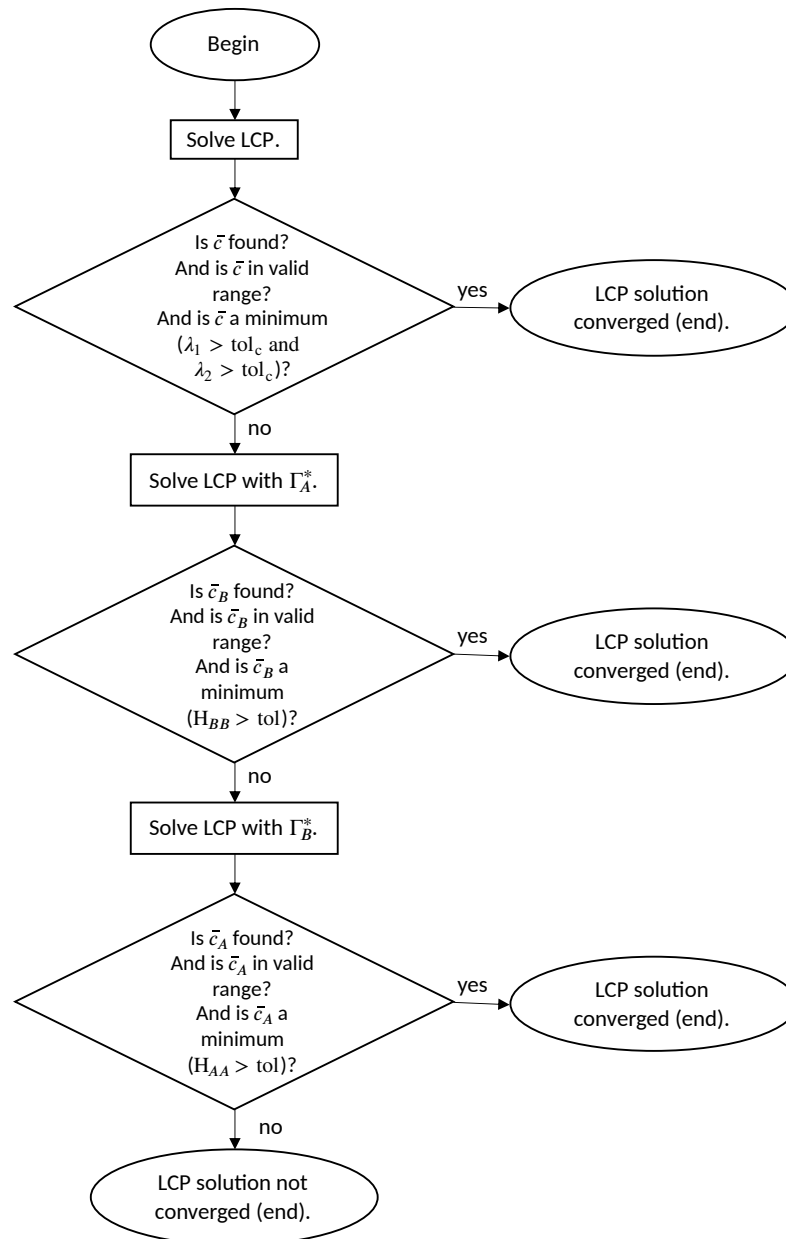


Figure 19: LCP solution workflow [3].

## 4 STRUCTURAL THEORY

This chapter presents a brief overview of the structural theory adopted with the spline-based contact formulation. Moreover, the Giraffe finite element solver is briefly introduced and the implementations associated with the contact formulation are described. The geometrically-exact beam theory adopted is detailed in [59, 60, 61].

Finally, an originally developed software for the modeling of textiles in the Giraffe solver is presented [1].

### 4.1 Kinematics

The proposed contact formulation is directly attachable to any quadratic beam formulation. In this work a nonlinear geometrically-exact structural formulation is adopted. The foundations for the geometrically-exact formulations were first presented in the seminal works of Simo[62, 63, 64]. The objective of this subsection is not to present in detail the geometrically-exact beam formulation, which can be found in [65, 66, 67]. However, for a better understanding of the model kinematics, the displacement field, and the constitutive matrix are presented next. The position of a generic point  $\mathbf{x}$  of a beam element is defined as

$$\mathbf{x} = \zeta \mathbf{e}_3^r + \mathbf{u} + \mathbf{Q} \mathbf{a}^r, \quad (4.1)$$

where  $\zeta$  is a convective coordinate that lies in the beam axis,  $\mathbf{e}_3^r$  is an axis oriented along the beam axis straight in the reference configuration,  $\mathbf{u}$  is the beam axis displacement,  $\mathbf{Q}$  is a rotation tensor for a given cross-section that maps the reference configuration to the current configuration, and  $\mathbf{a}^r$  is a vector that reads all points of the cross-section in the reference configuration. This kinematics represents a Timoshenko beam model. Figure 20



illustrates the displacement field presented in (4.1). The generic point position presented in (4.1) is, for now, completely arbitrary, and therefore can experience large displacements and finite rotations.

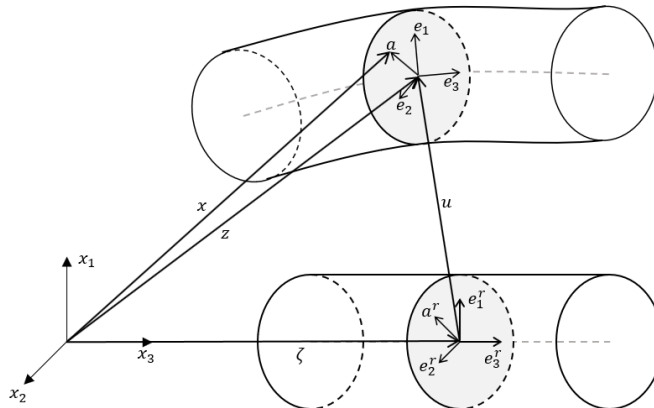


Figure 20: Representation of the displacement field of a generic point  $\boldsymbol{x}$  according to the geometrically-exact beam theory adopted [1].

A possible option to write the rotation tensor presented in (4.1) is using Rodrigues parameters, as presented in (3.20). It is important to note that the kinematic treatment presented in (4.1) is geometrically-exact, in other words, is not limited to small displacements and rotations (see [63, 64, 65]). This is the kinematic assumption employed for all simulations and examples shown in this work.

## 4.2 Constitutive Matrix

Next, infinitesimal strains are considered with the exclusive objective of illustrating the derivation of the constitutive matrix behavior for related generalized stress/strain. In this context, assuming that only small rotations occur, it is possible to consider the Rodrigues rotation tensor as  $\boldsymbol{Q} \approx \boldsymbol{I} + \boldsymbol{A}$ , where  $\boldsymbol{A}$  is a skew-symmetric tensor defined by

$$\boldsymbol{A} = \begin{bmatrix} 0 & -\alpha_3 & \alpha_2 \\ \alpha_3 & 0 & -\alpha_1 \\ -\alpha_2 & \alpha_1 & 0 \end{bmatrix}, \quad (4.2)$$

where  $\alpha_1$ ,  $\alpha_2$ , and  $\alpha_3$  are rotations concerning respectively  $\boldsymbol{e}_1$ ,  $\boldsymbol{e}_2$  and  $\boldsymbol{e}_3$ . The position of a generic point  $\boldsymbol{x}$  can be rewritten considering small rotations and the cross-section position ( $\boldsymbol{a}^r = x_1 \boldsymbol{e}_1^r + x_2 \boldsymbol{e}_2^r$ ) as

$$\mathbf{x} = \zeta \mathbf{e}_3^r + \mathbf{u} + (\mathbf{I} + \mathbf{A})(x_1 \mathbf{e}_1^r + x_2 \mathbf{e}_2^r). \quad (4.3)$$

Considering the displacement of a material point  $\mathbf{x}$ , it is possible now to calculate the deformation gradient as  $\mathbf{F}$  by

$$\mathbf{F} = \mathbf{x}_{,1} \otimes \mathbf{e}_1^r + \mathbf{x}_{,2} \otimes \mathbf{e}_2^r + \mathbf{x}' \otimes \mathbf{e}_3^r \quad (4.4)$$

where  $(\cdot)_{,1}$ ,  $(\cdot)_{,2}$ , and  $(\cdot)'$  denote, respectively, partial derivatives with respect to  $x_1$ ,  $x_2$ , and  $x_3$ . As a result, the deformation gradient  $\mathbf{F}$  yields

$$\mathbf{F} = \mathbf{I} + \mathbf{A} \mathbf{e}_1^r \otimes \mathbf{e}_1^r + \mathbf{A} \mathbf{e}_2^r \otimes \mathbf{e}_2^r + (u' + A' a^r) \otimes \mathbf{e}_3^r. \quad (4.5)$$

From the deformation gradient  $\mathbf{F}$ , it is possible to obtain a strain measure  $\nabla \mathbf{S}$  as

$$\nabla \mathbf{S} = \mathbf{F} - \mathbf{I}. \quad (4.6)$$

The strain measure  $\nabla \mathbf{S}$  of  $\mathbf{F}$  then leads to  $\nabla \mathbf{S} = \mathbf{A} \mathbf{e}_1^r \otimes \mathbf{e}_1^r + \mathbf{A} \mathbf{e}_2^r \otimes \mathbf{e}_2^r + (u' + A' a^r) \otimes \mathbf{e}_3^r$  or, in a matrix form, to

$$\nabla \mathbf{S} = \begin{bmatrix} 0 & -\alpha_3 & u'_1 - \alpha'_3 x_2 \\ \alpha_3 & 0 & u'_2 + \alpha'_3 x_1 \\ -\alpha_2 & \alpha_1 & u'_3 + \alpha'_1 x_2 - \alpha'_2 x_1 \end{bmatrix}. \quad (4.7)$$

Assuming now that only small strains take place again only to derive the constitutive matrix, it is reasonable to calculate the infinitesimal strain tensor  $\mathbf{E}$  defined by

$$\mathbf{E} = \frac{1}{2} (\nabla \mathbf{S} + \nabla \mathbf{S}^T). \quad (4.8)$$

The Green-Lagrange strain tensor  $\mathbf{E}$  yields

$$\mathbf{E} = \begin{bmatrix} 0 & 0 & \frac{1}{2}(u'_1 - \alpha'_3 x_2 - \alpha_2) \\ & 0 & \frac{1}{2}(u'_2 + \alpha'_3 x_1 + \alpha_1) \\ Sym. & & u'_3 + \alpha'_1 x_2 - \alpha'_2 x_1 \end{bmatrix}. \quad (4.9)$$

It is suitable to introduce two generalized strain vectors of great relevance to beam kinematics. The former vector called  $\boldsymbol{\eta}$  is associated with generalized beam axial strains and is defined as

$$\boldsymbol{\eta} = \mathbf{u}' - \boldsymbol{\alpha} \times \mathbf{e}_3^r = \begin{bmatrix} u'_1 - \alpha_2 \\ u'_2 + \alpha_1 \\ u'_3 \end{bmatrix}. \quad (4.10)$$

The latter vector called  $\boldsymbol{\kappa}$  is the specific rotation, defined as

$$\boldsymbol{\kappa} = \begin{bmatrix} \alpha'_1 \\ \alpha'_2 \\ \alpha'_3 \end{bmatrix}. \quad (4.11)$$

The Green-Lagrange strain tensor  $\mathbf{E}$  can be rewritten considering the generalized strain vectors  $\boldsymbol{\eta}$  and  $\boldsymbol{\kappa}$ , and a convenient Voigt notation as

$$\boldsymbol{\gamma} = \begin{bmatrix} \gamma_{13} \\ \gamma_{23} \\ \gamma_{33} \end{bmatrix} = \begin{bmatrix} \eta_1 - \kappa_3 x_2 \\ \eta_2 + \kappa_3 x_1 \\ \eta_3 + \kappa_1 x_2 - \kappa_2 x_1 \end{bmatrix}. \quad (4.12)$$

Additionally, considering the generalized Hooke's law, the beam model stress-strain relation can be expressed as

$$\boldsymbol{\tau} = \begin{bmatrix} G\gamma_{13} \\ G\gamma_{23} \\ E\epsilon_{33} \end{bmatrix} \quad (4.13)$$

where  $E$  and  $G$  are, respectively the Young's Modulus and the Shear Modulus. The group

of equations in (4.13) represent the stress components acting in any material point. Therefore, the total equivalent forces and moments in each direction can be simply obtained by integration as

$$\begin{aligned} \mathbf{n} &= \int_A \tau_{13} dA \mathbf{e}_1^r + \int_A \tau_{23} dA \mathbf{e}_2^r + \int_A \tau_{33} dA \mathbf{e}_3^r \text{ and} \\ \mathbf{m} &= \int_A x_2 \tau_{33} dA \mathbf{e}_1^r - \int_A x_1 \tau_{33} dA \mathbf{e}_2^r + \int_A (x_1 \tau_{23} - x_2 \tau_{13}) dA \mathbf{e}_3^r . \end{aligned} \quad (4.14)$$

The development of equations in (4.14) yields

$$\begin{aligned} n_1 &= \int_A \tau_{13} dA = kGA\eta_1 - GS_1\kappa_3, \\ n_2 &= \int_A \tau_{23} dA = kGA\eta_2 - GS_2\kappa_3, \\ n_3 &= \int_A \tau_{33} dA = EA\eta_3 + ES_1\kappa_1 + ES_2\kappa_2, \\ m_1 &= \int_A x_2 \tau_{33} dA = ES_1\eta_3 + EI_1\kappa_1 + EI_{12}\kappa_2, \\ m_2 &= - \int_A x_1 \tau_{33} dA = ES_2\eta_3 + EI_{12}\kappa_1 + EI_2\kappa_2, \text{ and} \\ m_3 &= \int_A x_1 \tau_{23} - x_2 \tau_{13} dA = -GS_1\eta_1 - GS_2\eta_2 + GI_0\kappa_3 , \end{aligned} \quad (4.15)$$

where  $k$  is the shear correction factor and the concepts of first moments of area ( $S_1$  and  $S_2$ ), second moments of area ( $I_1$  and  $I_2$ ), product of inertia ( $I_{12}$ ), and the polar moment of inertia ( $I_0$ ) were introduced. The first moments of area  $S_1$  and  $S_2$ , the second moments of area  $I_1$  and  $I_2$ , the product of inertia  $I_{12}$ , and the polar moment of inertia  $I_0$  are defined, in this context, as

$$\begin{aligned}
S_1 &= \int_A x_2 dA, \\
S_2 &= - \int_A x_1 dA, \\
I_1 &= \int_A x_2^2 dA, \\
I_2 &= \int_A x_1^2 dA, \\
I_{12} &= - \int_A x_1 x_2 dA, \text{ and} \\
I_0 &= \int_A (x_1^2 + x_2^2) dA .
\end{aligned} \tag{4.16}$$

Finally, it is possible to rearrange the terms in (4.15) to explicitly group generalized forces and moments, generalized strains, and the constitutive matrix as

$$\begin{bmatrix} n_1 \\ n_2 \\ n_3 \\ m_1 \\ m_2 \\ m_3 \end{bmatrix} = \begin{bmatrix} GA & 0 & 0 & 0 & 0 & -GS_1 \\ & GA & 0 & 0 & 0 & -GS_2 \\ & & EA & ES_1 & ES_2 & 0 \\ & & & EI_1 & EI_{12} & 0 \\ & & & & EI_2 & 0 \\ Sym. & & & & & GI_0 \end{bmatrix} \begin{bmatrix} \eta_1 \\ \eta_2 \\ \eta_3 \\ \kappa_1 \\ \kappa_2 \\ \kappa_3 \end{bmatrix}, \tag{4.17}$$

or in a more compact way as

$$\boldsymbol{\sigma} = \mathbf{D}\boldsymbol{\varepsilon} . \tag{4.18}$$

It is seen in equation (4.17) that a polar moment of inertia  $I_0$  appears, where a torsional inertia  $I_t$  would be expected. In fact, the polar moment of inertia  $I_0$  results from the initial hypothesis of null warping [68, 66]. A detailed formulation including arbitrary beam axis and warping in beam kinematics are presented in [68, 66].

When connecting the here shown constitutive equation evaluation with the desired large displacement and finite rotation kinematics, one has to employ the generalized strains presented in (4.17) always back-rotated to the reference configuration to avoid objectivity issues associated with finite rotations. This mapping transformation is, in fact, necessary since infinitesimal strains are assumed for the constitutive matrix while

finite displacements and rotations are considered for the geometrically-exact theory.

### 4.3 Weak Form

To establish the equilibrium equations for the model, a convenient possibility is to employ the weak form. The contributions of the internal forces, external loads, inertial forces, and contact (normal and frictional) forces are included. Each contribution is briefly presented as follows. From now on the  $\delta(\cdot)$  symbol is adopted for variation of quantities, also known as test functions.

By introducing some convenient notations and after some mathematical manipulation, it is possible to calculate from the displacement field presented in (4.1) a vector containing generalized forces and moments  $\boldsymbol{\sigma}$  written with respect to the reference configuration and a vector containing the generalized axial strains and specific rotations  $\boldsymbol{\varepsilon}$  back-rotated [69, 66]. With that, the internal forces contribution of all elements to the weak form  $\delta W_i$  is defined as

$$\delta W_i = \sum_{elements} \int_0^l \boldsymbol{\sigma} \cdot \delta \boldsymbol{\varepsilon} d\zeta, \quad (4.19)$$

where  $l$  is the length of the beam element in the reference configuration (see Figure 20). Considering a vector  $\bar{\mathbf{q}}$  containing the external generalized loads per reference length unit and a vector  $\delta \mathbf{d}$  containing the virtual displacement/rotation associated with a beam cross-section, the contribution of the external loads to the weak form  $\delta W_e$  is defined as

$$\delta W_e = \sum_{elements} \int_0^l \bar{\mathbf{q}} \cdot \delta \mathbf{d} d\zeta. \quad (4.20)$$

To account for the contribution of the inertial forces, it is necessary to introduce a vector  $\mathbf{f}$  containing the inertial forces and moments (see [59, 66] for details). Therefore, the inertial forces contribution  $\delta T$  of all elements is defined as

$$\delta T = \sum_{elements} \int_0^l \mathbf{f} \cdot \delta \mathbf{d} d\zeta. \quad (4.21)$$

The normal contact contribution to the weak form  $\delta W_n$  is simply defined by the normal force in (3.15) and the virtual normal gap vector in (3.8) for all contact pairs as

$$\delta W_n = \sum_{\text{contacts}} (\mathbf{f}_n \cdot \delta \mathbf{g}). \quad (4.22)$$

A normal contact contribution to the weak form and its corresponding tangential stiffness matrix, assuming a simplified interface law, are explicitly presented in Appendix 7.1. The frictional contact contribution to the weak form  $\delta W_t$  considering again all contact pairs is defined by the frictional force and the virtual tangential gap vector, see (3.29), as

$$\delta W_t = \sum_{\text{contacts}} (\mathbf{f}_t^{i+1} \cdot \delta \mathbf{g}_t^{i+1}). \quad (4.23)$$

It is important to observe that the contact is ultimately defined based on the spline geometry, though their contributions are incorporated in their corresponding nodes degrees-of-freedom. Finally, all contributions to the weak form yield

$$\delta W_i - \delta W_e + \delta T + \delta W_n + \delta W_t = 0. \quad (4.24)$$

## 4.4 Giraffe Finite Element Solver

For the numerical examples in this work, the Giraffe finite element solver is used [4]. The Giraffe solver already includes geometrically-exact beam and shell formulations [70, 71], master-master contact formulations of surfaces, and their degenerations [5, 6, 52, 27]. The Giraffe solver has been successfully used in challenging applications such as wind turbine blades [68], buckling of pipelines [72, 73], offshore risers [74, 59, 75, 60], and textiles [1].

### 4.4.1 Spline-Based Contact Implementation

The objective of this section is not to present in detail the spline-based contact formulation, but to provide an overview of the classes considered for implementation.

The proposed spline-based contact formulation is implemented in the Giraffe finite

element solver. To implement the spline-based contact formulation several classes were added in the original C++ object-oriented Giraffe code. These new classes were based on similar classes for the sake of conciseness and organization. The spline-based contact formulation is fully defined in the following classes.

- `Spline`
- `SplineElement`
- `SplineElementPair`
- `SplineElement.SplineElement`
- `SPContactData`
- `SPSP`

The `Spline` class contains all the necessary information to geometrically characterize the spline in space. The main data in this class are the nodes (control points), the knot vector, and the radius. The `SplineElement` class contains specific information about a spline element as a contact element. Therefore, a spline element contains basically three nodes, a radius, and nodal degrees-of-freedom information.

The `SplineElementPair` contains information on a pair of spline elements in which contact is prone to occur. This class effectively performs the search for an LCP solution. Moreover, this class characterizes found LCP solutions (see Section 3.4.1). The `SplineElement.SplineElement` class performs the normal and tangential contact contributions to the weak form. It is important to mention that the specific codes for these contributions were generated with the aid of the Mathematica<sup>®</sup> AceGen plug-in [76].

The `SPContactData` class contains all information regarding a pair of spline elements prone to contact. Some important information in this class are the normal gap vector, the tangential gap vector, and the LCP solution convective coordinates. Finally, the `SPSP` class contains information regarding the normal and tangential interface laws adopted, the allocation of memory, the rough pinball search, and the memory allocation.

#### 4.4.2 Textile Modeling

The Giraffe finite element solver is a powerful tool for various applications. For the textile modeling, however, an original software was developed in C# to combine the Giraffe solver with a specialized software for textiles, the TexGen<sup>®</sup> [77].



The TexGen<sup>®</sup> software is an open-source well-established option for the geometric modeling of textiles that has been used in several mechanical studies. The TexGen<sup>®</sup> also includes a key feature that permits recording and running Python scripts. This feature was used as an interface to exchange information with TexGen<sup>®</sup>.

Textile modeling is defined in three steps. In the first step, the developed software creates a Python script containing general geometric parameters such as the number of yarns in each direction  $y_n$ , the in-plane yarn spacing  $y_s$ , the out-of-plane yarn spacing or gap  $y_g$ , the yarn horizontal length  $y_l$ , and some interpolating points for the yarns centroidal axis. Figure 22 illustrates these parameters.

Figure 21 shows the developed software interface.

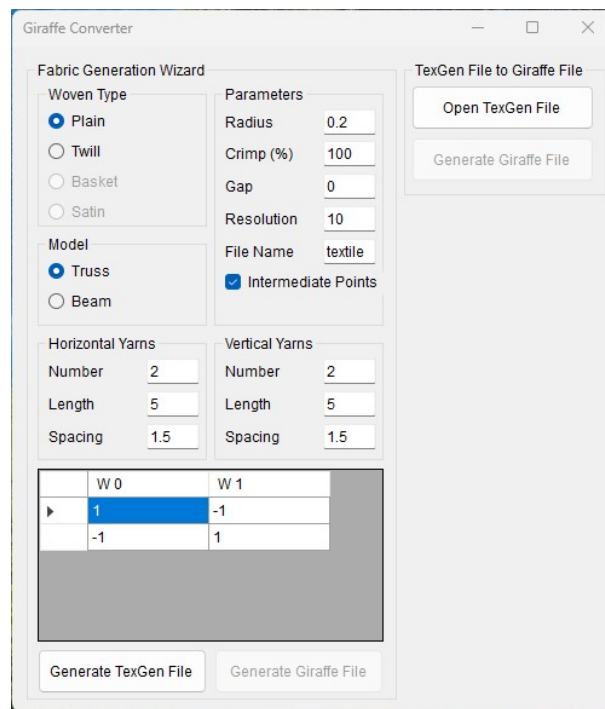


Figure 21: Original developed software for integrating the Giraffe solver with the TexGen<sup>®</sup> software.

Additionally, an indirect relative crimp measure parameter  $y_c$  is introduced. This relative crimp, which is a percentual value, indicates how yarns in both directions are relatively placed from the textile plane keeping the gap between them. In this context, a crimp of  $y_c = 100\%$  means that yarns in both directions are equally distant from the textile plane while a crimp of  $y_c = 0\%$  means that yarns in the “ $x$ ” direction are exactly at the textile plane as seen in Figure 23.

In the second step, the TexGen<sup>®</sup> software imports the Python script file and generates a model file containing detailed information on each yarn centroidal axis. Finally, in the

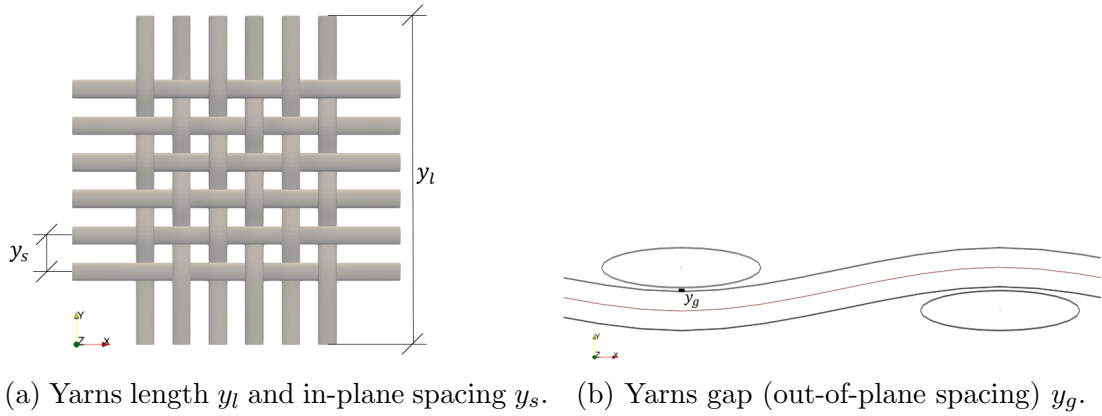


Figure 22: Textile geometric parameters [1].

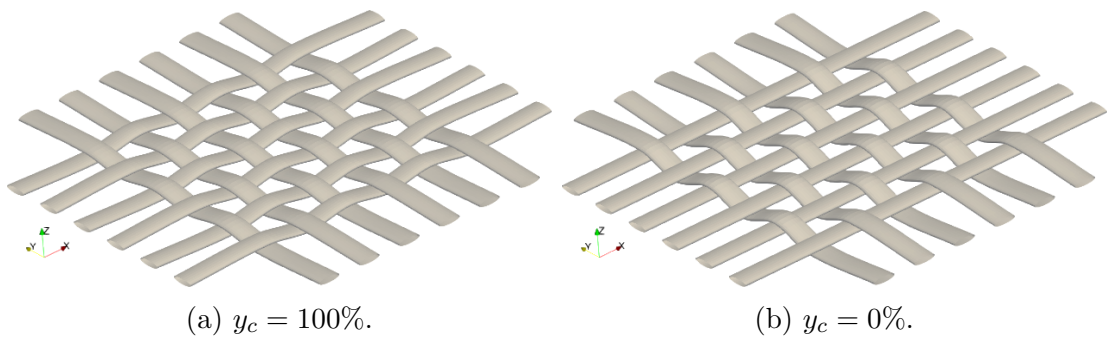


Figure 23: Yarns relative crimp [1].

third step, the developed software imports back the TexGen<sup>®</sup> model file and generate a specific input file for the simulation in the Giraffe solver. Figure 24 illustrates the modeling strategy. This final geometry is an approximation based on beam straight elements of Bézier curves such as in TexGen<sup>®</sup>.

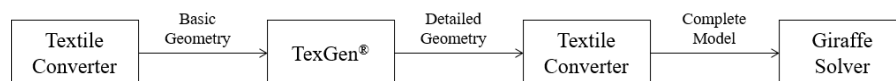


Figure 24: Textile modeling strategy [1].

## 5 NUMERICAL EXAMPLES

This chapter presents several applications of the spline-based contact problem in challenging problems involving conformal and non-conformal scenarios [2, 3].

### 5.1 Non-conformal Contact

The examples in this section are, whenever possible, compared with a non-smooth surface-to-surface contact formulation developed in [5, 6]. For the sake of convenience, in this section, surface-to-surface contact formulation results are indicated with “SS” while spline-based contact formulation results are indicated as “SP”.

#### 5.1.1 Perpendicular Beams

In this example, three quasi-static simulations are performed using both, “SS” and “SP”, contact models. The example consists of the modeling of two cantilever beams that are perpendicular to each other. A displacement is prescribed at the tip of one beam, to introduce contact occurrence. The adopted time scale is used only to impose the displacements gradually. In all simulations of this example, each beam is  $3m$  long with a radius of  $0.06m$  and is composed of 15 elements. Moreover, a material with an Young’s Modulus of  $2E9N/m^2$  and a Poisson ratio of 0.3 is considered. In these simulations Point A and Point B are respectively located at  $(2.5, 0, 0.3)m$  and  $(0, 2.5, 0)m$ .

##### 5.1.1.1 Normal Contact

The first analysis considers only normal contact with a linear interface law. A two-step static simulation is employed. During the first step, a “ $z$ ” displacement is prescribed

at node A and during the second step, a “ $y$ ” displacement is prescribed at the same point. Figure 25 illustrates the prescribed displacements. In the 1st solution-step a displacement  $u_{z1} = 0.5 \text{ m}$  is applied in 1s and in the 2nd solution-step a displacement  $u_{y2} = 2 \text{ m}$  is applied in 1 s. In this simulation the normal interface law parameters  $\epsilon_{e1} = 1E7 \text{ N/m}$  and  $\epsilon_{e2} = 1$  are adopted.

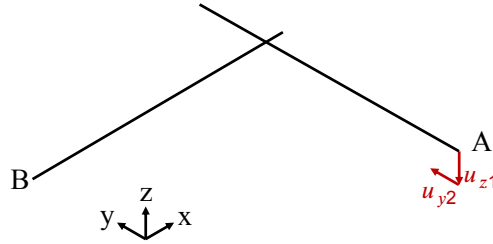
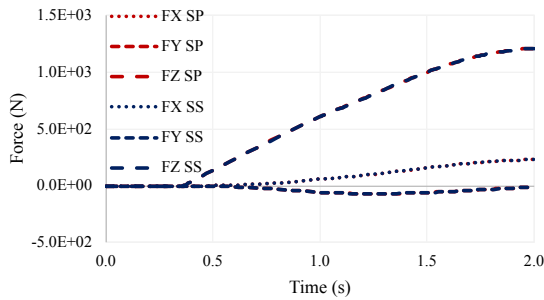
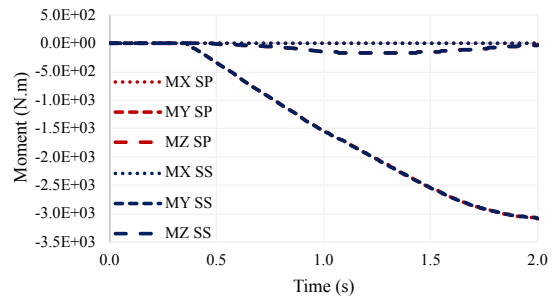


Figure 25: Representation of perpendicular beams model example with prescribed displacements [2].

The resulting reactions forces and moments are presented at point B in Figure 26a and Figure 26b. The graphs in both figures show practically the same reaction response for the “SP” and “SS” contact descriptions.



(a) Force reactions in point B.



(b) Moment reactions in point B.

Figure 26: Reactions obtained at point B in the perpendicular beams contact example with normal contact [2].

Figure 27 illustrates some instants of the simulation with normal contact forces obtained by both contact models. The red arrows indicate the forces obtained from the “SP” model and the blue arrows obtained from the “SS” model. As highlighted in Figure 28, the difference in both contact formulations is negligible. The spline-based contact is represented in Figure 28a and the surface-to-surface contact is represented in Figure 28b with the normal forces at each beam surface.

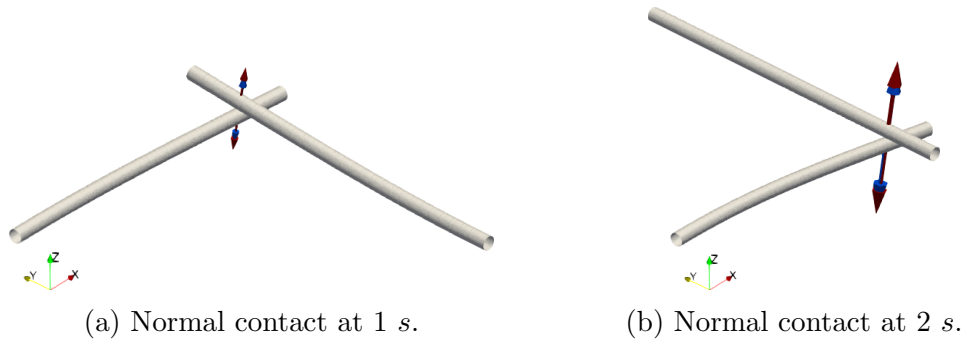


Figure 27: Perpendicular beams contact with red arrows and blue arrows representing respectively the “SP” model and the “SS” model. Simulation includes normal contact only [2].

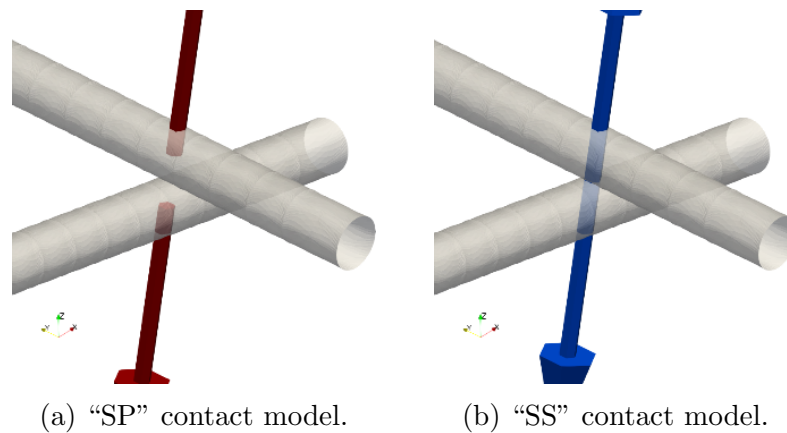


Figure 28: Detailed view of the normal contact forces representation [2].

#### 5.1.1.2 Normal & Tangential Contact

In this simulation, normal and tangential contact interactions are considered. The normal contact parameters adopted are  $\epsilon_{e1} = 1E7 \text{ N/m}$  and  $\epsilon_{e2} = 1$  while the tangential contact parameters are  $\epsilon_{te} = 1E6$  and  $\mu_s = \mu_d = 0.3$ .

The reaction forces and the reaction moments of point B are presented in Figure 29a and Figure 29b. Again, these results demonstrate that the spline-based contact response is very similar to the surface-to-surface contact, even considering the tangential contribution. However, there is a slight difference in the results at time 1s. Figure 29c and Figure 29d present force and moments reactions at point B from 0.9 s to 1.1 s. The difference between the “SP” and “SS” formulations naturally rises from the distinct material points where the tangential forces are acting at. In spline-based contact, tangential forces are applied at the beam centerline while in surface-to-surface contact tangential forces are applied at the surface. This issue is discussed and illustrated in [78]. The spline-based tangential contact definition neglects moments that may arise from the surface to the

beam centerline. However, as seen in this simulation, the relevance of this approximation depends highly on the beam slenderness and the contact interaction.

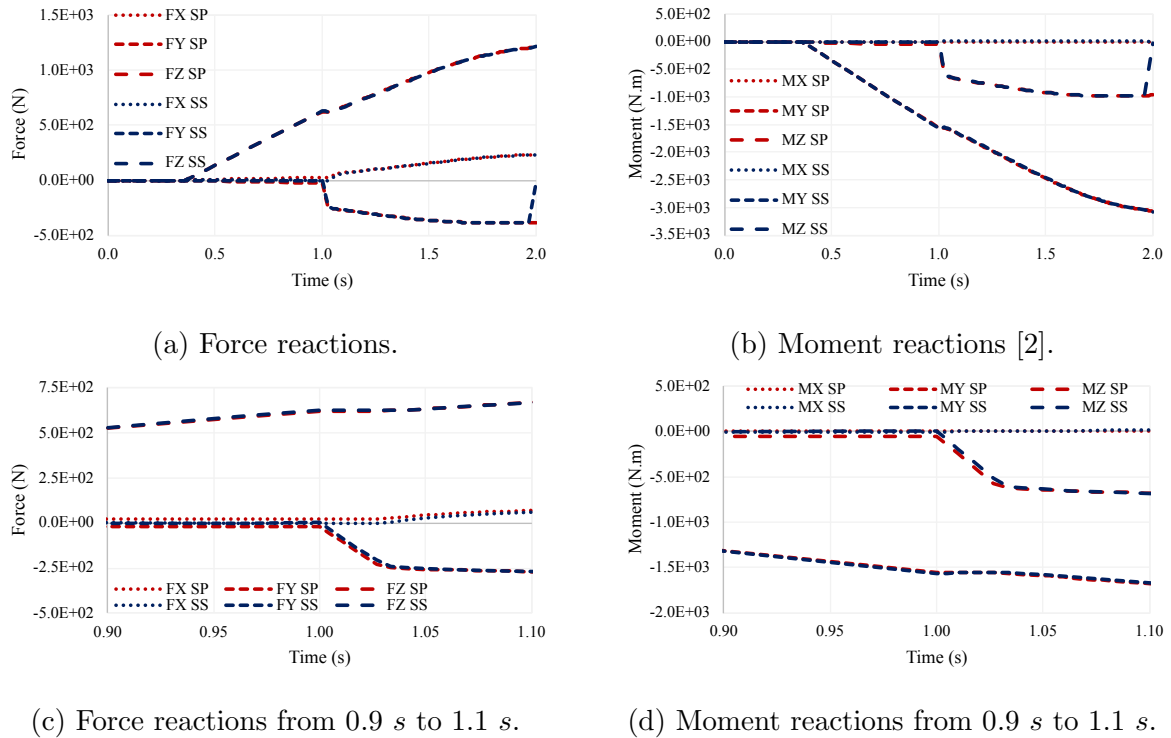


Figure 29: Reactions obtained for point B in the perpendicular beams contact example with normal and tangential contact [2].

Figure 30 depicts the contact of beams with normal and frictional forces at selected configurations. The forces in red and the forces in blue were respectively obtained from the “SP” model and the “SS” model.

### 5.1.1.3 Normal & Tangential Contact with Rotations

In the third simulation, an axial rotation is included in the displacement imposed at the second solution-step. In the 1<sup>st</sup> solution-step a displacement  $u_{z1} = 0.5 \text{ m}$  is applied in 1 s and in the 2<sup>nd</sup> solution step a displacement  $u_{y2} = 2 \text{ m}$  and a rotation  $\theta_{y2} = 25 \text{ rad}$  are simultaneously applied in 1 s. The prescribed displacement field is illustrated in Figure 31.

The reaction forces and moments at point B are presented in Figure 32. The results show very similar behavior for “SP” and “SS” in terms of “z” force and “y” moment. However, the results for FX are different, except for the “x” moment which is negligible. The reason for this difference lies in the tangential contact definition as mentioned in the previous simulation. While the contact parameters for this simulation were the same as in the previous cases, the large prescribed rotation increased the relevance of the surface

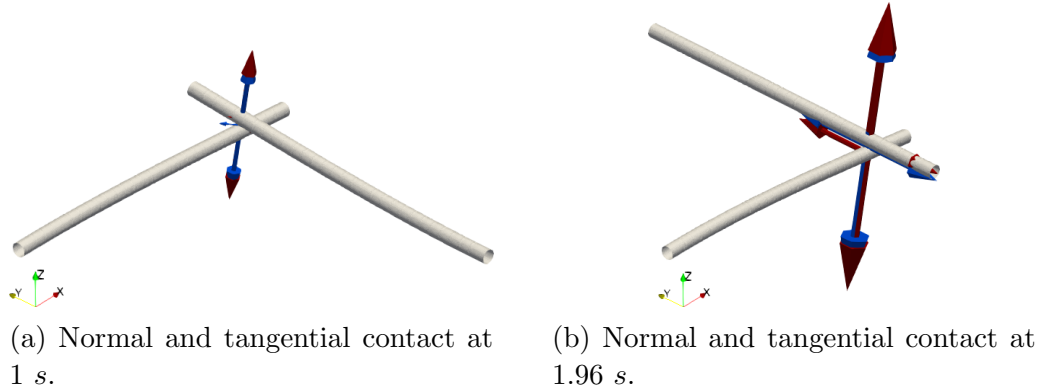


Figure 30: Perpendicular beams contact with red arrows and blue arrows representing respectively the “SP” contact model and the “SS” contact model. Simulation including normal and tangential contact [2].

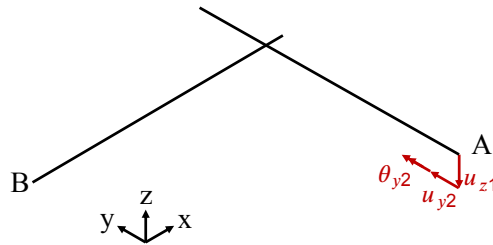


Figure 31: Representation of perpendicular beams model example with prescribed displacements including rotation [2].

contact forces.

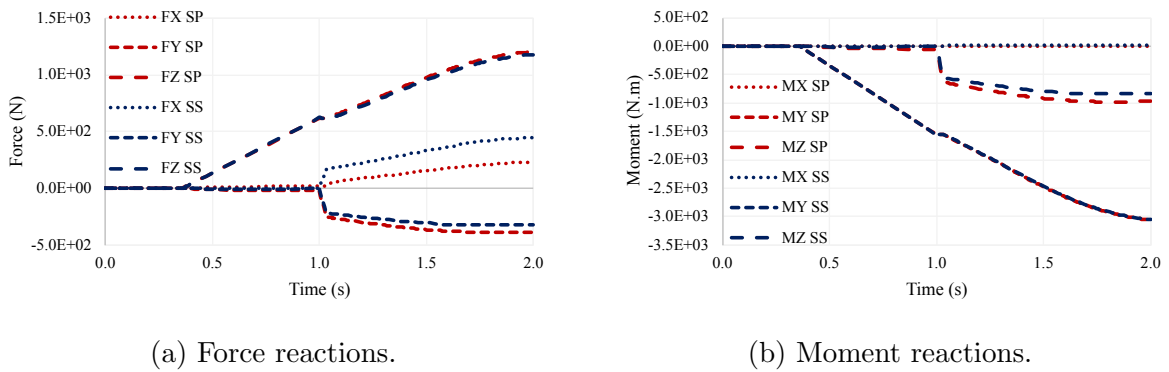


Figure 32: Reactions obtained for point B in the perpendicular beams contact example with normal and tangential contact including rotations [2].

Figure 33 illustrates the normal and tangential contact of the beams at two instants. In this figure, the red arrows stand for the results with “SP” model while the blue arrows stand for the results with the “SS” model. Figure 34 highlights the orientation difference in the frictional forces obtained in both models due to the prescribed rotation.

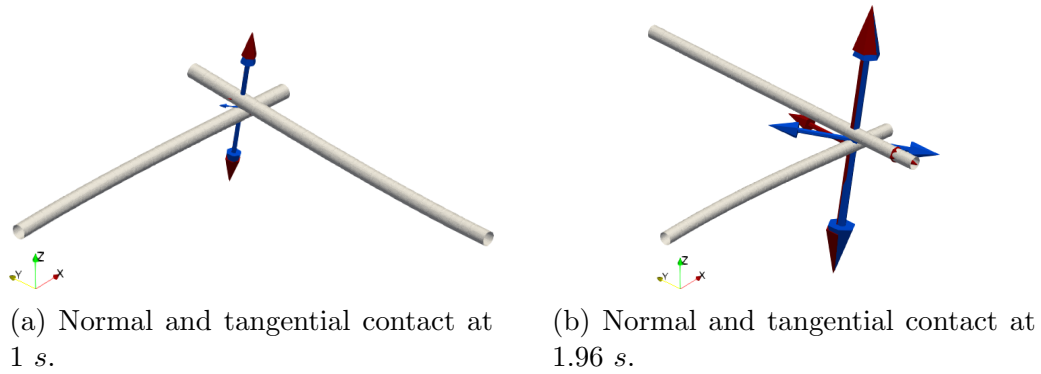


Figure 33: Perpendicular beams contact with red arrows and blue arrows representing respectively the “SP” contact model and the “SS” contact model. The simulation includes normal and tangential contact with rotations [2].

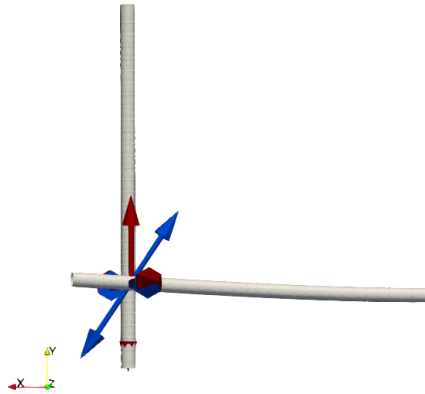


Figure 34: Perpendicular beams contact with red arrows and blue arrows representing respectively the “SP” contact model and the “SS” contact model. The simulation includes normal and tangential contact with rotations. Top view at instant 1.96 s [2].

#### 5.1.1.4 Basis Functions, Objectivity, and Convergence

The objective of this subsection is to comment on three relevant aspects in the context of the proposed contact formulation: the spline basis functions’ influence on the contact forces distribution, the consistency in an objectivity test, and the convergence behavior.

To show the spline basis influence on the contact forces nodal distribution, a static simulation with prescribed displacements as presented in Figure 25 is performed. In the 1<sup>st</sup> solution-step a displacement  $u_{z1} = 0.25 \text{ m}$  is applied in 1 s and in the 2<sup>nd</sup> solution-step a displacement  $u_{y2} = 2 \text{ m}$  is applied in 1 s. In this simulation only normal contact interaction is considered with the parameters  $\epsilon_{e1} = 1E7 \text{ N/m}$  and  $\epsilon_{e2} = 1$ .

In this simulation, however, all nodes in the beam with prescribed displacements are taken as a single rigid body. The objective of this assumption is to collect the reaction forces in some nodes to analyze the contact forces distribution. Figure 35 presents the “z” reaction forces obtained on 5 beam nodes as presented in Table 4. Figure 35a presents



Table 4: Initial position of nodes taken for basis function analysis.

$\mathbf{P}_1 = (0, 2.5, 0.8)$
$\mathbf{P}_2 = (0, 2.5, 0.9)$
$\mathbf{P}_3 = (0, 2.5, 1.0)$
$\mathbf{P}_4 = (0, 2.5, 1.1)$
$\mathbf{P}_5 = (0, 2.5, 1.2)$

the reaction forces in a simulation with the spline-based formulation while Figure 35b presents the reaction forces in a simulation with the surface-to-surface contact formulation. The results show that peak values of the “SP” formulation are lower than the “SS” formulation due to the spline basis functions nature. Moreover, the “SP” model reaction forces reproduce the smooth  $C^1$  shape of the spline basis functions considered, as expected.

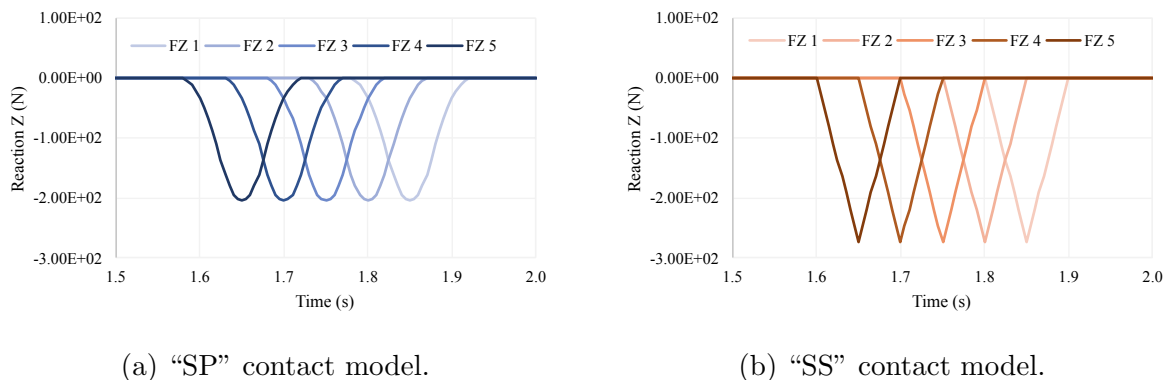


Figure 35: Basis functions influence on the nodal reaction forces on five nodes [2].

The second relevant aspect is the formulation consistency when undergoing large displacements and rotations. To analyze the model’s robustness, an objectivity test involving three solution-steps is proposed. The displacements adopted for the objectivity test are illustrated in Figure 36 and detailed in Table 12 (see Appendix 7.1).

In the first solution-step ( $0 \leq t < 1 \text{ s}$ ), a displacement is imposed at point B to induce contact. In the second solution-step ( $1 \leq t < 2 \text{ s}$ ), displacements and rotation are imposed at points A and B to simulate a rotation in the “ $xy$ ” plane. In the third solution-step ( $2 \leq t < 3 \text{ s}$ ), displacements and rotations are imposed in point B while rotations are imposed in point B to simulate a rotation in the “ $xz$ ” plane.

The reaction forces and moments on point B in each direction during the objectivity test are presented in Figure 37. In this figure, the results indicated as “FT” and “MT” represent, respectively, the reaction force and moment magnitudes. The results in Figure 37 show that despite large displacements and rotations, reaction forces and moments magnitudes are kept as expected. Figure 38 presents some configurations during

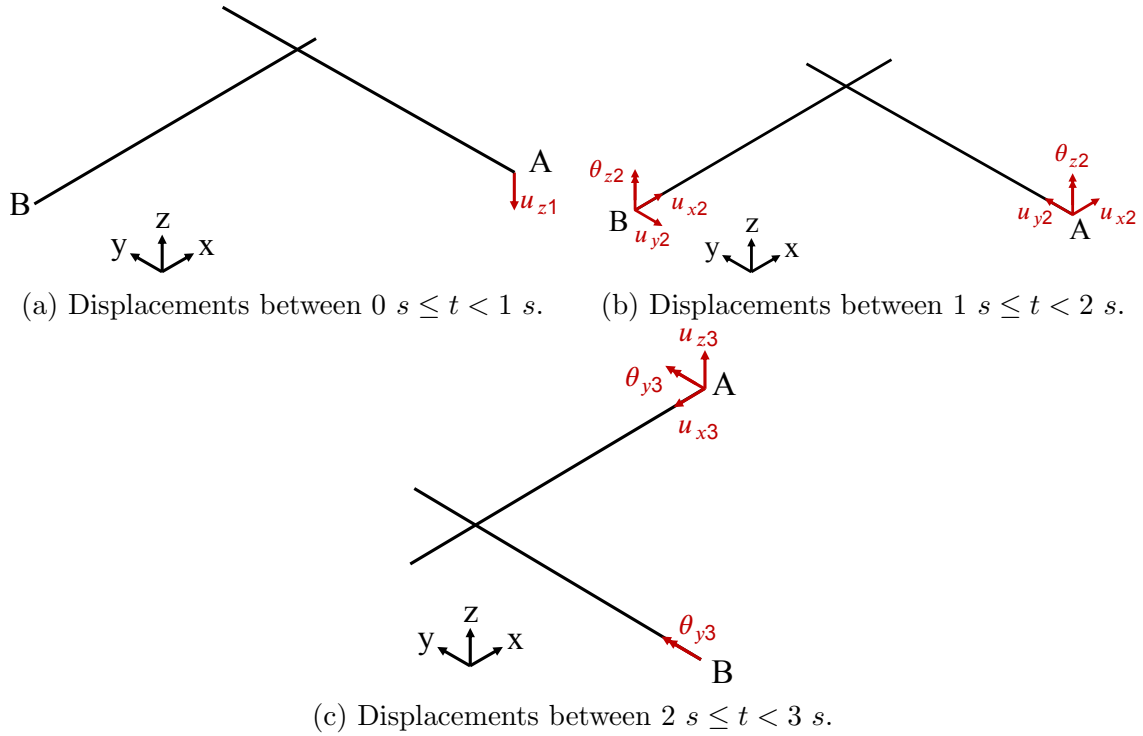
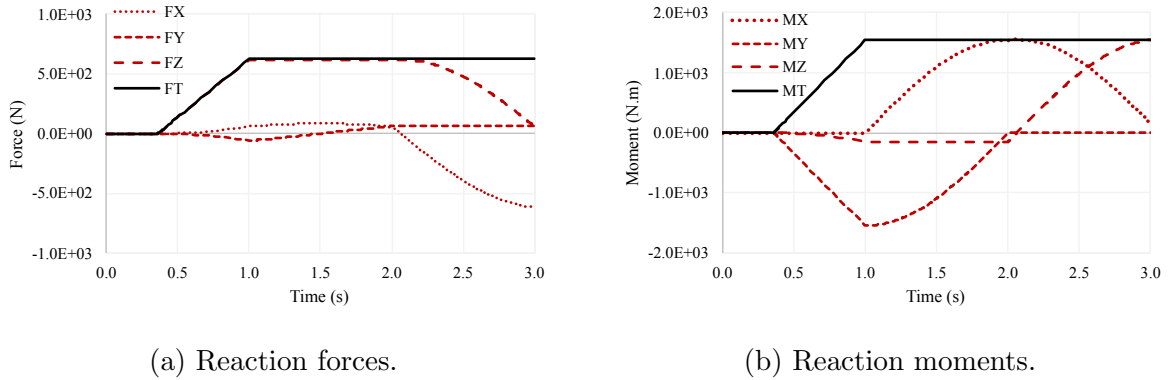


Figure 36: Prescribed displacements adopted in the objectivity test [2].

the objectivity test.



(a) Reaction forces.

(b) Reaction moments.

Figure 37: Reaction forces and moments on point B in the objectivity test [2].

The last relevant aspect of the proposed formulation is the convergence behavior. Figure 39 presents some convergence results for the numerical example (i) with respect to three distinct uniform meshes composed of 30, 60, and 120 elements for each beam and respectively indicated as “M1”, “M2”, and “M3”. Figure 39a presents the tip displacements of the beam fixed at point B. Figure 39b shows the internal forces at the first beam element next to point B. In this figure “N1”, “N2”, and “N3” are respectively associated with shear force in the “y” global direction, shear force in the “z” global direction, and axial force in the “x” global direction, all in the reference configuration. This convergence study demonstrates that the mesh initially adopted is sufficiently refined for the

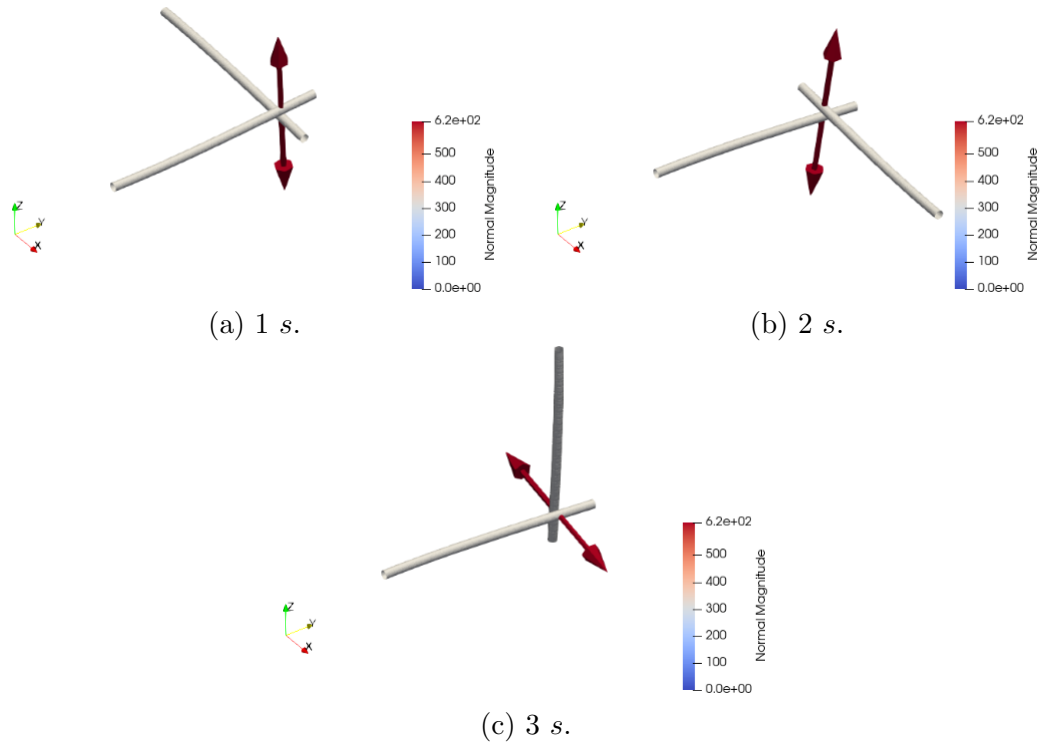


Figure 38: Normal contact force at some configurations in the objectivity test [2].

simulations proposed.

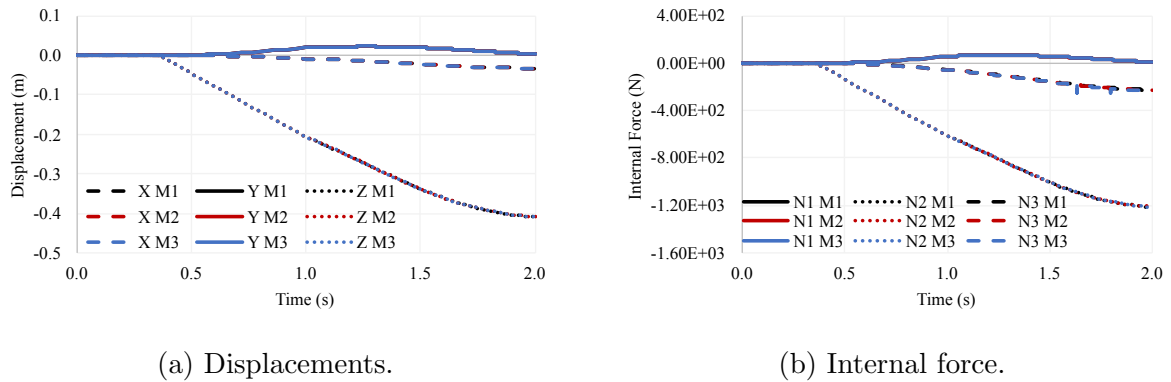


Figure 39: Convergence analysis for the perpendicular beams numerical example 5.1.1.1 for three different meshes with 30, 60, and 120 elements in each beam indicated respectively with suffixes “1”, “2”, and “3” [2].

## 5.1.2 Octagonal Ring

The objective of this example is to compare the spline-based smooth formulation with the surface-to-surface formulation in contact scenarios with finite element corners without refinements. This example consists of imposing displacements on a cantilevered beam to induce contact with a fixed octagonal ring made of beam elements. Figure 40 describes the model setup and the imposed displacements. Figure 41 shows the finite

Table 5: Octagonal ring example simulation data. The variable  $t$  is the total simulation time.

Simulation data			
Displ. 1 <sup>st</sup> solution-step (m) and simulation time (s)	$u_{x1} = 0.8$ 1	Displ. 2 <sup>nd</sup> solution-step (m) and simulation time (s)	$u_2 = \begin{cases} u_{x2} = 2.7 - 2.7\cos\left(\frac{t-1}{25}\right) \\ u_{y2} = 2.7\sin\left(\frac{t-1}{25}\right) \end{cases}$ 50 $\pi$

element mesh in black color with nodes in orange color and the contact surfaces “SP” and “SS” in gray color. In this simulation, a material with  $E = 200E9 \text{ N/m}^2$ , Poisson ratio  $\nu = 0.3$ , and a specific mass of  $3000 \text{ kg/m}^3$  is considered. The straight beam is composed of three elements with a radius of  $0.2 \text{ m}$  and a length of  $18 \text{ m}$ . Point A is located at  $(3.5, 0, -17) \text{ m}$ . The octagonal ring is composed of 16 beam elements with a radius of  $0.1 \text{ m}$ . The octagonal ring is centered at  $(0, 0, 0) \text{ m}$  and has a side of  $2.2961 \text{ m}$ .

Two dynamic solution-steps are prescribed in this simulation. In the first solution-step an “ $x$ ” displacement is defined at point A to introduce the first contact. After that, a combination of “ $x$ ” and “ $y$ ” displacements are defined to prescribe a circular displacement around the octagonal ring. The simulation data for this example is presented in Table 5. This simulation is performed in a dynamic framework with an adaptive time-step ranging from  $1E - 4 \text{ s}$  to  $1 \text{ s}$  and Newmark integration parameters  $\beta = 0.3$  and  $\gamma = 0.55$  (see [79]). The following contact parameters are considered, normal interface law  $\epsilon_{e1} = 1E7 \text{ N/m}$ , normal interface law  $\epsilon_{e2} = 1$ , normal damping coefficient  $c_{nd} = 1E4 \text{ Ns/m}$ , static friction coefficient  $\mu_s = 0.55$ , dynamic friction coefficient  $\mu_d = 0.4$ , tangential penalty parameter  $\epsilon_{te} = 1E5 \text{ N/m}$ , frictional damping coefficient  $c_{td} = 0 \text{ Ns/m}$ .

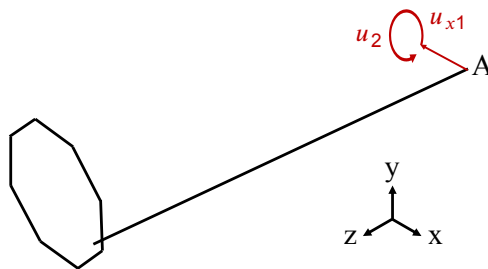


Figure 40: Representation of ring model example with prescribed displacements [2].

The reaction forces at point A are presented in Figure 42a and, in detail, in Figure 42b. The norm of the normal and tangential forces are shown in Figure 42c and, in detail, in Figure 42d. Figure 43 depicts contact forces at several simulation instants. At the very beginning, there is an impact caused by the first contact of the cantilever beam with the octagonal ring. The effect of this first contact, however, rapidly decays as observed

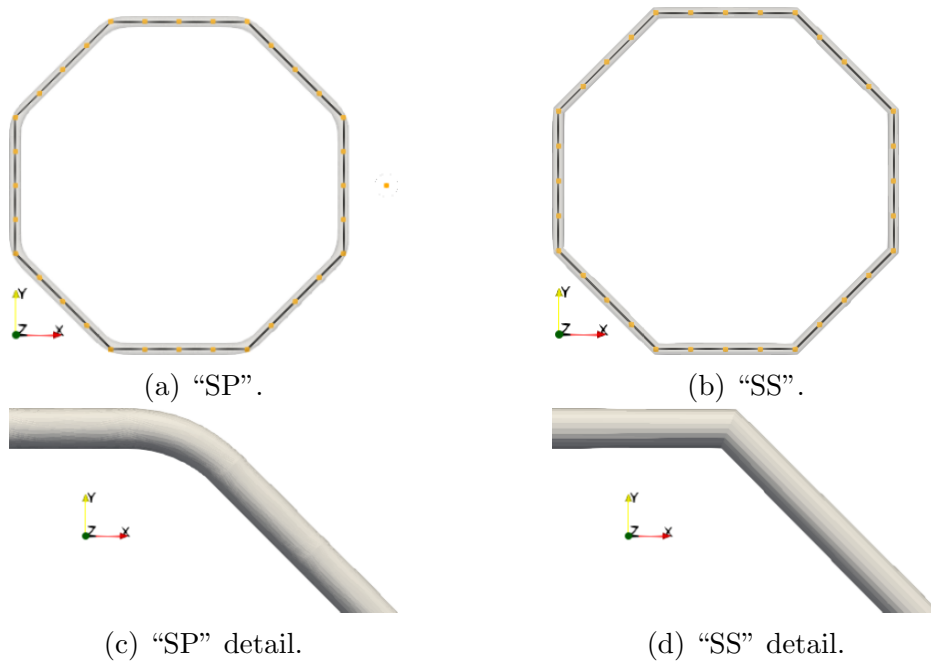


Figure 41: Octagonal ring model finite element mesh in black color with nodes in orange color and contact surfaces in gray color [2].

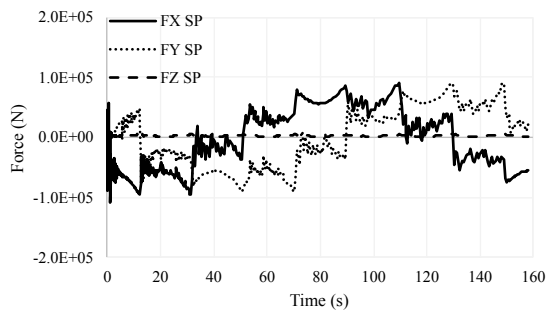
between 0  $s$  and 3  $s$ . On the other hand, there is, during the whole simulation, a high-frequency oscillation triggered by stick-slide frictional contact with different frictional coefficients. This behavior is observed around 71  $s$  and 129  $s$ . At these instants, a maximum normal force occurs simultaneously with a stick-slide frictional interaction. The maximum normal forces always occur at the corners of the octagonal ring since they are more distant from the ring's center. Again, the proposed model can handle impacts and static/dynamic frictional contact interaction in challenging scenarios involving finite element corners.

The results in Figure 42b and Figure 42d reflect the difference between the “SP” and the “SS” contact strategies. Both models present very similar responses until 12  $s$ . Approximately at this instant, the “SP” model passes the first octagonal corner. The “SS” model instead continues until 17  $s$  when it passes the corner kink and then diverges.

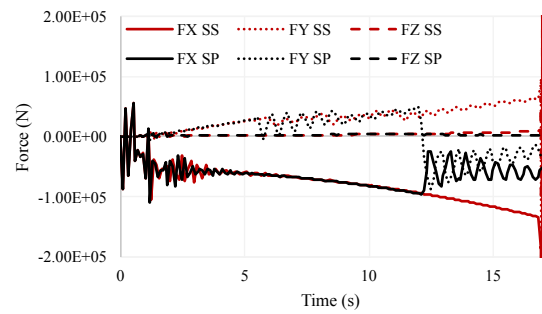
### 5.1.3 Wave-shaped Obstacle

The objective of this example is to compare the spline-based smooth contact in corners defined by two adjacent finite elements with the surface-to-surface contact described by multiple finite elements. For that, simulations involving the contact of a cantilevered beam with a wave-shaped obstacle are proposed.

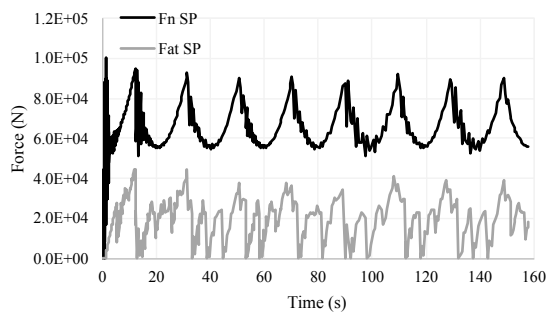
Several prescribed displacements are imposed in a cantilevered beam to induce contact



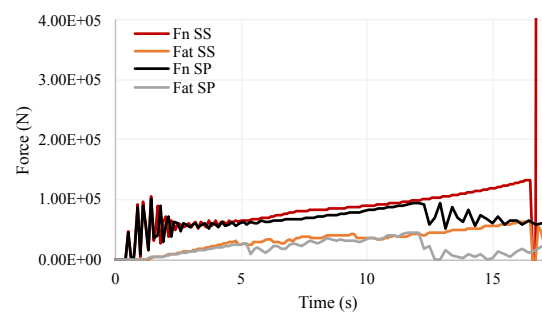
(a) Force reactions.



(b) Force reactions in detail.



(c) Total normal (Fn) and friction force (Fat).



(d) Total normal (Fn) and friction force (Fat) in detail.

Figure 42: Reactions forces for point A and normal and friction forces obtained in the ring obstacle contact example [2].

with a wave obstacle consisting of beam elements. Figure 44 describes the model setup with displacements imposed at point A and the wave obstacle that is fixed at points B and C. In this simulation, a material with  $E = 200E9 \text{ N/m}^2$ , a Poisson ratio of  $\nu = 0.3$ , and a specific mass of  $8000 \text{ kg/m}^3$  is considered. The straight beam is composed of two beam elements of radius  $0.1 \text{ m}$  and has a length of  $6 \text{ m}$ . Point A is located at  $(-0.2, -5.5, 0.3) \text{ m}$ . The wave obstacle is composed of four beam elements with a radius of  $0.1 \text{ m}$  and a side of  $\sqrt{4.5} \text{ m} \approx 2.12132 \text{ m}$ . Points B and C are respectively located at  $(0, 0, 0) \text{ m}$  and  $(6, 0, 0) \text{ m}$ . Figure 45 shows the finite element meshes in black with the nodes in orange and the contact surfaces in gray. In this simulation, five dynamic solution-steps are defined. The simulation data is presented in Table 6. This simulation is performed in a dynamic framework with Newmark parameters  $\beta = 0.3$  and  $\gamma = 0.55$  (see [79]) and an adaptative time-step ranging from  $1E - 2 \text{ s}$  to  $1E - 1 \text{ s}$ . Moreover, the following contact parameters are adopted, normal interface law parameter  $\epsilon_{e1} = 1E7 \text{ N/m}$ , normal interface law parameter  $\epsilon_{e2} = 1$ , normal damping coefficient  $c_{nd} = 1E1 \text{ Ns/m}$ , static and dynamic friction coefficients  $\mu_s = \mu_d = 0.3$ , tangential penalty parameter  $\epsilon_{te} = 1E5 \text{ N/m}$ , and frictional damping parameter  $c_{td} = 1E1 \text{ Ns/m}$ .

The reaction forces at point A are presented in Figure 46a and the norm of the

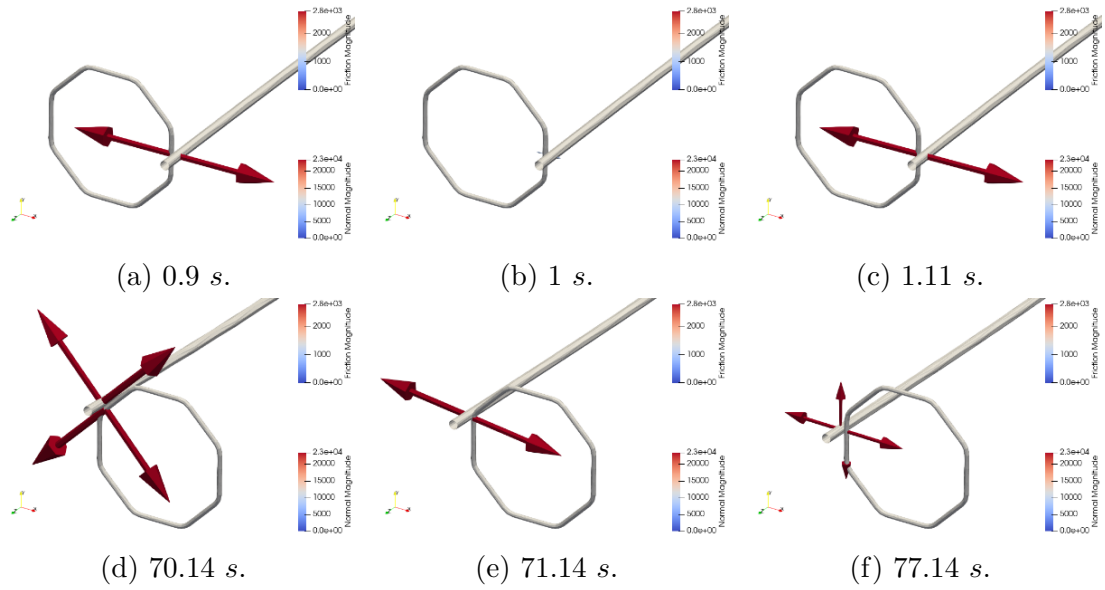


Figure 43: Normal and tangential contact forces at several instants of the ring obstacle example [2].

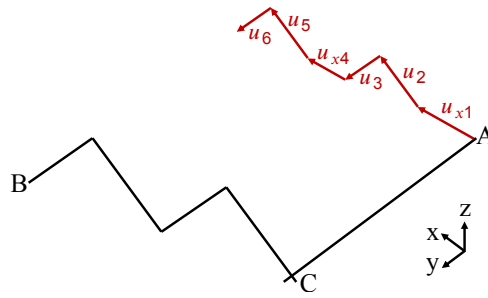


Figure 44: Representation of wave-shaped model example with prescribed displacements [2].

normal ( $F_n$ ) and friction forces ( $F_{at}$ ) are depicted in Figure 46b. Figure 47 demonstrates the normal and tangential contact at some relevant simulation instants. The results show an increasing normal and tangential force due to contact from 10 s to 20 s the displacement imposed in the horizontal direction. After that, the forces slightly decrease while the displacement follows the wave obstacle just before 30 s. Around that instant, the cantilevered beam approaches the peak of the wave obstacle leading to a slight decrease at 30 s. From 30 s to 40 s the cantilevered beam swings around the wave obstacle finally passing the top. Then, the cantilevered beam goes to the valley of the wave with the minimum normal force at 45 s. An analogous behavior occurs until the end of the simulation. This simulation underlines that the proposed formulation is able to smooth sharp finite element corners and can handle the contact conveniently.

Additionally, the results in Figure 46a show that both contact formulations have very similar responses until approximately 30 s. A few seconds later, the reaction forces

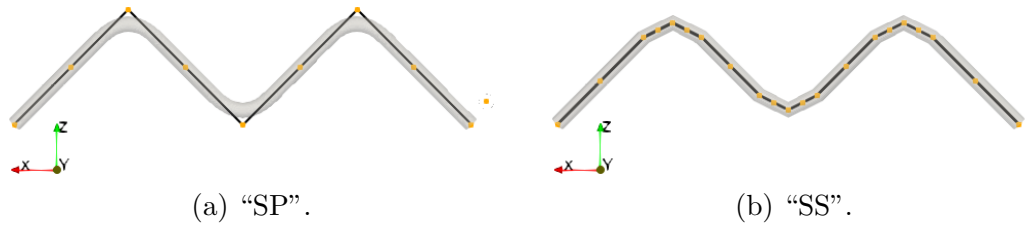


Figure 45: Wave-shaped obstacle finite element meshes in black color with nodes in orange color and contact surfaces in gray color [2].

Table 6: Wave-shaped obstacle example simulation data.

Simulation data			
Displ. 1 <sup>st</sup> solution-step (m)	$u_{x1} = 0.95$		
and simulation time (s)	20		
Displ. in each subsequent solution-step (2 <sup>nd</sup> to 5 <sup>th</sup> ) (m) and simulation time in each subsequent solution-step (s)	$u_2 = \begin{cases} u_{x2} = 1.7 \\ u_{y2} = 0.75 \end{cases}$ $u_5 = \begin{cases} u_{x5} = 4.7 \\ u_{y5} = 0.75 \end{cases}$	$u_3 = \begin{cases} u_{x3} = 2.45 \\ u_{y3} = 0 \end{cases}$ $u_6 = \begin{cases} u_{x6} = 5.45 \\ u_{y6} = 0 \end{cases}$	$u_{x4} = 3.95$

decrease on the “SP” simulation while keeps increasing on the “SS” model. Similar behavior is also observed in Figure 46b. It is possible to assume, by observing the “SP” model, that the kinks play an important role. When the cantilevered beam passes the first kink, there is an abrupt change in the contact direction. This effect is seen in the “SP” model “ $x$ ” reaction force just after 30  $s$ . After that, the contact forces keep increasing, see Figure 46b, as the cantilevered beam reaches the second kink. However, around 40  $s$  the “SS” model diverges.

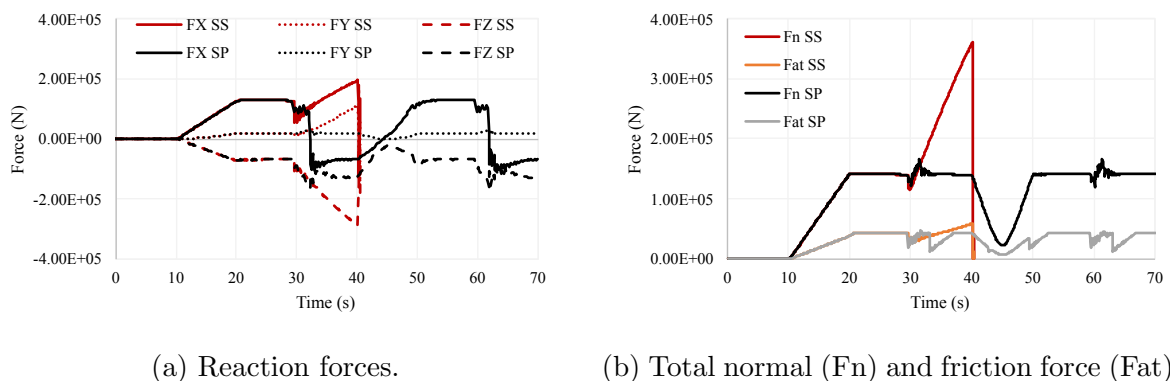


Figure 46: Reactions forces for point A and normal and friction forces obtained in the wave-shaped obstacle contact example [2].



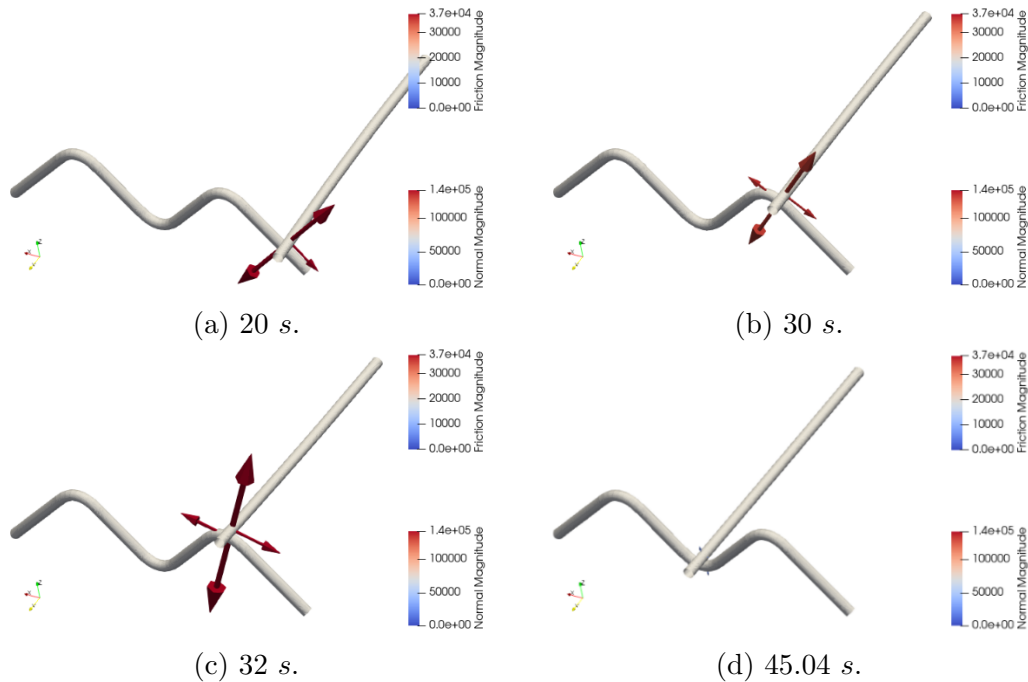


Figure 47: Normal and tangential contact forces at several instants of the wave-shaped obstacle example [2].

#### 5.1.4 Alternative Smooth Contact Formulation

The objective of this numerical example is to compare the proposed spline-based contact formulation with an alternative smooth contact formulation. To achieve this goal a simulation that reproduces an example from Magliulo, Zilian, and Beex [24] is adopted. The authors' strategy consists of producing smooth surfaces based on beam centerlines approximated by Bézier curves in beam corners. There are, however, three main differences that should be noted: the contact surface geometry, the contact interaction strategy, and the compliance law. In [24] the contact surface is defined by beams with elliptical cross-section while in the present work only beams with circular cross-section are adopted. Moreover, in [24] contact interaction is treated in a surface-to-surface master-slave framework while in this work a pointwise master-master strategy is adopted. Moreover, as the spline contact model is decoupled from the structural theory it is possible to produce a simulation that combines an elliptical cross-section with a circular contact surface as presented in Figure 48a. Finally, in [24] a combination of cubic and quadratic normal contact potentials is adopted while in this particular example, a resulting quadratic potential is considered.

The simulation setup is defined by two initially straight, perpendicular, and elliptical cross-section beams in a single touch configuration at their mid-span, see Figure 48b. A material with Young's Modulus of  $100\text{GPa}$  and Poisson ratio of 0.3 is adopted [24].

Table 7: Displacement field adopted to reproduce perpendicular beams simulation. Rotations were applied around the beam center.

Time (s)	Displacement Field	Time (s)	Displacement Field
$0 \text{ s} \leq t < 1 \text{ s}$	$u_{a_2} = -1.5 \text{ cm}$	$3 \text{ s} \leq t < 4 \text{ s}$	$\theta_{a_2} = -\frac{\pi}{6} \text{ rad}$
$1 \text{ s} \leq t < 2 \text{ s}$	$u_{a_1} = 0.5\cos(\pi/4) \text{ cm}$ $u_{a_3} = 0.5\sin(\pi/4) \text{ cm}$	$4 \text{ s} \leq t < 5 \text{ s}$	$u_{a_1} = -0.5\cos(\pi/4) \text{ cm}$ $u_{a_3} = -0.5\sin(\pi/4) \text{ cm}$
$2 \text{ s} \leq t < 3 \text{ s}$	$\theta_{a_2} = \frac{\pi}{6} \text{ rad}$	$5 \text{ s} \leq t < 6 \text{ s}$	$u_{a_2} = 1.5 \text{ cm}$

Moreover, each beam is composed of 16 beam elements with an elliptical cross-section of radius  $0.3\text{cm}$  and  $0.1\text{cm}$ , and a length of  $8\text{cm}$  [24]. The simulation is defined by 6 displacement fields of one second each imposed at the boundaries of one beam to induce contact. The simulation is static and, therefore, the time variable is used only to gradually impose displacements. The other beam boundary displacements and rotations are fixed. The displacement field adopted is presented in Table 7. The displacement field depicted in Table 7 was based on figures presented in [24], as illustrated in Table 8. A normal contact interface law parameter  $\epsilon_{e1} = 1E8 \text{ N/m}$  and a normal contact interface law parameter  $\epsilon_{e2} = 1$  are adopted for this simulation.

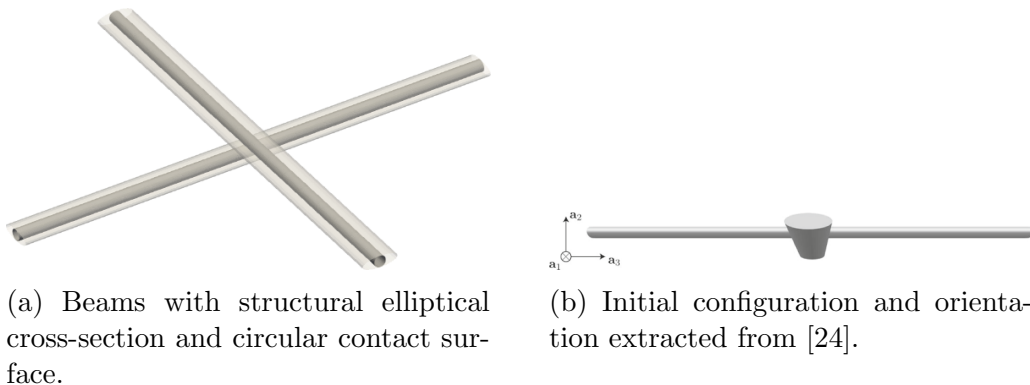

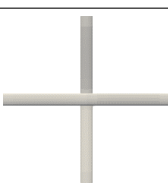

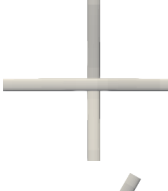

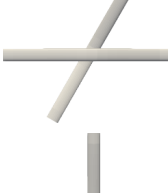

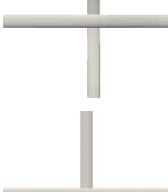




Figure 48: Models overview [2].

The horizontal beam left end, see orientation in Table 8, reactions for both contact formulations are presented in Figure 49. In this figure, the dashed line results indicated as “MZZB” were extracted from [24] and solid line results were obtained in the spline-based contact formulation. The results in Figure 49a show that both formulations present very similar reactions despite the formulation differences. It is possible to note, however, more oscillations in the “SP” model when compared to the “MZZB” model between  $1 \text{ s}$  and  $5 \text{ s}$ . This oscillation is caused by the pointwise contact interaction and the contact surface geometry assumptions. These characteristics lead to contact components that would not be expected in [24]. This effect is also observed in the results of Figure 49b between  $1 \text{ s}$  and  $5 \text{ s}$ . These results show higher “SP” model reactions when compared to the “MZZB”

Table 8: Simulation overview comparative figures at several time steps.

	Extracted from [24]	Present work
$t = 1 \text{ s}$		
$t = 2 \text{ s}$		
$t = 3 \text{ s}$		
$t = 4 \text{ s}$		
$t = 5 \text{ s}$		

model due to the differences mentioned. It is possible to consider, then, that both models could represent the proposed problem considering their own advantages and limitations.

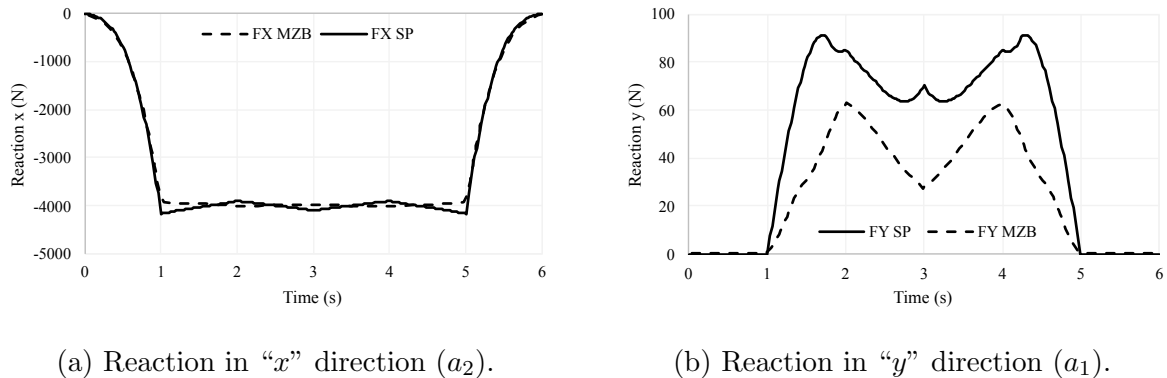


Figure 49: Horizontal beam left end reaction forces as illustrated in Table 8. Reaction forces indicated as MZB adapted from [24]. Extracted from [2].

## 5.2 Conformal Contact

### 5.2.1 Twisting Beams

The objective of this example is to test the proposed numerical strategy in a 3D near-conformal contact scenario. In this example, cantilevered beams are twisted at their ends. Moreover, two models are adopted, the former with two beams (TB1), and the latter with seven beams (TB2). Though friction may be not negligible at beams’ surfaces, only normal contact interaction is considered in this example.

Figure 50 illustrates the twisting beams simulation setup for TB1. To impose the twisting a rigid element connecting the beams’ ends is defined (points B and D) while a rotation is imposed at its middle point (point E) [80]. The simulation setup for TB2 is similar to TB1, however with seven beams. Simulation TB2 is defined by one central beam CD with six equally spaced instances of beam AB around. Figure 51 presents the front view of TB1 and TB2 with the rigid elements defined.

All beams in this example are composed of 25 elements with a total length of 5  $m$  and a radius of 0.049  $m$ . The distance between beam centerlines is 0.1  $m$  for TB1. For TB2 a 0.1  $m$  distance is also adopted, taking as reference the central beam and the rotated copies of AB. For both simulations, a rotation  $\theta_x = 4\pi$  is imposed with a total simulation time of 10  $s$ . The simulation is used only to gradually impose the displacements as TB1 and TB2 are performed quasi-statically. A material with  $E = 2E9 \text{ N/m}^2$  and Poisson ratio of  $\nu = 0.3$  is adopted. A linear normal penalty parameter of  $5.5E5 \text{ N/m}$  is considered.

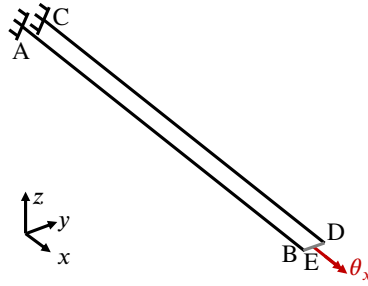


Figure 50: Twisting beams simulation setup for TB1 [3].

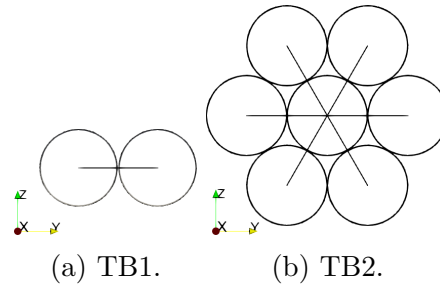


Figure 51: Front view with rigid elements [3].

The axial and moment reactions evolution at point E are presented in Figure 52. This figure shows that the reaction evolution is more intense in TB2 when compared with TB1. This is an expected result since outside beams in TB2 experience higher elongations than beams in TB1. The final TB2 reaction is almost ten times greater than TB1 reaction.

Figure 53 presents the axial force in the final configuration for TB1 and TB2. This figure shows, as expected, an almost homogeneous axial forces distribution for TB1 and a radial symmetric forces distribution for TB2. It is still possible to observe some compression at the tips of beam AB in TB2. This effect is caused by the substantial beams' penetration in contrast to boundary constraints. Figure 53 also illustrates the final configuration of normal contact forces for TB1 and TB2. In the final configuration, TB1 presents 46 contact pairs while TB2 shows 116 contact pairs. This example shows that the proposed formulation could handle near conformal contact scenarios even considering large deformations.

### 5.2.2 Sliding Beams

The objective of this example is to explore the proposed numerical strategy in a scenario where a beam slides on the top of another beam with normal contact interaction. The main challenge in this example lies in switching contact interactions between different spline elements with large deformations.

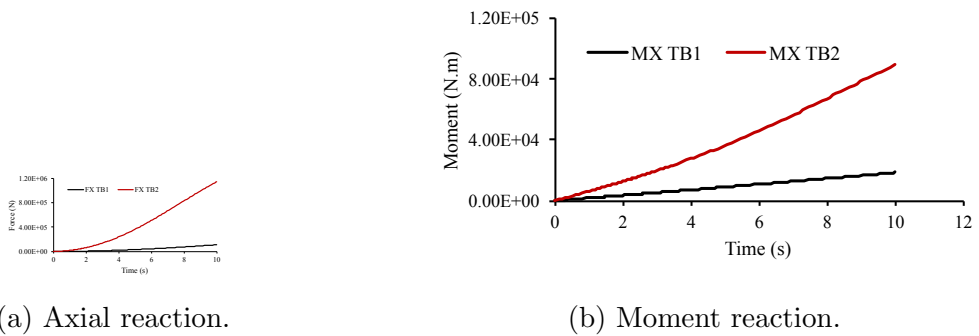


Figure 52: Twisting beams example axial and moment reaction force at point E [3].

Figure 54 illustrates the example setup. In this example, each beam is composed of 15 beam elements with a radius of  $0.06\text{ m}$ . Both beams are  $3\text{ m}$  long with an initial overlapping projection of  $1\text{ m}$  in the  $x$  axis and  $z$  gap of  $0.3\text{ m}$ . Moreover, a material with Young's Modulus  $E = 2E9\text{ N/m}^2$  and Poisson ratio  $\nu = 0.3$  is considered. A linear normal penalty parameter  $1E6\text{ N/m}$  is assumed for the contact interactions. Friction is not considered in this example.

The static simulation is performed in two solution-steps. The time parameter in this example is used only to gradually impose the displacements. In the first solution-step a  $u_{z1} = 1.5$  displacement is imposed in  $5\text{ s}$ . After, in the second solution-step, a  $u_{x2}$  displacement is applied in  $10\text{ s}$ .

The reaction forces and moment at point E are presented in Figure 55. This figure shows two clearly different stiffness behaviors at the distinct solution-steps. From  $0\text{ s}$  to  $5\text{ s}$ , the reactions are mainly ruled by beams' bending. After, from  $5\text{ s}$  to  $10\text{ s}$ , an  $x$  displacement is imposed changing the models' stiffness response. Figure 56 shows several normal contact configurations as the contact interactions move along spline elements.

### 5.2.3 Parallel Beams

The objective of this example is to explore the proposed formulation in challenging conformal contact scenarios. For that, an example first presented in [25] as "Contact between points and surfaces (master-slave)" is considered. It is important to mention that in [25] beams' cross-sections are defined as super ellipsis with exponent  $n = 10$  with surface-to-surface contact interaction. Instead, in this work circular cross-sections are adopted with beam-to-beam contact interaction. The circular cross-sections are considered in this example only to formulate the contact interaction while all beam finite elements characteristics are kept. Figure 57 illustrates the contact elements in red and

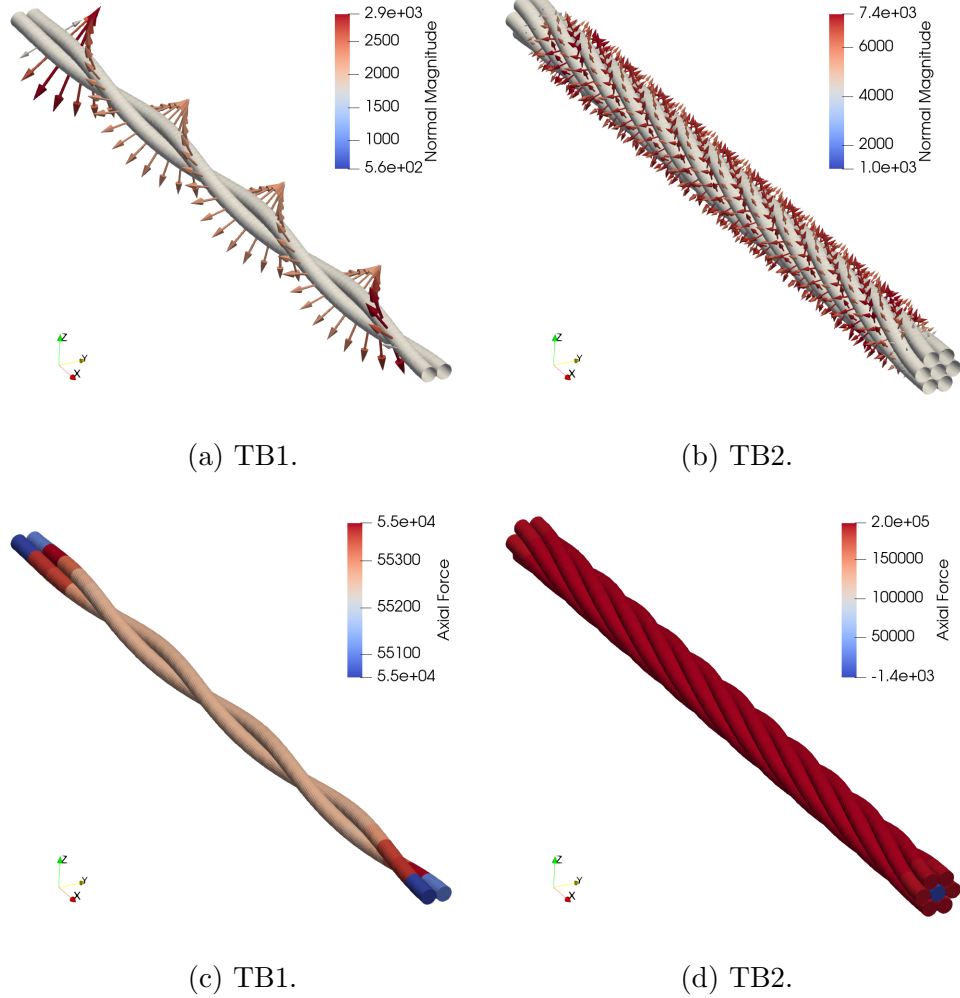


Figure 53: Twisting beams example final configuration normal contact forces [3] and internal axial forces.

the beam elements in gray.

The initial configuration is illustrated in Figure 58. The example is defined by a beam AB that is 3 *m* long and a beam CD that is 1.5 *m* long, both with a radius of 0.1 *m*. The beams are in the *xy* plane with the same middle point *x* coordinate middle and a *y* gap of 0.2 *m*. In beam CD, displacements and rotations are fixed at both ends. The simulation consists of imposing a displacement  $u_y = 0.5$  *m* in the middle of AB to induce contact with CD. This simulation is performed in a quasi-statically with a duration of 1 *s*. Time is used only to gradually impose the displacements. A material of Young’s Modulus  $E = 2E9$  *N/m2* and Poisson ratio  $\nu = 0.3$  is adopted.

Two simulations are analyzed in this example. The former simulation (PB1) objective is to compare the proposed formulation with the results presented in [25]. The latter simulation (PB2) objective is to increase the problem complexity by introducing frictional

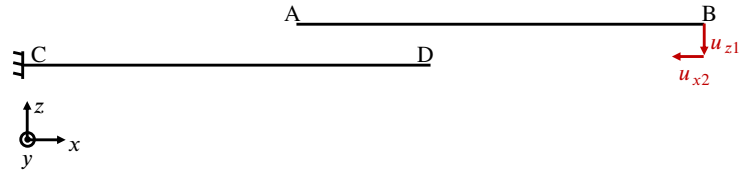


Figure 54: Parallel beams sliding simulation setup [3].

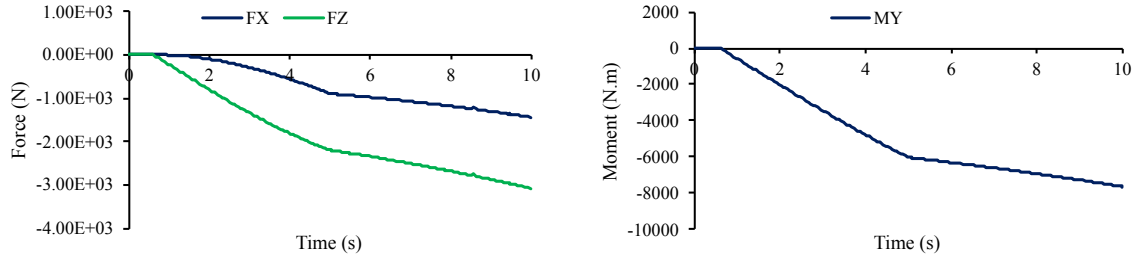
(a) Reaction forces  $x$  and  $z$ .(b) Reaction moment  $y$ .

Figure 55: Reaction forces and moment at point E [3].

contact interaction. A linear normal penalty parameter of  $1E7$   $N/m$  is adopted for PB1 and PB2. A tangential penalty of  $1E6$   $N/m$  with frictional coefficient  $\mu_s = 0.3$  is adopted for PB2.

Figure 60a presents the  $y$  reaction forces at point E for PB1 in red, for PB2 in red marks, and the reactions from [25] in red. It is possible to note in this figure that the results from PB1 and from [25] are almost identical until approximately 7 s. After that, the spline-based contact formulation presents slightly higher reaction values. Moreover, Figure 59 illustrates the final configuration obtained for simulation PB1 and as presented in [25]. This figure shows that both final configurations are similar, though more reaction forces are observed in PB1. These results indicate that the higher stiffness observed in PB1 is associated with more contact pairs. The number of contact pairs becomes particularly relevant in high-penetration scenarios.

The axial internal force in the middle element of beam AB analyzes the friction effects in this simulation. Figure 60b presents the axial internal forces evolution for both simulations, PB1 and PB2. Figure 60c presents the  $y$  direction displacement difference between simulations PB1 and PB2 at the middle node of AB. These results show that friction substantially increases the middle element compression. Moreover, it shows that friction reduces beam penetrations resulting in a final higher compression in the middle of beam AB. Figure 61 presents the normal and frictional contact forces evolution for PB2.



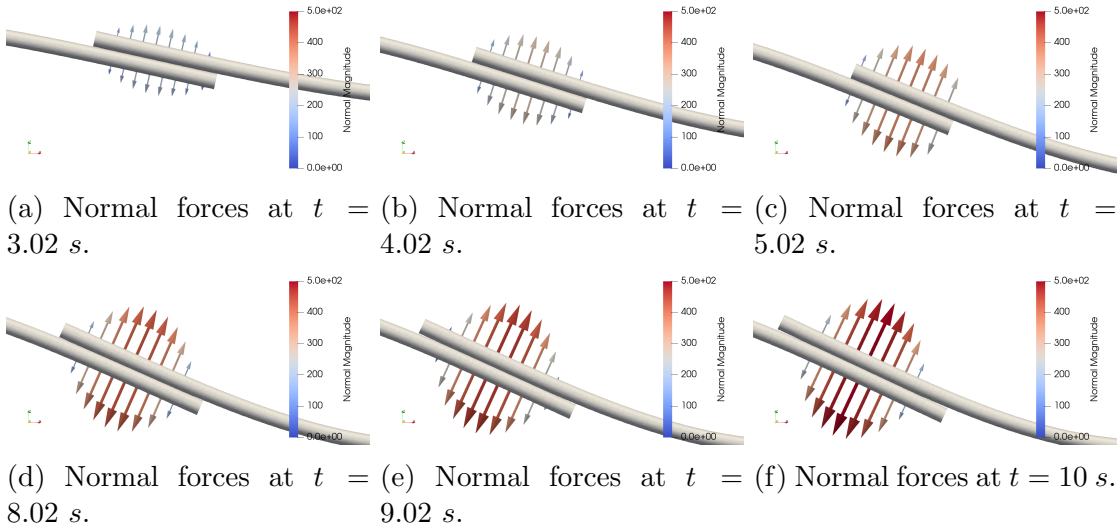


Figure 56: Sliding beams example normal forces [3].

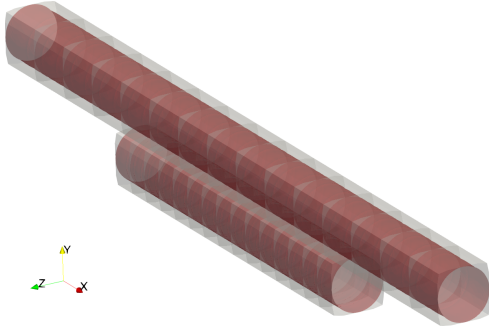


Figure 57: Parallel beams example. Contact elements in red and beam elements in gray [3].

### 5.2.4 Rotating Beam

In this example, the proposed numerical strategy is tested in a problem where the local contact problem should automatically switch between degenerated and non-degenerated formulations, therefore changing from non-conformal/conformal contact, and vice-versa.

The example setup is presented in Figure 62. In this example, beams AB and CD are composed of 15 elements with a total length of  $3m$  and a radius of  $0.06m$ . These beams are orthogonally oriented such that their projection intersection in the  $xy$  plane is at  $2.5m$  from points A and C. Their centerlines are separated in the  $z$  direction by a  $0.3m$  gap. The beam AB presents one end clamped (point A) and the other end (point B) constrained for  $y$  direction displacements. In beam BC, the displacements are imposed in point C while point D is set free.

The simulation is performed in two quasi-static solution-steps. In the first solution-step contact is induced in two initially perpendicular beams. After, in the second solution-step, one beam rotates on the top of another including conformal contact scenarios. The

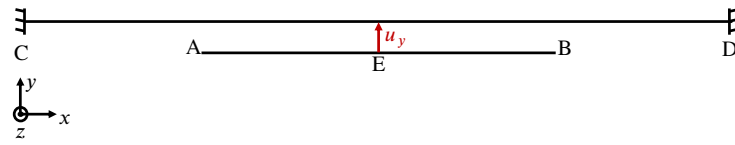
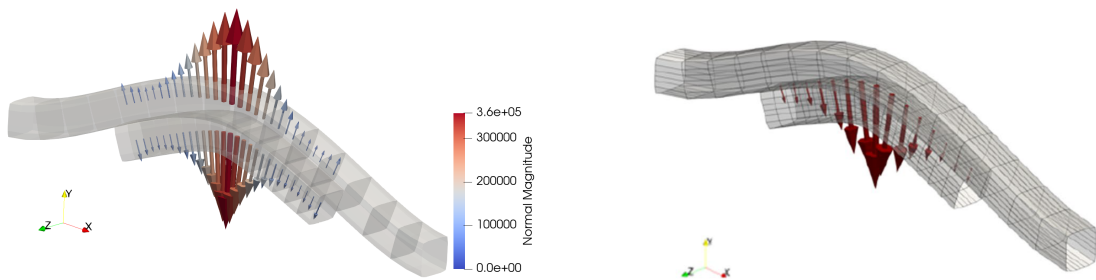


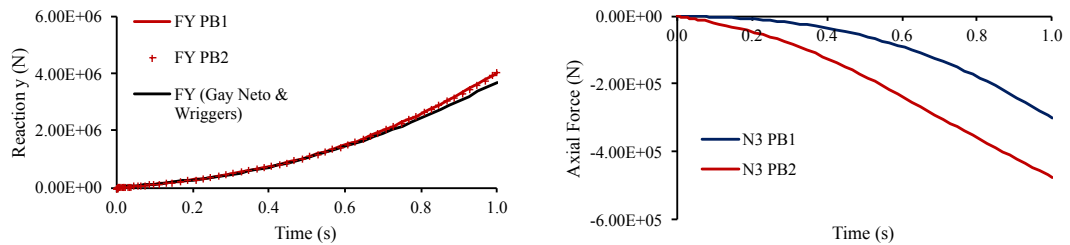
Figure 58: Parallel beams simulation setup [3].



(a) Simulation PB1.

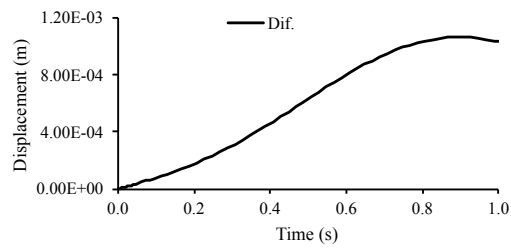
(b) Extracted from [25].

Figure 59: Parallel beams example final configuration [3].



(a) Reaction forces  $y$  at point E for PB1 in blue and extracted from [25] in red.

(b) Axial internal forces in the middle beam element of AB for PB1 in blue and for PB2 in red.



(c) Displacement difference between PB1 and PB2 in the middle node of AB.

Figure 60: Parallel beams example results [3].

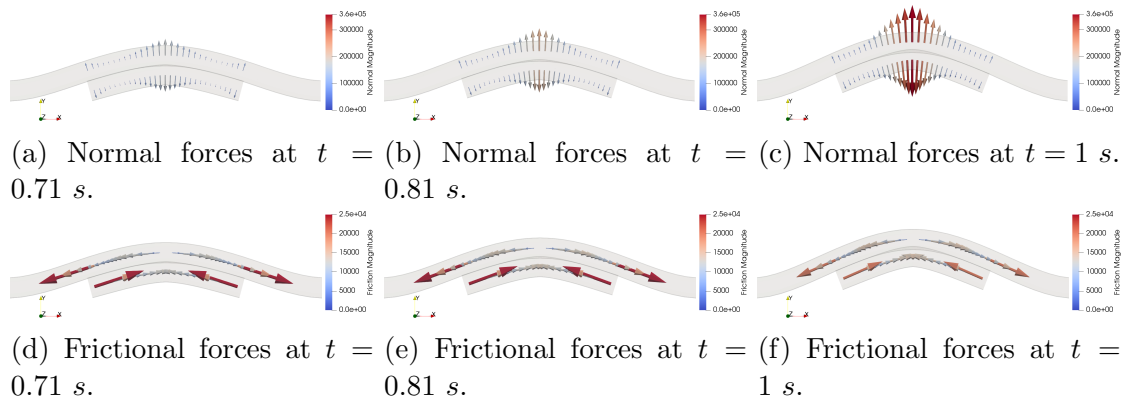


Figure 61: Parallel beams simulation PB2 normal and frictional forces [3].

simulation displacements are detailed in Table 9. The time parameter is used only to gradually impose the displacements. In this example, a material with Young's Modulus  $2E9 \text{ N/m}^2$  and a Poisson ratio of  $\nu = 0.3$  is considered. Moreover, a linear normal penalty parameter of  $1E6 \text{ N/m}$  is adopted.

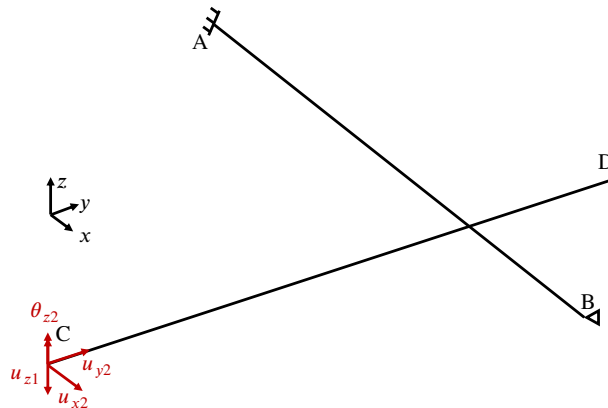


Figure 62: Rotating beams example simulation setup [3].

Displacements	
Displ. 1 <sup>st</sup> solution-step (m)	$u_{y1} = 0.4t$
Duration 1 <sup>st</sup> solution-step (s)	1
Displ. 2 <sup>nd</sup> solution-step (m,rad)	$u_{x2} = -2.5\cos\left(\frac{\pi(t-1)}{19} + \frac{\pi}{2}\right)$ $u_{y2} = 2.5\sin\left(\frac{\pi(t-1)}{19} + \frac{3\pi}{2}\right) + 2.5$ $\theta_z = \frac{\pi(t-1)}{19}$
Duration 2 <sup>nd</sup> solution-step (s)	19

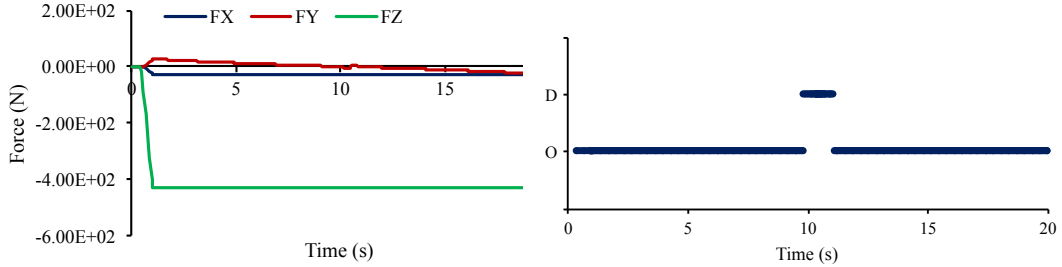
Table 9: Rotating beam example displacements data.

Figure 63a presents the reaction forces at point C. These results show that the  $z$  and  $x$  reactions stay constant during the beam rotation. Moreover, the  $y$  reaction symmetrically changes, as expected, due to the beam rotation. The contact formulation status during the simulation is presented in Figure 63b with “O” indicating an original LCP and “D”

a degenerated LCP. This figure shows that from 10.4 s to 11.11 s there are degenerated contact pairs effectively involved in the simulation as beams become aligned.

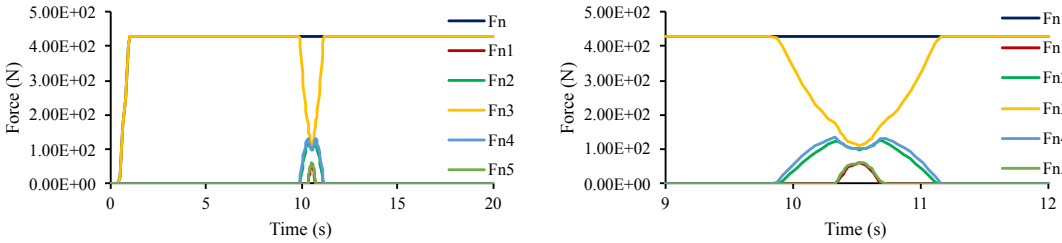
Figure 63c presents the normal contact forces acting in beam CD. In this figure, the total normal contact force is indicated as  $F_n$  while other contact forces are indicated as  $F_{n1}$  to  $F_{n5}$ . This figure shows that the total normal contact force remains constant during the whole beam rotation. In fact, the total normal contact force  $F_n$  is equal to  $F_{n3}$  in the major part of the simulation where there is no degeneration. However, when degeneration takes place, the total normal contact force  $F_n$  splits into five contact forces,  $F_{n1}$  to  $F_{n5}$ . It is noteworthy that the splitting process does not occur instantaneously, but gradually by introducing and removing contact forces according to simulation evolution. Figure 63d presents in detail the normal contact forces splitting from 9 s to 12 s. Figure 67 shows the normal contact forces evolution in several configurations.

The results in Figure 63 prove that the proposed numerical strategy is consistent in going back and forth between non-degenerated and degenerated formulations. Moreover, it could maintain the total contact force even considering the challenging transitions to conformal contact scenarios.



(a) Reaction forces at point C.

(b) LCP status with “O” as original and “D” as degenerated.



(c) Total normal contact force in beam CD. (d) Detailed view of the total normal contact force.

Figure 63: Rotating beam example results [3].

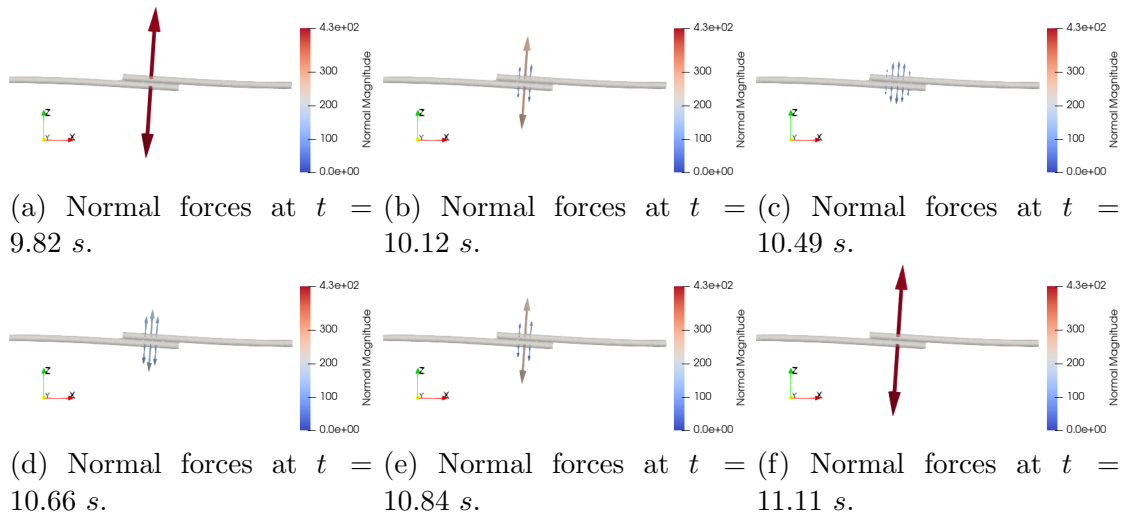


Figure 64: Rotating beam example normal forces [3].

### 5.2.5 Beam Rotating on Arc

The objective of this example is again to explore a scenario where automatic degeneration is necessary. In this example, which is based on [47], orthogonal contact of a straight beam and an arc is initially imposed. After that, rotations are defined at beam ends inducing conformal contact scenarios.

Figure 65 illustrates the simulation setup. The simulation is defined by a beam AB that is composed of seven elements with length 2 and radius of 0.01, and an arc composed of 31 beam elements and radius 0.01. The arc is in fact discretized with straight beam elements and smooth contact elements due to the spline-based formulation. The arc radius is one.

The beam and the arc are initially orthogonally oriented in a just-touch configuration. To impose the displacements a rigid node set is defined at point C to control the displacements of points A and B. Point C is initially defined as the middle point of beam AB. The arc is clamped at both ends (points D and E) with  $z$  displacements fixed along the whole length.

The simulation is divided into two quasi-static solution-steps. In the first solution-step a displacement  $u_y = 0.28$  is imposed at point C in 10 s. After that, in the second solution-step, a full rotation  $\theta_z = 2\pi$  is imposed at point C in 10 s. Time is used only to gradually impose the displacements. A material with Young's Modulus  $1E9$  and Poisson ratio  $\nu = 0.3$  is adopted. Moreover, an axial stiffness reduction factor of 100 ( $0.01 EA$ ) is adopted for beam AB as in [47].

Two simulations are proposed for this example. The former simulation (RA1) objective is to compare the proposed formulation with the results presented in [47]. In this case, only normal contact interaction is considered with a normal penalty parameter of  $1E5$ . In the latter simulation (RA2), however, normal and frictional contact interactions are considered. For simulations RA2 a normal penalty parameter  $1E5$  is also considered with a tangential penalty parameter  $1E4$  and a frictional coefficient  $\mu_s = 0.3$ .

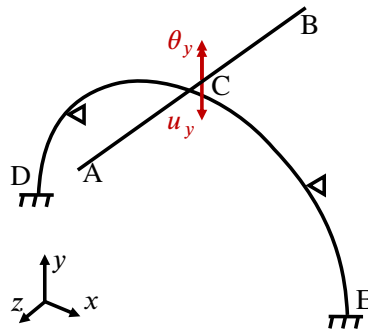
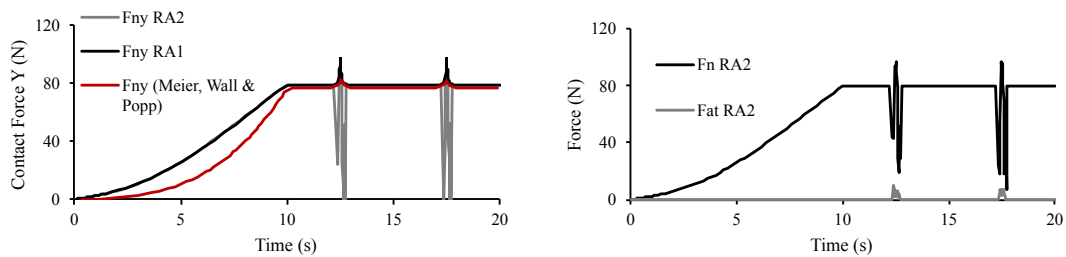


Figure 65: Beam rotating on arc simulation setup [3].



(a) Contact forces in  $y$  direction. Black line for RA1, gray line for RA2, and red line and frictional force (Fat) for RA2. adapted from [47]. (b) Magnitude of normal contact force (Fn) for RA2.

Figure 66: Beam rotating on arc results [3].

Figure 66a presents the contact forces in the  $y$  direction for RA1 and RA2 respectively in black and gray, and the results adapted from [47]. This figure shows, from 0 s to 10 s, a clear gap between the spline-based contact formulation (RA1 and RA2) and the formulation proposed by [47]. This gap, however, gradually reduces up to very similar final contact forces for all three simulations at 10 s. This difference is likely to be associated with the contact interface law that is nonlinear in [47] and linear in simulations RA1 and RA2.

From 10 s to 20 s, all models present similar reactions with peaks around 12.5 s and 17.5 s. These instants represent singular conformal contact configurations where the beam is exactly aligned with the arc. The peak values in Figure 66a can be interpreted as a “snap-through” phenomenon as also observed in [47]. Moreover, the results from

RA2 indicate that friction may play a critical role during the “snap-through” phase. It is possible to observe in Figure 66a that friction drastically affects the normal reaction while peak values are kept.

Figure 66b shows the magnitude of the normal contact force ( $F_n$ ) and the frictional force ( $F_{at}$ ) for RA2. It is possible to observe in this figure that the normal contact force is reduced but does not vanish in frictional contact scenarios. Figure 67 illustrates several configurations around the “snap-through” stage of RA2.

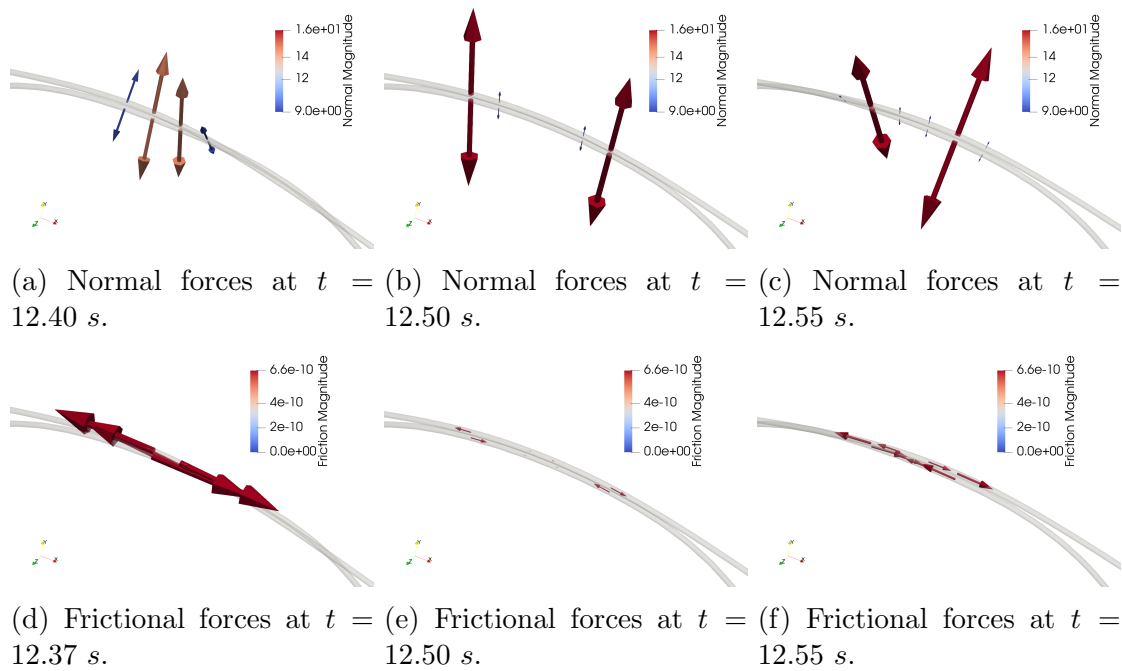


Figure 67: Beam rotating on arc contact forces for RA2 [3].

## 6 TEXTILE APPLICATIONS

This chapter is particularly dedicated to numerical examples involving textile applications [2]. The last example recovers a study for the biaxial tension behavior of textiles presented in [68] including now the spline-based contact formulation results. This study served as a great motivation for the spline-based contact formulation developed.

### 6.1 Knot Tighten

In this example, the proposed formulation is applied in a self-contact scenario. The tightening of a knot is analyzed based on the procedure presented in [35]. This simulation is performed as a static simulation with three solution-steps using three distinct displacement fields. The time presented in each solution-step is used only to impose the displacements gradually. Figure 68 illustrates the considered displacement fields. The objective of the first displacement field is to bend the beam into a “heart shape”. The second displacement aims to slightly tighten the knot. Finally, with the last prescribed displacement, the tips are pulled and the knot is effectively tightened.

In this simulation, a material with  $E = 1E6 \text{ N/m}^2$  and Poisson ratio  $\nu = 0.3$  is considered. The beam is composed of 40 elements with a radius of  $0.15 \text{ m}$  and a length of  $40 \text{ m}$ . Points A and B are fixed during the whole simulation and are initially located respectively at  $(0, 0, 0) \text{ m}$  and  $(0, 0, 40) \text{ m}$ . Points C and D are initially located respectively at  $(0, 0, 15) \text{ m}$  and  $(0, 0, 25) \text{ m}$ . Additionally, a constraint is added to the model at the beginning of the second prescribed displacement field at points C and D. The objective of this constraint is to fix the “ $x$ ” displacement at points C and D to avoid rotations during the knot tightening. To induce self-contact the beam model is divided into two equal parts. These parts are then joined by a special constraint that imposes the same displacements and rotations employing Lagrange multipliers, see e.g. [81]. The simulation data are detailed in Table 10. This simulation is performed in a static framework with an



Table 10: Knot tighten example simulation data.

Simulation data				
Displ. 1 <sup>st</sup> solution-step (m)	$u_{x1} = 0.3$	$u_{y1} = 15$	$u_{z1} = 22$	$\theta_{x1} = 1.5\pi$
and simulation time (s)	5			
Displ. 2 <sup>nd</sup> solution-step (m)	$u_{x2} = 3.5$	$\theta_{z2} = 0.5\pi$		
and simulation time (s)	3			
Displ. 3 <sup>rd</sup> solution-step (m)	$u_{x3} = 9$			
and simulation time (s)	7			

adaptative time-step ranging from  $1E-4$  s to  $5E-1$  s. The following contact parameters are adopted, normal interface law parameter  $\epsilon_{e1} = 1E6$  N/m, and normal interface law parameter  $\epsilon_{e2} = 1$ .

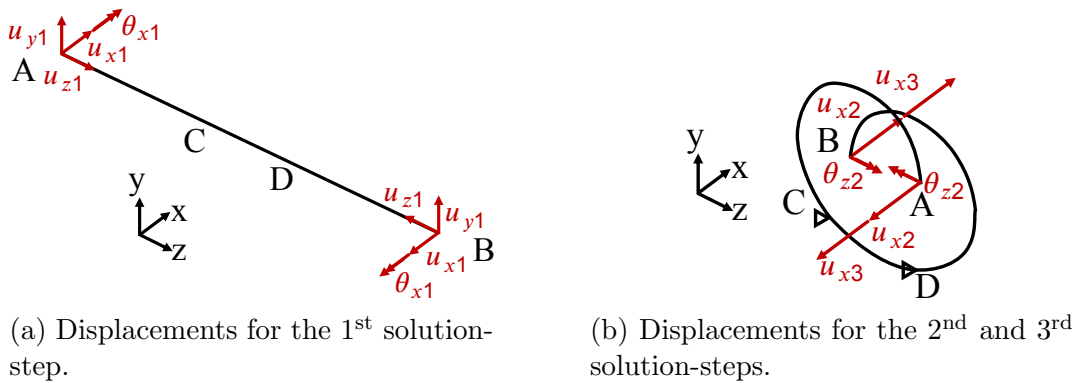


Figure 68: Representation of knot tightening model example with prescribed displacements [2].

The reaction force components at point A for the “SP” and the “SS” contact models are depicted in Figure 69. From 0 s to 5 s only the “z” direction force is relevant since the heart shape is being formed. After that, from 5 s to 8 s, when the knot starts the tightening process, the “x” force increases with the first beam contact appearing at 7 s as shown in Figure 70. Finally, when the knot is effectively tightened, the magnitude of the “x” force drastically increases while the “y” reduces since the tip moves away from the knot’s center. Figure 69 shows that both contact models present almost the same result until approximately 7s when the “SS” model finally diverges. The simulation underlines that the proposed formulation is robust and can handle smoothly challenging scenarios such as the simultaneous sliding of contact elements present in the knot tightening modeling. Figure 71 depicts several instants of this simulation.

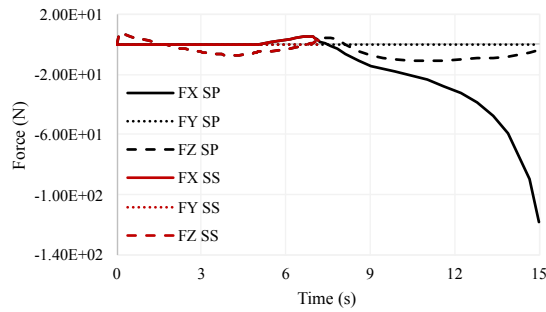


Figure 69: Reactions force components at point A obtained in the knot tightening contact example [2].



Figure 70: First contact instant at 7 s in the knot tightening contact example [2].

## 6.2 Textile Shear

The application of the proposed formulation to a problem with multiple contacts with friction and a nonlinear normal interface law is the subject of this example. The “SS” contact model is not adopted in this example since the nonlinear normal interface law as considered in this work is not available in this formulation. A square plain textile sample with 20 yarns (10 in each direction) is defined. The sample is subjected to a shear simulation that reproduces an experimental test known as picture-frame [82]. The picture-frame test consists of a rigid square trellis frame where a diagonal displacement is imposed leading to shear in the textile. The objective of the picture-frame test lies in the characterization of yarn’s rotation (shear angle) with respect to the applied shear force.

The experimental apparatus is modeled by four rigid body elements connecting the yarn’s tips on each side of the square sample [83]. Additionally, a pilot node for each rigid body is defined in the corner of the square sample. The pilot node controls the rigid body motion and, as a consequence, the yarns’ tip displacement [80]. Figure 72a and Figure 72b illustrate the textile model and the displacement field imposed on the pilot nodes. Two pilot nodes are defined in each point A and B. The pilot nodes in point A have the same displacement  $u_x$  and  $u_y$ , but opposite rotations  $\theta_z$  to reproduce the

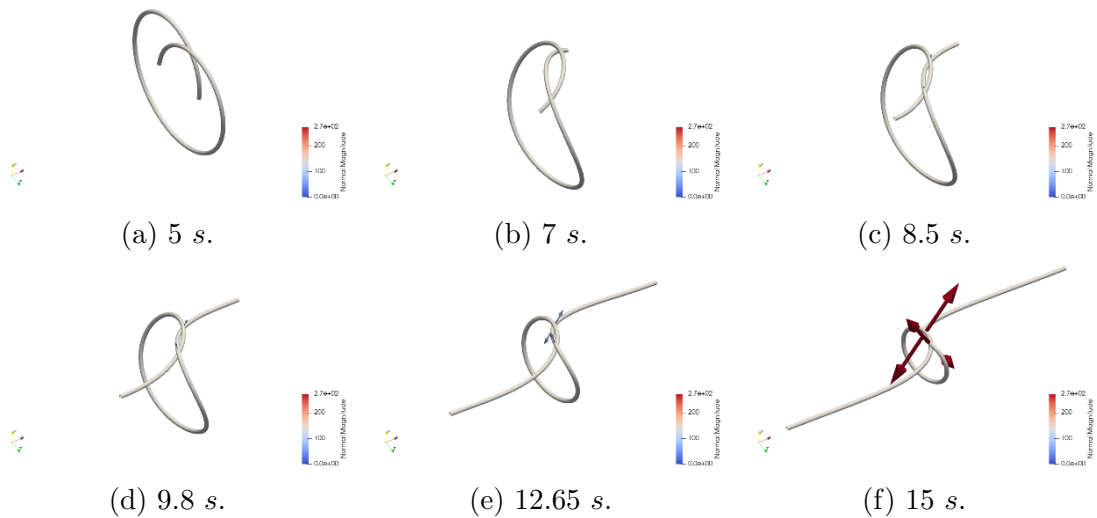


Figure 71: Normal contact forces at several instants in the knot tightening example [2].

Table 11: Textile shear example simulation data.

Simulation data			
Displacement (mm, rad) and simulation time (s)	$u_x = 2.63802$	$u_y = 2.63802$	$\theta_z = 0.32$
	1.6		

picture-frame experiment. An analogous idea is applied to both nodes in point B.

In this simulation, a material with tensile stiffness of  $38000\text{ N}$ , Poisson ratio of  $\nu = 0.2$ , and specific mass of  $2540\text{ kg/m}^3$  is considered. Moreover, each yarn is composed of 52 beam elements with a radius of  $0.2\text{ mm}$ . The yarns' centerlines in-plane “ $xy$ ” length is  $20\text{ mm}$  with a spacing of  $1.6\text{ mm}$ . The out-of-plane “ $z$ ” spacing between yarns' surfaces is  $0.02\text{ mm}$ . Point A and B are respectively located at  $(0, 0, 0)\text{ mm}$  and  $(20, 20, 0)\text{ mm}$ . The textile geometry and material data are based on the plain weave presented in [68], however, adapted here to a circular cross-section. The normal nonlinear interface law is based on the yarn's crushing law presented in [55], which was obtained through a 3D FEM simulation. Figure 11 illustrates the normal contact interface law adopted as a dotted line and the interface law extracted from [55] as a solid line. The proposed simulation is performed in a single dynamic solution-step. The simulation data are detailed in Table 11. This simulation is performed in a dynamic framework with Newmark parameters  $\beta = 0.3$  and  $\gamma = 0.5$  (see [79]) with an adaptative time-step ranging from  $1E-4\text{ s}$  to  $1E-1\text{ s}$ . Moreover, the following contact parameters are considered, normal interface law parameter  $\epsilon_{e1} = 4E6\text{ N/m}^2.613$ , normal interface law parameter  $\epsilon_{e2} = 2.613$ , static and dynamic frictional coefficients  $\mu_s = \mu_d = 0.1$ , and frictional penalty parameter  $\epsilon_{te} = 1E1$ .

Figure 73a shows the textile configuration at the end of the simulation. The final textile configuration with multiple normal contact forces and frictional contact forces are

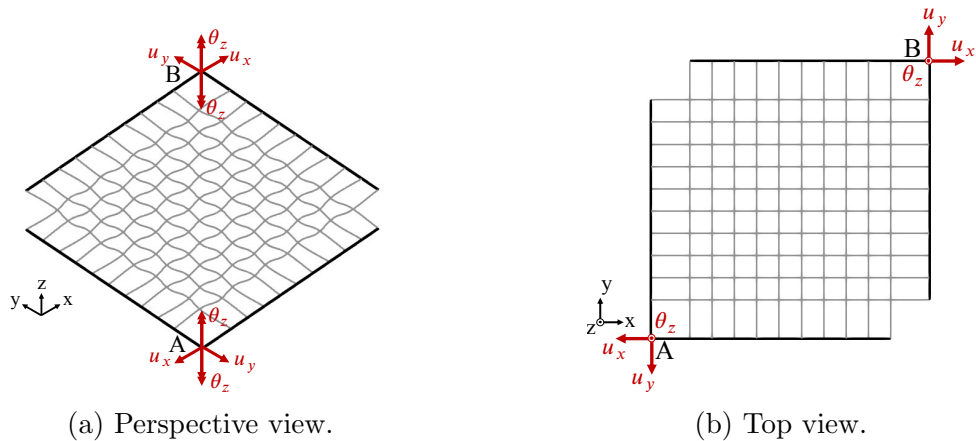


Figure 72: Representation of textile shear model example with prescribed displacements [2].

presented in Figure 73b and Figure 73c. The results demonstrate that the spline-based formulation can handle multiple contacts including a nonlinear normal interface law and friction.

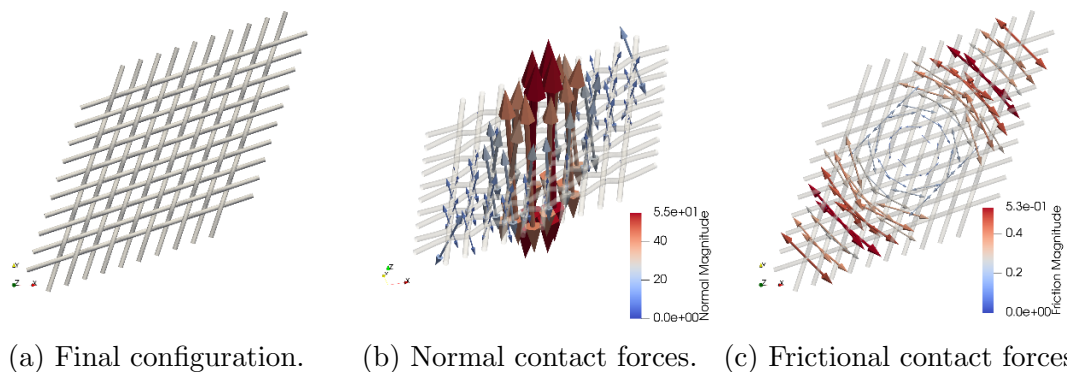


Figure 73: Model results obtained at the end of the textile shear example simulation [2].

The relationship between the shear angle and the normalized shear force is presented in Figure 74. The shear angle  $\gamma$  is defined as  $\gamma = 90 - 2\theta$ , where  $2\theta$  is the current angle formed by the rigid elements at point A or B during the simulation [82]. The shear force  $F_s$  is calculated based on the pulling force  $F$  and the frame configuration  $\theta$  as  $F_s = F/(2\cos(\theta))$  [82]. The normalized shear force  $F_s \text{ norm}$  is simply defined, considering the frame's length equals to the fabric's length sample, as  $F_s \text{ norm} = F_s/L_{frame}$ . While it is not the objective of this example to develop a deep analysis of the textile shear mechanics, the results of Figure 69 show a good qualitative response when compared to the experimental results presented in [82] for shear angles above  $25^\circ$ .

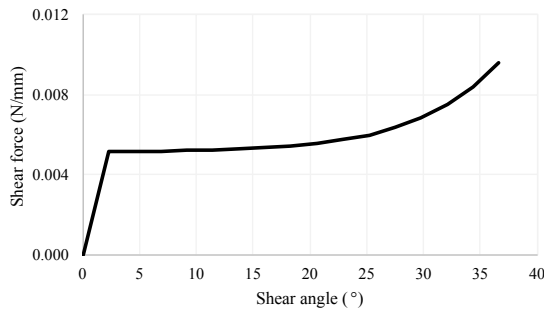


Figure 74: Shear angle response with respect to the normalized shear force applied [2].

### 6.3 Biaxial Tension

The objective of this example is to reproduce the results for the biaxial tension modeling of a plain woven glass fabric presented in [1]. In that work a surface-to-surface contact formulation is combined with a geometrically-exact beam model, both with elliptical cross-sections, to reproduce biaxial tension experimental results from [7]. In this example, however, a circular cross-section is adopted according to the spline-based contact formulation while the same elliptical cross-section is considered for the beam model. A similar strategy is adopted in example 5.2.3.

The biaxial tension experiment consists of simultaneously imposing displacements in both main textile directions (warp and weft) while forces are measured. The ratio between strains is defined as  $k = \varepsilon_{warp} / \varepsilon_{weft}$ , where  $\varepsilon_{warp}$  and  $\varepsilon_{weft}$  are, respectively, the strains in the warp “ $x$ ” and the weft “ $y$ ” directions. The biaxial tension simulation setup is illustrated in Figure 75.

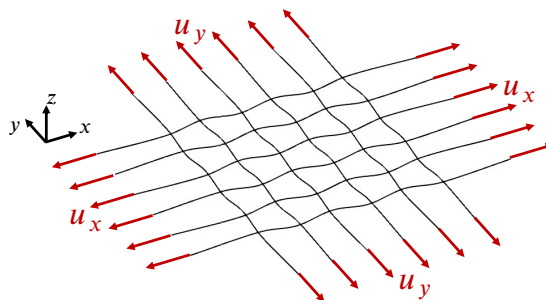


Figure 75: Biaxial tension model setup.

The complete geometric characterization of the beam model is presented in [1] and combines a pre-processor with the well-established software for textile modeling TexGen<sup>®</sup> [77]. In this example, a glass fabric with tensile stiffness ( $EA$ ) of 38000  $N$ , a Poisson ratio of 0.2, and a specific mass of 2540  $kg/m^3$  is considered. The ellipsoidal beam semi-major axis is 1.136364  $mm$  and the semi-minor axis is 0.2840909  $mm$ . For the spline-based

contact surface, the ellipsoidal semi-minor axis is taken as the radius. A bending stiffness reduction factor of  $10^{-1}$  is adopted to reduce the lower moment of inertia. This reduction factor is assumed with the objective of reproducing the almost null bending stiffness of real textiles. The simulations are dynamically performed with Newmark parameters  $\beta = 0.3$  and  $\gamma = 0.5$  [79]. A linear normal penalty parameter of  $3.5E5 \text{ N/m}$  is adopted in [1], though normal penalty parameters  $\epsilon_1 = 1.5E6 \text{ N/m}$  and  $\epsilon_2 = 1$  are adopted in this work. Friction is not considered in this example. The textile sample is composed of six yarns in each direction with an in-plane length of  $40.90909 \text{ mm}$ , an in-plane spacing between yarns of  $4.54545 \text{ mm}$ , and an out-of-plane spacing between yarns surfaces of  $0.11364 \text{ mm}$ . Fixed displacements and free rotations are adopted as boundary conditions for all yarns in this example. Figure 76 illustrates the beam model in gray and the spline-based contact surface in red.

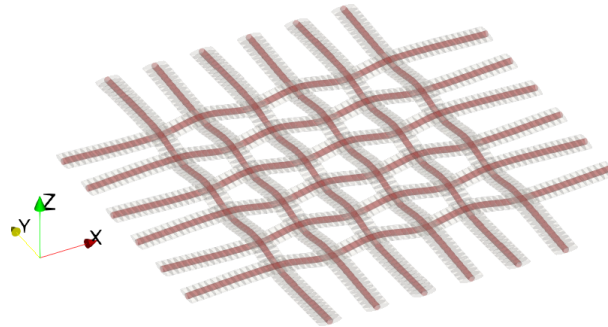


Figure 76: Biaxial tension models. Spline-based contact surface in red and structural beam model rendered in gray.

The results for  $k = 1$ ,  $k = 2$ , and  $k = 0.5$  as experimentally obtained in [7], modeled with surface-to-surface contact as in [1], and calculated with the spline-based contact formulation are presented. Figure 77a shows that the results from “Surface” and “Spline” are almost identical, though shifted from the experimental result. This shift is, however, caused by the gap adopted between contact surfaces to avoid initial overlapping [1]. Figures 77b and 77c show, however, significant differences between the results from “Surface” and “Spline”. These results highlight the spline-based contact formulation feature of smoothing kinks formed by straight beam elements. The smoothing of beam elements kinks leads to slight differences in yarns’ curvature that become more relevant when  $k \neq 1$ . It is possible however to consider the spline-based contact formulation results qualitatively good, in particular when compared to the experimental results.

Figure 78 presents normal contact forces obtained from the biaxial tension simulation in [1] and from the spline-based contact formulation. It is possible to note that a single contact force is present in each yarn’s contact region instead of multiple forces in [84]. In

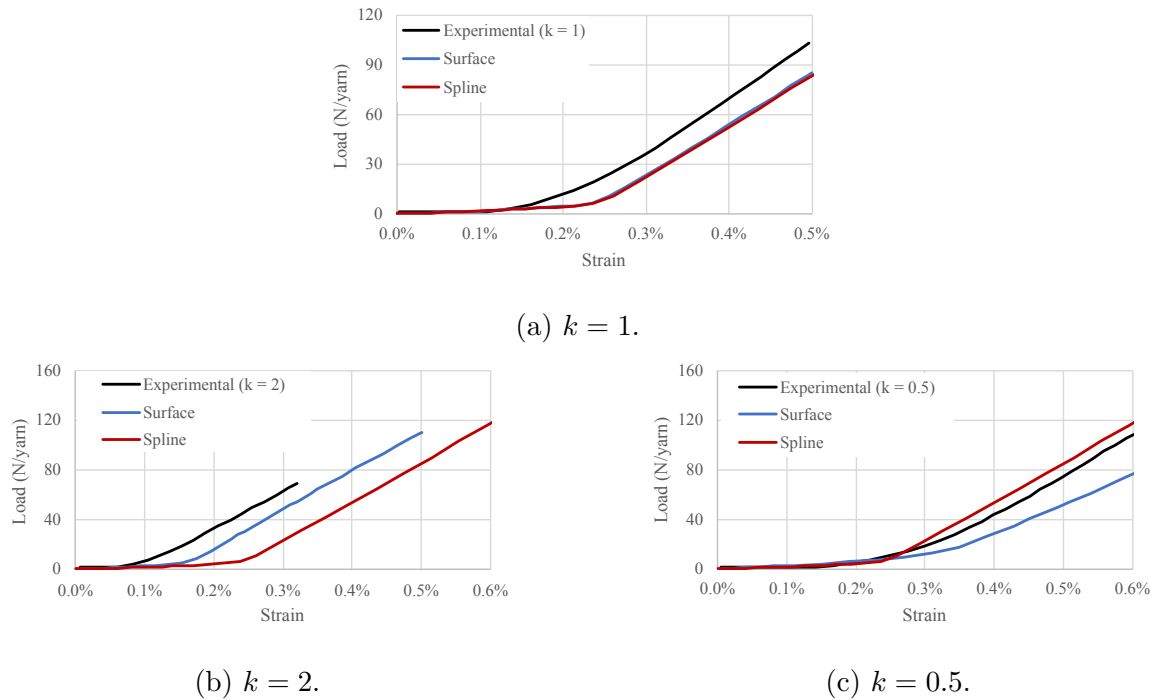
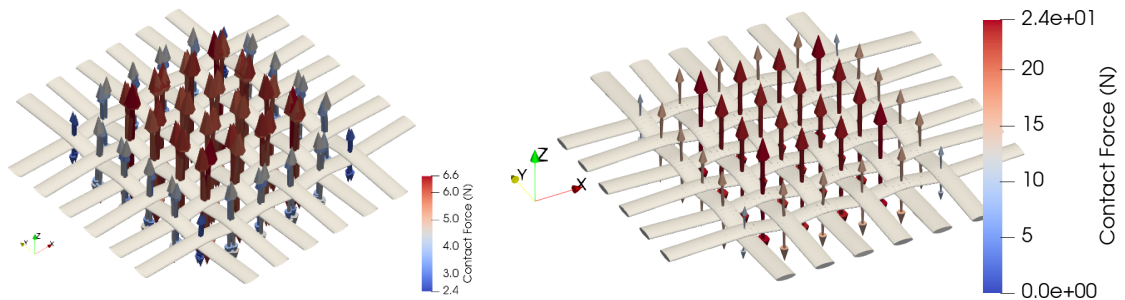


Figure 77: Biaxial tension results, “Experimental” in black from [7], “Surface” in blue from [1], and “Spline” in red from the spline-based contact formulation.

the surface-to-surface formulation, each contact element is described as smooth surfaces based on superellipse cross-sections, though only  $C^0$  continuity is granted at their interfaces. In the spline-based formulation, however, the contact surface is smoothly described as a whole with  $C^1$  continuity and circular cross-section. These different geometric descriptions certainly play a role in contact interaction. Another important aspect of this simulation is the normal linear penalty coefficients considered. In the spline-based contact formulation, a higher linear penalty is considered since multiple contact pairs become single-contact interactions. In this example, single-contact interactions may be seen as an advantage since they allow the use of particular nonlinear interface laws experimentally obtained.



(a) Surface-to-surface contact formulation. Extracted from [1].

(b) Spline-based contact formulation.

Figure 78: Normal contact forces obtained from the biaxial modeling of a glass fabric plain weave for  $k = 1$ .



## 7 CONCLUSIONS

A spline-based  $C^1$  smooth formulation for beam-to-beam contact to handle conformal and non-conformal contact was developed. The proposed contact formulation seeks to smoothly describe structures as a whole regardless of any particular structural formulation and displacement magnitude. Though the formulation was detailed for  $C^1$  continuity, the ideas presented can be easily expanded to higher-order formulations.

The spline description guarantees continuity not only within the contact elements but for the whole contact surface. Another advantage of the spline-based formulation lies in the simplicity of the geometric description that uses only one convective coordinate to depict the centerline. As a result, the Local Contact Problem (LCP) reduces to a minimization problem. However, the lack of an additional convective coordinate neglects the effects of surface contacts with respect to the centerline. This work assumes a normal and tangential contact formulation including elastic and viscous contributions. A nonlinear interaction law was introduced for normal contact.

The three criteria introduced showed to be reliable in the decision-making regarding an LCP solution. The degeneration procedure of fixing *a priori* one of the convective coordinates regarding the numerical criteria proved to be effective in handling complex contact scenarios. The choice for this procedure highlights the strategy's simplicity while putting into evidence its robustness.

The spline contact model was successfully applied to several problems. In the perpendicular beam example, the proposed formulation was compared to a more complex but well-established surface-to-surface contact formulation. The results of this example showed that the spline contact formulation is accurate for thin beams where the cross-section size is not important. The spline contact formulation was also compared with an alternative smooth contact formulation with sufficiently good results considering the different approaches. The non-conformal numerical examples showed that the strategy is

capable of automatically switching between degenerated and non-degenerated scenarios.

The proposed contact formulation also showed great potential in dry fabrics considering the integration between the Giraffe solver and the TexGen<sup>®</sup> software [77]. The natural spline smooth description is quite desirable in these applications where large deformations are likely to occur. Moreover, the spline-based contact was able to reproduce single-contact interactions when expected. This characteristic is also of particular interest since it permits the use of experimentally obtained interaction laws, even including frictional effects.

## 7.1 Future Works

Some direct extensions of this work would be the increase in the degree of the spline contact elements and the inclusion of rotational degrees of freedom in the spline contact formulation to consider surface moments with respect to beam centerlines.

The main advantage of increasing the degree of the spline elements lies in smoothing the contact interaction due to the spline continuity, depending on the needs of the structure in analysis. Moreover, the contact forces would be distributed to more nodes (control points) according to the spline degree. The drawback of increasing the spline degree is that the spline-based surface is more likely to differ from the actual finite element mesh.

The inclusion of degrees of freedom could be done similarly as proposed in [36, 41], however considering the spline elements description. In [36, 41] a Frenet-Serret description is adopted for the contact formulation. The advantage of this approach is the existence of normal and binormal vectors that enable rotation measurements.

Finally, it is possible to conceive several practical applications of the present work in the textile modeling field. Some possible applications are:

- Adoption of experimental yarns crushing law for the normal contact interaction;
- Adoption of experimental frictional coefficients;
- Modeling of multiple fibers as a single yarn;
- Applications involving 3D fabric modeling;
- Manufacturing of woven composite materials.

## APPENDIX A

Simulation data	Point A	Point B
Displ. 1 <sup>st</sup> solution-step (m) and simulation time (s)	$u_{z1} = 0.5$ 1	
Displ. 2 <sup>nd</sup> solution-step (m) and simulation time (s)	$\theta_{z2} = \frac{\pi}{2}$ $u_{x2} = 2.5 \cos\left(\frac{(t-1)\pi}{2} + \frac{3\pi}{2}\right)$ $u_{y2} = 2.5 + 2.5 \sin\left(\frac{(t-1)\pi}{2} + \frac{3\pi}{2}\right)$ 1	$\theta_{z2} = \frac{\pi}{2}$ $u_{x2} = 2.5 + 2.5 \cos\left(\frac{(t-1)\pi}{2} + \pi\right)$ $u_{y2} = -2.5 \sin\left(\frac{(t-1)\pi}{2} + \pi\right)$
Displ. 3 <sup>rd</sup> solution-step (m) and simulation time (s)	$\theta_{y3} = \frac{\pi}{2}$ $u_{x3} = \sqrt{0.5^2 + 2.5^2} \cos\left(-tg^{-1}\left(\frac{0.2}{2.5}\right) + \frac{t-2\pi}{2}\right) - 2.5$ $u_{z3} = \sqrt{0.5^2 + 2.5^2} \cos\left(-tg^{-1}\left(\frac{0.2}{2.5}\right) + \frac{t-2\pi}{2}\right) + 0.2$ 1	$\theta_{y3} = \frac{\pi}{2}$
Timestep (adapt.) (s)	1E - 4 to 2E - 2	

Table 12: Objectivity test simulation displacements.

## APPENDIX B

This appendix aims to develop the normal contact weak form contribution and the corresponding tangent operator for a contact between two spline elements  $\Gamma_A$  and  $\Gamma_B$ . The weak form contributions and the tangent operator are initially symbolic calculated. After the necessary matrices are explicitly express considering the spline-based contact formulation. The procedure here is similar to the one developed in [5] for surfaces.

### 7.1 Weak Form Contribution

For convenience, a simple linear normal contact law is adopted. Consider now, for this purpose a normal interface law  $\mathbf{f}_n$  defined as

$$\mathbf{f}_n = \epsilon \mathbf{g}_e, \tag{7.1}$$

where  $\epsilon$  is a linear penalty parameter and  $\mathbf{g}_e$  is an effective gap vector associated with  $\Gamma_A$  and  $\Gamma_B$ . The effective gap vector is parallel to the normal direction ( $\mathbf{n} = \mathbf{g}/\|\mathbf{g}\|$ ) with the magnitude of the effective gap, see (3.7). It is possible now to write a normal contact potential  $W_n$  as

$$W_n = \frac{1}{2} \epsilon \mathbf{g}_e \cdot \mathbf{g}_e. \tag{7.2}$$

The normal contact potential  $W_n$  can be then derived with respect to the convective coordinates  $\mathbf{c}$  (see (3.4)) and generalized displacements  $\mathbf{d}$  (see (3.5) and Figure 10) to obtain the normal contact force contribution to the weak form. The normal contact force contribution of a pair of spline elements yields

$$\delta W_n = \epsilon \mathbf{g}_e \cdot \delta \mathbf{g}_e, \tag{7.3}$$

where the symbol  $\delta$  is adopted to indicate the variation of quantities. The variation of the effective gap vector  $\delta \mathbf{g}_e$  can be then expressed as

$$\delta \mathbf{g}_e = \mathbf{g}_{e,c} \delta \mathbf{c} + \mathbf{g}_{e,d} \delta \mathbf{d}, \quad (7.4)$$

where a notation  $\mathbf{p}_{,q} = \partial \mathbf{p} / \partial \mathbf{q}$  is introduced to represent partial derivatives. It is possible now to find a relation between  $\delta \mathbf{c}$  and  $\delta \mathbf{d}$  considering the linearization of the orthogonality conditions, which implies that  $\delta \mathbf{r} = \mathbf{o}_2$  since  $\mathbf{bmr} = \mathbf{o}_2$ . A notation  $\mathbf{o}_m$  is adopted to express zero matrices of order  $m$ . The linearization of the orthogonality conditions can be written as

$$\delta \mathbf{r} = \mathbf{r}_{,c} \delta \mathbf{c} + \mathbf{r}_{,d} \delta \mathbf{d} = \mathbf{o}_2. \quad (7.5)$$

Moreover, the linearization  $\delta \mathbf{r}$  can be rearranged as

$$\mathbf{r}_{,c} \delta \mathbf{c} = -\mathbf{r}_{,d} \delta \mathbf{d} \rightarrow \delta \mathbf{c} = -(\mathbf{r}_{,c})^{-1} \mathbf{r}_{,d} \delta \mathbf{d} \rightarrow \delta \mathbf{c} = \mathbf{D} \delta \mathbf{d}, \quad (7.6)$$

where the operator  $\mathbf{D}$  is introduced. The  $\mathbf{D}$  operator expresses the relation between  $\delta \mathbf{c}$  and  $\delta \mathbf{d}$ . The  $\mathbf{D}$  operator is therefore formally defined as

$$\mathbf{D} = -(\mathbf{r}_{,c})^{-1} \mathbf{r}_{,d}. \quad (7.7)$$

It is possible now to express the linearization of the effective gap vector  $\delta \mathbf{g}_e$  considering the  $\mathbf{D}$  operator as

$$\delta \mathbf{g}_e = (\mathbf{g}_{e,c} \mathbf{D} + \mathbf{g}_{e,d}) \delta \mathbf{d}. \quad (7.8)$$

Finally, the normal contact contribution to the weak form can be expressed by considering only variations with respect to the generalized displacements as

$$\delta W_n = \epsilon \mathbf{g}_e \cdot \left( (\mathbf{g}_{e,c} \mathbf{D} + \mathbf{g}_{e,d}) \delta \mathbf{d} \right). \quad (7.9)$$

## 7.2 Contact Tangent Operator

To obtain the contact tangent operator it is necessary to develop a linearization of the weak form. The linearization of the presented weak form leads to

$$\Delta(\delta W_n) = \delta \mathbf{g}_e \cdot \epsilon \Delta \mathbf{g}_e + \epsilon \Delta(\delta \mathbf{g}_e) \cdot \mathbf{g}_e, \quad (7.10)$$

where the symbol  $\Delta$  is introduced to express variation of quantities. It is possible to note that to calculate this tangent operator it is necessary to develop two more terms,  $\Delta \mathbf{g}_e$  and  $\Delta(\delta \mathbf{g}_e)$ . The  $\Delta \mathbf{g}_e$  term can be directly developed with the same strategy presented in (7.8) as

$$\Delta \mathbf{g}_e = (\mathbf{g}_{e,c} \mathbf{D} + \mathbf{g}_{e,d}) \Delta \mathbf{d}. \quad (7.11)$$

The expansion of  $\Delta(\delta \mathbf{g}_e)$  leads to

$$\Delta(\delta \mathbf{g}_e) = \Delta(\mathbf{g}_{e,c} \delta \mathbf{c} + \mathbf{g}_{e,d} \delta \mathbf{d}) = \Delta(\mathbf{g}_{e,c}) \delta \mathbf{c} + \Delta(\mathbf{g}_{e,d}) \delta \mathbf{d}, \quad (7.12)$$

where the direct linearizations  $\Delta \mathbf{g}_{e,c}$  and  $\Delta \mathbf{g}_{e,d}$ . Again, these linearizations can be developed with the same strategy presented in 7.8. The  $\Delta \mathbf{g}_{e,c}$  term leads to

$$\begin{aligned} \Delta \mathbf{g}_{e,c} &= \mathbf{g}_{e,cc} \Delta \mathbf{c} + \mathbf{g}_{e,cd} \Delta \mathbf{d} \\ \Delta \mathbf{g}_{e,c} &= (\mathbf{g}_{e,cc} \mathbf{D} + \mathbf{g}_{e,cd}) \Delta \mathbf{d}, \end{aligned} \quad (7.13)$$

while the  $\Delta \mathbf{g}_{e,d}$  term leads to

$$\begin{aligned}\Delta \mathbf{g}_{e,\mathbf{d}} &= \mathbf{g}_{e,\mathbf{dc}} \Delta \mathbf{c} + \mathbf{g}_{e,\mathbf{dd}} \Delta \mathbf{d} \\ \Delta \mathbf{g}_{e,\mathbf{d}} &= (\mathbf{g}_{e,\mathbf{dc}} \mathbf{D} + \mathbf{g}_{e,\mathbf{dd}}) \Delta \mathbf{d}.\end{aligned}\tag{7.14}$$

By adopting these expressions, it is possible now to more explicitly rewrite  $\Delta(\delta \mathbf{g}_e)$  as

$$\Delta(\delta \mathbf{g}_e) = \left( (\mathbf{g}_{e,\mathbf{cc}} \mathbf{D} + \mathbf{g}_{e,\mathbf{cd}}) \Delta \mathbf{d} \mathbf{D} + (\mathbf{g}_{e,\mathbf{dc}} \mathbf{D} + \mathbf{g}_{e,\mathbf{dd}}) \Delta \mathbf{d} \right) \delta \mathbf{d}.\tag{7.15}$$

Finally, the contact tangent operator can be now expressed considering only virtual quantities associated with generalized displacements as

$$\begin{aligned}\Delta(\delta W_n) &= (\mathbf{g}_{e,\mathbf{c}} \mathbf{D} + \mathbf{g}_{e,\mathbf{d}}) \delta \mathbf{d} \cdot \epsilon(\mathbf{g}_{e,\mathbf{c}} \mathbf{D} + \mathbf{g}_{e,\mathbf{d}}) \Delta \mathbf{d} \\ &+ \epsilon \left( (\mathbf{g}_{e,\mathbf{cc}} \mathbf{D} + \mathbf{g}_{e,\mathbf{cd}}) \Delta \mathbf{d} \mathbf{D} + (\mathbf{g}_{e,\mathbf{dc}} \mathbf{D} + \mathbf{g}_{e,\mathbf{dd}}) \Delta \mathbf{d} \right) \delta \mathbf{d} \cdot \mathbf{g}_e.\end{aligned}\tag{7.16}$$

### 7.3 Equations

In the matrices presented below  $N_i^A$ ,  $N_{i+1}^A$ , and  $N_{i+2}^A$  are the basis functions associated with  $\mathbf{u}_{AA}$ ,  $\mathbf{u}_{AB}$ ,  $\mathbf{u}_{AC}$  and, similarly,  $N_i^B$ ,  $N_{i+1}^B$ , and  $N_{i+2}^B$  are the basis functions associated with  $\mathbf{u}_{BA}$ ,  $\mathbf{u}_{BB}$ ,  $\mathbf{u}_{BC}$ .

$$\mathbf{g}_{e,\mathbf{c}} = \begin{bmatrix} \mathbf{u}_{AA} N_i^A, \xi_A + \mathbf{u}_{BA} N_{i+1}^A, \xi_A + \mathbf{u}_{CA} N_{i+2}^A, \xi_A \\ -\mathbf{u}_{AB} N_i^B, \xi_B - \mathbf{u}_{BB} N_{i+1}^B, \xi_B - \mathbf{u}_{CB} N_{i+2}^B, \xi_B \end{bmatrix}\tag{7.17}$$

$$\mathbf{g}_{e,\mathbf{d}} = \begin{bmatrix} N_i^A \\ N_{i+1}^A \\ N_{i+2}^A \\ -N_i^B \\ -N_{i+1}^B \\ -N_{i+2}^B \end{bmatrix}\tag{7.18}$$

$$\mathbf{g}_{e,cc} = \begin{bmatrix} \mathbf{u}_{AA}N_{i,\xi_A\xi_A}^A + \mathbf{u}_{BA}N_{i+1,\xi_A\xi_A}^A + \mathbf{u}_{CA}N_{i+2,\xi_A\xi_A}^A & 0 \\ 0 & -\mathbf{u}_{AB}N_{i,\xi_B\xi_B}^B - \mathbf{u}_{BB}N_{i+1,\xi_B\xi_B}^B - \mathbf{u}_{CB}N_{i+2,\xi_B\xi_B}^B \end{bmatrix} \quad (7.19)$$

$$\mathbf{g}_{e,dd} = \mathbf{0}_{6 \times 6} \quad (7.20)$$

$$\mathbf{g}_{e,cd} = \begin{bmatrix} N_{i,\xi_A}^A & N_{i+1,\xi_A}^A & N_{i+2,\xi_A}^A & 0 & 0 & 0 \\ 0 & 0 & 0 & -N_{i,\xi_B}^B & -N_{i+1,\xi_B}^B & -N_{i+2,\xi_B}^B \end{bmatrix} \quad (7.21)$$

$$\mathbf{g}_{e,dc} = \begin{bmatrix} N_{i,\xi_A}^A & 0 \\ N_{i+1,\xi_A}^A & 0 \\ N_{i+2,\xi_A}^A & 0 \\ 0 & -N_{i,\xi_B}^B \\ 0 & -N_{i+1,\xi_B}^B \\ 0 & -N_{i+2,\xi_B}^B \end{bmatrix} \quad (7.22)$$

$$\mathbf{D} = \begin{bmatrix} -\frac{N_{i,\xi_A}^A}{D^A} & -\frac{N_{i+1,\xi_A}^A}{D^A} & -\frac{N_{i+2,\xi_A}^A}{D^A} & 0 & 0 & 0 \\ 0 & 0 & 0 & \frac{N_{i,\xi_B}^B}{D^B} & \frac{N_{i+1,\xi_B}^B}{D^B} & \frac{N_{i+2,\xi_B}^B}{D^B} \end{bmatrix} \quad (7.23)$$

with

$$\begin{aligned} D^A &= \mathbf{u}_{AA}N_{i,\xi_A\xi_A}^A + \mathbf{u}_{BA}N_{i+1,\xi_A\xi_A}^A + \mathbf{u}_{CA}N_{i+2,\xi_A\xi_A}^A \\ D^B &= \mathbf{u}_{AB}N_{i,\xi_B\xi_B}^B + \mathbf{u}_{BB}N_{i+1,\xi_B\xi_B}^B + \mathbf{u}_{CB}N_{i+2,\xi_B\xi_B}^B \end{aligned} \quad (7.24)$$



## REFERENCES

- [1] FACCIO JÚNIOR, Celso Jaco; GAY NETO, Alfredo. Challenges in representing the biaxial mechanical behavior of woven fabrics modeled by beam finite elements with contact. **Composite Structures**, v. 257, p. 113330, fev. 2021. ISSN 02638223. DOI: 10.1016/j.compstruct.2020.113330. Disponível em: <https://linkinghub.elsevier.com/retrieve/pii/S0263822320332566>.
- [2] FACCIO JÚNIOR, Celso Jaco; GAY NETO, Alfredo; WRIGGERS, Peter. Spline-based smooth beam-to-beam contact model. **Computational Mechanics**, mar. 2023. ISSN 0178-7675. DOI: 10.1007/s00466-023-02283-1. Disponível em: <https://link.springer.com/10.1007/s00466-023-02283-1>.
- [3] FACCIO JÚNIOR, Celso Jaco; GAY NETO, Alfredo; WRIGGERS, Peter. Numerical strategy for solving general  $C^1$ -continuous beam-to-beam contact problems (under review). **International Journal for Numerical Methods in Engineering**, 2024.
- [4] GAY NETO, A. "Giraffe user's manual" - generic interface readily accessible for finite elements, p. 1–70, 2020. Disponível em: <http://sites.poli.usp.br/p/alfredo.gay/>.
- [5] GAY NETO, Alfredo; PIMENTA, Paulo Mattos; WRIGGERS, Peter. A master-surface to master-surface formulation for beam to beam contact. Part I: Frictionless interaction. **Computer Methods in Applied Mechanics and Engineering**, Elsevier B.V., v. 303, p. 400–429, 2016. ISSN 00457825. DOI: 10.1016/j.cma.2016.02.005. Disponível em: <http://dx.doi.org/10.1016/j.cma.2016.02.005>.
- [6] GAY NETO, Alfredo; PIMENTA, Paulo Mattos; WRIGGERS, Peter. A master-surface to master-surface formulation for beam to beam contact. Part II: Frictional interaction. **Computer Methods in Applied Mechanics and Engineering**, v. 319, p. 146–174, 2017. ISSN 0045-7825. DOI: <https://doi.org/10.1016/j.cma.2017.01.038>. Disponível em: <https://www.sciencedirect.com/science/article/pii/S0045782516303218>.

- [7] BUET-GAUTIER, K.; BOISSE, P. Experimental analysis and modeling of biaxial mechanical behavior of woven composite reinforcements. **Experimental Mechanics**, v. 41, n. 3, p. 260–269, 2001. ISSN 00144851. DOI: 10.1007/BF02323143.
- [8] JIN, Seungmin; SOHN, Dongwoo; IM, Seyoung. Node-to-node scheme for three-dimensional contact mechanics using polyhedral type variable-node elements. **Computer Methods in Applied Mechanics and Engineering**, v. 304, p. 217–242, jun. 2016. ISSN 00457825. DOI: 10.1016/j.cma.2016.02.019. Disponível em: [jhttps://linkinghub.elsevier.com/retrieve/pii/S0045782516300494](https://linkinghub.elsevier.com/retrieve/pii/S0045782516300494).
- [9] XING, Weiwei et al. A node-to-node scheme for three-dimensional contact problems using the scaled boundary finite element method. **Computer Methods in Applied Mechanics and Engineering**, v. 347, p. 928–956, abr. 2019. ISSN 00457825. DOI: 10.1016/j.cma.2019.01.015. Disponível em: [jhttps://linkinghub.elsevier.com/retrieve/pii/S0045782519300209](https://linkinghub.elsevier.com/retrieve/pii/S0045782519300209).
- [10] WRIGGERS, Peter; RUST, Wilhelm T. A virtual element method for frictional contact including large deformations. **Engineering Computations (Swansea, Wales)**, v. 36, n. 7, p. 2133–2161, 2019. ISSN 02644401. DOI: 10.1108/EC-02-2019-0043.
- [11] PAGGI, Marco; WRIGGERS, Peter. Node-to-segment and node-to-surface interface finite elements for fracture mechanics. **Computer Methods in Applied Mechanics and Engineering**, v. 300, p. 540–560, mar. 2016. ISSN 00457825. DOI: 10.1016/j.cma.2015.11.023. Disponível em: [jhttps://linkinghub.elsevier.com/retrieve/pii/S0045782515003837](https://linkinghub.elsevier.com/retrieve/pii/S0045782515003837).
- [12] KHOEI, Amir R.; BIABANAKI, S. O.R.; PARVANEH, S. M. 3D dynamic modeling of powder forming processes via a simple and efficient node-to-surface contact algorithm. **Applied Mathematical Modelling**, v. 37, n. 1-2, p. 443–462, jan. 2013. ISSN 0307904X. DOI: 10.1016/j.apm.2012.03.010. Disponível em: [jhttps://linkinghub.elsevier.com/retrieve/pii/S0307904X12001485](https://linkinghub.elsevier.com/retrieve/pii/S0307904X12001485).
- [13] CRISFIELD, M. A. Re-visiting the contact patch test. **International Journal for Numerical Methods in Engineering**, v. 48, n. 3, p. 435–449, mai. 2000. ISSN 00295981. DOI: 10.1002/(SICI)1097-0207(20000530)48:3<435::AID-NME891>3.0.CO;2-V. Disponível em: [jhttps://onlinelibrary.wiley.com/doi/10.1002/\(SICI\)1097-0207\(20000530\)48:3%5C%3C435::AID-NME891%5C%3E3.0.CO;2-V](https://onlinelibrary.wiley.com/doi/10.1002/(SICI)1097-0207(20000530)48:3%5C%3C435::AID-NME891%5C%3E3.0.CO;2-V).

- [14] DE LORENZIS, Laura; WRIGGERS, Peter; HUGHES, Thomas J.R. Isogeometric contact: A review. **GAMM Mitteilungen**, v. 37, n. 1, p. 85–123, jul. 2014. ISSN 09367195. DOI: 10.1002/gamm.201410005. Disponível em: [jhttps://onlinelibrary.wiley.com/doi/10.1002/gamm.201410005](https://onlinelibrary.wiley.com/doi/10.1002/gamm.201410005).
- [15] HEINSTEIN, M. W.; LAURSEN, T. A. A three-dimensional surface-to-surface projection algorithm for non-coincident domains. **Communications in Numerical Methods in Engineering**, v. 19, n. 6, p. 421–432, fev. 2003. ISSN 10698299. DOI: 10.1002/cnm.601. Disponível em: [jhttps://onlinelibrary.wiley.com/doi/10.1002/cnm.601](https://onlinelibrary.wiley.com/doi/10.1002/cnm.601).
- [16] ZIMMERMAN, Brandon K.; ATESHIAN, Gerard A. A Surface-to-Surface Finite Element Algorithm for Large Deformation Frictional Contact in febio. **Journal of Biomechanical Engineering**, v. 140, n. 8, ago. 2018. ISSN 15288951. DOI: 10.1115/1.4040497. Disponível em: [jhttps://asmedigitalcollection.asme.org/biomechanical/article/doi/10.1115/1.4040497/425512/A-SurfacettoSurface-Finite-Element-Algorithm-for](https://asmedigitalcollection.asme.org/biomechanical/article/doi/10.1115/1.4040497/425512/A-SurfacettoSurface-Finite-Element-Algorithm-for).
- [17] WRIGGERS, P.; ZAVARISE, G. On contact between three-dimensional beams undergoing large deflections. **Communications in Numerical Methods in Engineering**, v. 13, n. 6, p. 429–438, jun. 1997. ISSN 10698299. DOI: 10.1002/(SICI)1099-0887(199706)13:6<429::AID-CNM70>3.0.CO;2-X. Disponível em: [jhttps://onlinelibrary.wiley.com/doi/10.1002/\(SICI\)1099-0887\(199706\)13:6%5C%3C429::AID-CNM70%5C%3E3.0.CO;2-X](https://onlinelibrary.wiley.com/doi/10.1002/(SICI)1099-0887(199706)13:6%5C%3C429::AID-CNM70%5C%3E3.0.CO;2-X).
- [18] LITEWKA, P.; WRIGGERS, P. Frictional contact between 3D beams. **Computational Mechanics**, v. 28, n. 1, p. 26–39, 2001. ISSN 01787675. DOI: 10.1007/s004660100266.
- [19] HERTZ, Heinrich. Ueber die Berührung fester elastischer Körper. **Journal für die Reine und Angewandte Mathematik**, v. 1882, n. 92, p. 156–171, jan. 1882. ISSN 14355345. DOI: 10.1515/crll.1882.92.156. Disponível em: [jhttps://www.degruyter.com/document/doi/10.1515/crll.1882.92.156/html](https://www.degruyter.com/document/doi/10.1515/crll.1882.92.156/html).
- [20] JOHNSON, K. L. **Contact Mechanics**. [S.l.]: Cambridge University Press, mai. 1989. ISBN 0521347963. DOI: 10.1201/b17588-12. Disponível em: [jhttps://www.cambridge.org/core/product/identifier/9781139171731/type/book](https://www.cambridge.org/core/product/identifier/9781139171731/type/book).
- [21] AL-DOJAYLI, M.; MEGUID, S. A. Accurate modeling of contact using cubic splines. **Finite Elements in Analysis and Design**, v. 38, n. 4, p. 337–352, 2002. ISSN 0168874X. DOI: 10.1016/S0168-874X(01)00088-9.

- [22] KRSTULOVIĆ-OPARA, L.; WRIGGERS, P.; KORELC, J. A  $C^1$ -continuous formulation for 3D finite deformation frictional contact. **Computational Mechanics**, v. 29, n. 1, p. 27–42, 2002. ISSN 01787675. DOI: 10.1007/s00466-002-0317-z.
- [23] LU, Jia. Isogeometric contact analysis: Geometric basis and formulation for frictionless contact. **Computer Methods in Applied Mechanics and Engineering**, Elsevier B.V., v. 200, n. 5-8, p. 726–741, 2011. ISSN 00457825. DOI: 10.1016/j.cma.2010.10.001. Disponível em: <http://dx.doi.org/10.1016/j.cma.2010.10.001>.
- [24] MAGLIULO, M.; ZILIAN, A.; BEEEX, L. A.A. Contact between shear-deformable beams with elliptical cross sections. **Acta Mechanica**, Springer Vienna, v. 231, n. 1, p. 273–291, 2020. ISSN 16196937. DOI: 10.1007/s00707-019-02520-w.
- [25] GAY NETO, Alfredo; WRIGGERS, Peter. Computing pointwise contact between bodies: a class of formulations based on master–master approach. **Computational Mechanics**, Springer Berlin Heidelberg, v. 64, n. 3, p. 585–609, 2019. ISSN 14320924. DOI: 10.1007/s00466-019-01680-9. Disponível em: <https://doi.org/10.1007/s00466-019-01680-9>.
- [26] MAGLIULO, Marco et al. Non-localised contact between beams with circular and elliptical cross-sections. **Computational Mechanics**, v. 65, n. 5, p. 1247–1266, mai. 2020. ISSN 14320924. DOI: 10.1007/s00466-020-01817-1. Disponível em: <https://link.springer.com/10.1007/s00466-020-01817-1>.
- [27] GAY NETO, Alfredo; WRIGGERS, Peter. Master-master frictional contact and applications for beam-shell interaction. **Computational Mechanics**, Springer Berlin Heidelberg, v. 66, n. 6, p. 1213–1235, 2020. ISSN 14320924. DOI: 10.1007/s00466-020-01890-6. Disponível em: <https://doi.org/10.1007/s00466-020-01890-6>.
- [28] NETO, Alfredo Gay; WRIGGERS, Peter. Discrete element model for general polyhedra. **Computational Particle Mechanics**, v. 9, n. 2, p. 353–380, jun. 2022. ISSN 21964386. DOI: 10.1007/s40571-021-00415-z. Disponível em: <https://link.springer.com/10.1007/s40571-021-00415-z>.
- [29] GAY NETO, Alfredo; WRIGGERS, Peter. Numerical method for solution of pointwise contact between surfaces. **Computer Methods in Applied Mechanics and Engineering**, Elsevier B.V., v. 365, 2020. ISSN 00457825. DOI: 10.1016/j.cma.2020.112971.

- [30] PIETRZAK, G.; CURNIER, A. Large deformation frictional contact mechanics: continuum formulation and augmented Lagrangian treatment. **Computer Methods in Applied Mechanics and Engineering**, v. 177, n. 3-4, p. 351–381, jul. 1999. ISSN 00457825. DOI: 10.1016/S0045-7825(98)00388-0. Disponível em: <https://linkinghub.elsevier.com/retrieve/pii/S0045782598003880>.
- [31] PADMANABHAN, V.; LAURSEN, T.A. A framework for development of surface smoothing procedures in large deformation frictional contact analysis. **Finite Elements in Analysis and Design**, v. 37, n. 3, p. 173–198, mar. 2001. ISSN 0168874X. DOI: 10.1016/S0168-874X(00)00029-9. Disponível em: <https://linkinghub.elsevier.com/retrieve/pii/S0168874X00000299>.
- [32] WRIGGERS, P.; KRSTULOVIC-OPARA, L.; KORELC, J. Smooth C1-interpolations for two-dimensional frictional contact problems. **International Journal for Numerical Methods in Engineering**, v. 51, n. 12, p. 1469–1495, 2001. ISSN 00295981. DOI: 10.1002/nme.227.
- [33] LITEWKA, Przemysław. Hermite polynomial smoothing in beam-to-beam frictional contact. **Computational Mechanics**, v. 40, n. 5, p. 815–826, 2007. ISSN 01787675. DOI: 10.1007/s00466-006-0143-9.
- [34] DURVILLE, Damien. Simulation of the mechanical behaviour of woven fabrics at the scale of fibers. **International Journal of Material Forming**, v. 3, SUPPL. 2, p. 1241–1251, 2010. ISSN 19606206. DOI: 10.1007/s12289-009-0674-7.
- [35] DURVILLE, Damien. Contact-friction modeling within elastic beam assemblies: An application to knot tightening. **Computational Mechanics**, v. 49, n. 6, p. 687–707, 2012. ISSN 01787675. DOI: 10.1007/s00466-012-0683-0.
- [36] KONYUKHOV, Alexander; SCHWEIZERHOF, Karl. Geometrically exact covariant approach for contact between curves. **Computer Methods in Applied Mechanics and Engineering**, Elsevier B.V., v. 199, n. 37-40, p. 2510–2531, 2010. ISSN 00457825. DOI: 10.1016/j.cma.2010.04.012. Disponível em: <http://dx.doi.org/10.1016/j.cma.2010.04.012>.
- [37] TEMIZER, I.; WRIGGERS, P.; HUGHES, T. J.R. Three-dimensional mortar-based frictional contact treatment in isogeometric analysis with NURBS. **Computer Methods in Applied Mechanics and Engineering**, Elsevier B.V., v. 209-212, p. 115–128, 2012. ISSN 00457825. DOI: 10.1016/j.cma.2011.10.014. Disponível em: <http://dx.doi.org/10.1016/j.cma.2011.10.014>.

- [38] NISHI, S.; TERADA, K.; TEMIZER, I. Isogeometric analysis for numerical plate testing of dry woven fabrics involving frictional contact at meso-scale. **Computational Mechanics**, Springer Berlin Heidelberg, v. 64, n. 1, p. 211–229, 2019. ISSN 01787675. DOI: 10.1007/s00466-018-1666-6. Disponível em: <https://doi.org/10.1007/s00466-018-1666-6>.
- [39] MEIER, Christoph et al. Geometrically exact beam elements and smooth contact schemes for the modeling of fiber-based materials and structures. **International Journal of Solids and Structures**, Elsevier Ltd, v. 154, p. 124–146, 2018. ISSN 00207683. DOI: 10.1016/j.ijsolstr.2017.07.020. arXiv: 1611.06436. Disponível em: <https://doi.org/10.1016/j.ijsolstr.2017.07.020>.
- [40] TASORA, Alessandro et al. A geometrically exact isogeometric beam for large displacements and contacts. **Computer Methods in Applied Mechanics and Engineering**, Elsevier B.V., v. 358, p. 112635, 2020. ISSN 00457825. DOI: 10.1016/j.cma.2019.112635. Disponível em: <https://doi.org/10.1016/j.cma.2019.112635>.
- [41] KONYUKHOV, Alexander; SCHWEIZERHOF, Karl. **Computational Contact Mechanics**. Berlin, Heidelberg: Springer Berlin Heidelberg, 2013. v. 67. (Lecture Notes in Applied and Computational Mechanics). ISBN 978-3-642-31530-5. DOI: 10.1007/978-3-642-31531-2. Disponível em: <http://link.springer.com/10.1007/978-3-642-31531-2>.
- [42] LITEWKA, Przemysław. Enhanced multiple-point beam-to-beam frictionless contact finite element. **Computational Mechanics**, v. 52, n. 6, p. 1365–1380, 2013. ISSN 01787675. DOI: 10.1007/s00466-013-0881-4.
- [43] LITEWKA, Przemysław. Frictional beam-to-beam multiple-point contact finite element. **Computational Mechanics**, Springer Berlin Heidelberg, v. 56, n. 2, p. 243–264, 2015. ISSN 01787675. DOI: 10.1007/s00466-015-1169-7.
- [44] VU, T. D.; DURVILLE, D.; DAVIES, P. Finite element simulation of the mechanical behavior of synthetic braided ropes and validation on a tensile test. **International Journal of Solids and Structures**, v. 58, p. 106–116, 2015. ISSN 00207683. DOI: 10.1016/j.ijsolstr.2014.12.022.
- [45] DURVILLE, Damien et al. Determining the initial configuration and characterizing the mechanical properties of 3D angle-interlock fabrics using finite element simulation. **International Journal of Solids and Structures**, Elsevier Ltd,

- v. 154, p. 97–103, 2018. ISSN 00207683. DOI: 10.1016/j.ijsolstr.2017.06.026. Disponível em: <https://doi.org/10.1016/j.ijsolstr.2017.06.026>.
- [46] MEIER, Christoph; POPP, Alexander; WALL, Wolfgang A. A finite element approach for the line-to-line contact interaction of thin beams with arbitrary orientation. **Computer Methods in Applied Mechanics and Engineering**, Elsevier B.V., v. 308, p. 377–413, 2016. ISSN 00457825. DOI: 10.1016/j.cma.2016.05.012. arXiv: 1603.09227. Disponível em: <http://dx.doi.org/10.1016/j.cma.2016.05.012>.
- [47] MEIER, Christoph; WALL, Wolfgang A.; POPP, Alexander. A unified approach for beam-to-beam contact. **Computer Methods in Applied Mechanics and Engineering**, Elsevier B.V., v. 315, p. 972–1010, 2017. ISSN 00457825. DOI: 10.1016/j.cma.2016.11.028. arXiv: 1607.08853. Disponível em: <http://dx.doi.org/10.1016/j.cma.2016.11.028>.
- [48] BOOR, Carl de. On calculating with B-splines. **Journal of Approximation Theory**, v. 6, n. 1, p. 50–62, jul. 1972. ISSN 10960430. DOI: 10.1016/0021-9045(72)90080-9. Disponível em: <https://linkinghub.elsevier.com/retrieve/pii/0021904572900809>.
- [49] COTTRELL, J. Austin; HUGHES, Thomas J.R.; BAZILEVS, Yuri. **Isogeometric Analysis: Toward Integration of CAD and FEA**. Chichester, UK: John Wiley Sons, Ltd, ago. 2009. P. 1–335. ISBN 9780470748732. DOI: 10.1002/9780470749081. Disponível em: <http://doi.wiley.com/10.1002/9780470749081>.
- [50] PIEGL, Les; TILLER, Wayne. **The NURBS book**. Berlin, Heidelberg: Springer Berlin Heidelberg, 1997. v. 35. (Monographs in Visual Communication, 02). ISBN 9783540615453. DOI: 10.5860/choice.35-0952. Disponível em: <http://link.springer.com/10.1007/978-3-642-59223-2>.
- [51] BELYTSCHKO, Ted; NEAL, Mark O. Contact-impact by the pinball algorithm with penalty and Lagrangian methods. **International Journal for Numerical Methods in Engineering**, v. 31, n. 3, p. 547–572, mar. 1991. ISSN 10970207. DOI: 10.1002/nme.1620310309. Disponível em: <https://onlinelibrary.wiley.com/doi/10.1002/nme.1620310309>.
- [52] GAY NETO, Alfredo; WRIGGERS, Peter. Discrete element model for general polyhedra. **Computational Particle Mechanics**, v. 9, n. 2, p. 353–380, jun.

2022. ISSN 21964386. DOI: 10.1007/s40571-021-00415-z. Disponível em:  
<https://link.springer.com/10.1007/s40571-021-00415-z>.
- [53] CONN, A R; GOULD, N I M; TOINT, P L. **Trust Region Methods**. [S.l.]: Society for Industrial e Applied Mathematics (SIAM, 3600 Market Street, Floor 6, Philadelphia, PA 19104), 2000. (MPS-SIAM Series on Optimization). ISBN 9780898719857. Disponível em:  
<https://books.google.com.br/books?id=fsQOEAAAQBAJ>.
- [54] NOCEDAL, J; WRIGHT, S. **Numerical Optimization**. [S.l.]: Springer New York, 2006. (Springer Series in Operations Research and Financial Engineering). ISBN 9780387227429. Disponível em:  
<https://books.google.com.br/books?id=7wDpBwAAQBAJ>.
- [55] BOISSE, P.; GASSER, A.; HIVET, G. Analyses of fabric tensile behaviour: Determination of the biaxial tension-strain surfaces and their use in forming simulations. **Composites - Part A: Applied Science and Manufacturing**, v. 32, n. 10, p. 1395–1414, 2001. ISSN 1359835X. DOI: 10.1016/S1359-835X(01)00039-2.
- [56] WRIGGERS, Peter. **Computational contact mechanics**. Berlin, Heidelberg: Springer Berlin Heidelberg, 2006. P. 1–518. ISBN 3540326081. DOI: 10.1007/978-3-540-32609-0. Disponível em:  
<http://link.springer.com/10.1007/978-3-540-32609-0>.
- [57] HOSCHEK, Josef. Spline approximation of offset curves. **Computer Aided Geometric Design**, v. 5, n. 1, p. 33–40, jun. 1988. ISSN 01678396. DOI: 10.1016/0167-8396(88)90018-0. Disponível em:  
<https://linkinghub.elsevier.com/retrieve/pii/0167839688900180>.
- [58] PHAM, B. Offset curves and surfaces: a brief survey. **Computer-Aided Design**, v. 24, n. 4, p. 223–229, abr. 1992. ISSN 00104485. DOI: 10.1016/0010-4485(92)90059-J. Disponível em:  
<https://linkinghub.elsevier.com/retrieve/pii/001044859290059J>.
- [59] GAY NETO, Alfredo; MARTINS, Clóvis Arruda; PIMENTA, Paulo Mattos. Static analysis of offshore risers with a geometrically-exact 3D beam model subjected to unilateral contact. **Computational Mechanics**, v. 53, n. 1, p. 125–145, 2014. ISSN 01787675. DOI: 10.1007/s00466-013-0897-9.



- [60] GAY NETO, Alfredo. Dynamics of offshore risers using a geometrically-exact beam model with hydrodynamic loads and contact with the seabed. **Engineering Structures**, Elsevier Ltd, v. 125, p. 438–454, 2016. ISSN 18737323. DOI: 10.1016/j.engstruct.2016.07.005.
- [61] GAY NETO, Alfredo. **Estabilidade estrutural da configuração estática de risers em catenária**. Ago. 2012. Tese (Doutorado) – Universidade de São Paulo, São Paulo. DOI: 10.11606/T.3.2012.tde-15072013-163230. Disponível em: <http://www.teses.usp.br/teses/disponiveis/3/3152/tde-15072013-163230/>.
- [62] SIMO, J. C. A finite strain beam formulation. The three-dimensional dynamic problem. Part I. **Computer Methods in Applied Mechanics and Engineering**, v. 49, n. 1, p. 55–70, 1985. ISSN 00457825. DOI: 10.1016/0045-7825(85)90050-7.
- [63] SIMO, J. C.; VU-QUOC, L. A three-dimensional finite-strain rod model. part II: Computational aspects. **Computer Methods in Applied Mechanics and Engineering**, v. 58, n. 1, p. 79–116, 1986. ISSN 00457825. DOI: 10.1016/0045-7825(86)90079-4. Disponível em: <http://www.sciencedirect.com/science/article/pii/0045782586900794>.
- [64] SIMO, J. C.; VU-QUOC, L. A Geometrically-exact rod model incorporating shear and torsion-warping deformation. **International Journal of Solids and Structures**, v. 27, n. 3, p. 371–393, 1991. ISSN 00207683. DOI: 10.1016/0020-7683(91)90089-X.
- [65] PIMENTA, Paulo M.; YOJO, Takashi. Geometrically exact analysis of spatial frames. **Applied Mechanics Reviews**, v. 46, n. 11, s118–s128, 1993. ISSN 00036900. DOI: 10.1115/1.3122626.
- [66] PIMENTA, P. M.; CAMPELLO, E. M. B. Geometrically nonlinear analysis of thin-walled space frames. In: PROCEEDINGS of the Second European Conference on Computational Mechanics, II ECCM. [S.l.: s.n.], 2001.
- [67] DA COSTA E SILVA, Cátia et al. A simple finite element for the geometrically exact analysis of Bernoulli–Euler rods. **Computational Mechanics**, v. 65, n. 4, p. 905–923, 2020. ISSN 14320924. DOI: 10.1007/s00466-019-01800-5. Disponível em: <https://doi.org/10.1007/s00466-019-01800-5>.

- [68] FACCIO JÚNIOR, Celso Jaco et al. Modeling wind turbine blades by geometrically-exact beam and shell elements: A comparative approach. **Engineering Structures**, Elsevier, v. 180, p. 357–378, fev. 2019. ISSN 18737323. DOI: 10.1016/j.engstruct.2018.09.032.
- [69] YOJO, Takashi. **Análise Não-Linear Geometricamente Exata de Pórticos Espaciais**. 1993. Tese (Doutorado).
- [70] GAY NETO, Alfredo; PIMENTA, Paulo M.; WRIGGERS, Peter. Self-contact modeling on beams experiencing loop formation. **Computational Mechanics**, v. 55, n. 1, p. 193–208, jan. 2015. ISSN 0178-7675. DOI: 10.1007/s00466-014-1092-3. Disponível em: <http://link.springer.com/10.1007/s00466-014-1092-3>.
- [71] OTA, N. S.N. et al. Nonlinear dynamic analysis of creased shells. **Finite Elements in Analysis and Design**, Elsevier, v. 121, p. 64–74, 2016. ISSN 0168874X. DOI: 10.1016/j.finel.2016.07.008.
- [72] CRAVEIRO, Marina Vendl; GAY NETO, Alfredo. Upheaval buckling of pipelines due to internal pressure: A geometrically nonlinear finite element analysis. **Engineering Structures**, v. 158, p. 136–154, mar. 2018. ISSN 18737323. DOI: 10.1016/j.engstruct.2017.12.010. Disponível em: <https://linkinghub.elsevier.com/retrieve/pii/S0141029617319181>.
- [73] CRAVEIRO, Marina Vendl; GAY NETO, Alfredo. Lateral buckling of pipelines due to internal pressure: A geometrically nonlinear finite element analysis. **Engineering Structures**, v. 200, p. 109505, dez. 2019. ISSN 18737323. DOI: 10.1016/j.engstruct.2019.109505. Disponível em: <https://linkinghub.elsevier.com/retrieve/pii/S0141029619314373>.
- [74] GAY NETO, Alfredo; MARTINS, Clóvis de Arruda. Structural stability of flexible lines in catenary configuration under torsion. **Marine Structures**, Elsevier Ltd, v. 34, p. 16–40, 2013. ISSN 09518339. DOI: 10.1016/j.marstruc.2013.07.002.
- [75] GAY NETO, Alfredo; RIBEIRO MALTA, Eduardo; DE MATTOS PIMENTA, Paulo. Catenary riser sliding and rolling on seabed during induced lateral movement. **Marine Structures**, Elsevier Ltd, v. 41, p. 223–243, 2015. ISSN 09518339. DOI: 10.1016/j.marstruc.2015.02.001.
- [76] KORELC, Jože; WRIGGERS, Peter. **Automation of Finite Element Methods**. Cham: Springer International Publishing, 2016. ISBN

- 978-3-319-39003-1. DOI: 10.1007/978-3-319-39005-5. Disponível em:  
<http://link.springer.com/10.1007/978-3-319-39005-5>.
- [77] BROWN, L.P.; LONG, A.C. Modeling the geometry of textile reinforcements for composites: TexGen. In: **COMPOSITE Reinforcements for Optimum Performance**. [S.l.]: Elsevier, 2021. P. 237–265. DOI: 10.1016/B978-0-12-819005-0.00008-3. Disponível em:  
[http://texgen.sourceforge.net/index.php/Main\\_Page%20https://linkinghub.elsevier.com/retrieve/pii/B9780128190050000083](http://texgen.sourceforge.net/index.php/Main_Page%20https://linkinghub.elsevier.com/retrieve/pii/B9780128190050000083).
- [78] ZAVARISE, G.; WRIGGERS, P. Contact with friction between beams in 3-D space. **International Journal for Numerical Methods in Engineering**, v. 49, n. 8, p. 977–1006, nov. 2000. ISSN 00295981. DOI: 10.1002/1097-0207(20001120)49:8<977::AID-NME986>3.0.CO;2-C. Disponível em: [https://onlinelibrary.wiley.com/doi/10.1002/1097-0207\(20001120\)49:8%5C%3C977::AID-NME986%5C%3E3.0.CO;2-C](https://onlinelibrary.wiley.com/doi/10.1002/1097-0207(20001120)49:8%5C%3C977::AID-NME986%5C%3E3.0.CO;2-C).
- [79] IBRAHIMBEGOVIĆ, Adnan; MAMOURI, Saïd. On rigid components and joint constraints in nonlinear dynamics of flexible multibody systems employing 3D geometrically exact beam model. **Computer Methods in Applied Mechanics and Engineering**, v. 188, n. 4, p. 805–831, 2000. ISSN 00457825. DOI: 10.1016/S0045-7825(99)00363-1.
- [80] REFACHINHO DE CAMPOS, Paulo R.; GAY NETO, Alfredo. Rigid body formulation in a finite element context with contact interaction. **Computational Mechanics**, v. 62, n. 6, p. 1369–1398, 2018. ISSN 01787675. DOI: 10.1007/s00466-018-1569-6.
- [81] GAY NETO, Alfredo. Simulation of mechanisms modeled by geometrically-exact beams using Rodrigues rotation parameters. **Computational Mechanics**, Springer Berlin Heidelberg, v. 59, n. 3, p. 459–481, mar. 2017. ISSN 01787675. DOI: 10.1007/s00466-016-1355-2. Disponível em:  
<http://link.springer.com/10.1007/s00466-016-1355-2>.
- [82] CAO, J. et al. Characterization of mechanical behavior of woven fabrics: Experimental methods and benchmark results. **Composites Part A: Applied Science and Manufacturing**, v. 39, n. 6, p. 1037–1053, 2008. ISSN 1359835X. DOI: 10.1016/j.compositesa.2008.02.016.

- [83] REFACHINHO DE CAMPOS, Paulo R.; GAY NETO, Alfredo. Rigid body formulation in a finite element context with contact interaction. **Computational Mechanics**, v. 62, n. 6, p. 1369–1398, mar. 2018. ISSN 01787675. DOI: 10.1007/s00466-018-1569-6. Disponível em: <https://doi.org/10.1007/s00466-018-1569-6>.
- [84] FACCIO JÚNIOR, Celso Jaco; GAY NETO, Alfredo. Dynamics of wind turbine blades using a geometrically-exact beam formulation. In: June. ECCOMAS Congress 2016 - Proceedings of the 7th European Congress on Computational Methods in Applied Sciences and Engineering. Crete Island: [s.n.], 2016. v. 3, p. 4503–4519. ISBN 9786188284401. DOI: 10.7712/100016.2128.10221.